ABSTRACT

Title of dissertation: SITE-SPECIFIC INTERACTION OF DOXORUBICIN IN THE IRON RESPONSIVE ELEMENT RNA: IMPLICATIONS IN CELLULAR IRON HOMEOSTASIS AND NON-IRON DEFICIENCY ANEMIA

Luigi Jhon Alvarado, Doctor of Philosophy, 2014

Dissertation directed by: Professor T. Kwaku Dayie

Department of Chemistry & Biochemistry

A widely utilized chemotherapy drug, doxorubicin, has recently been shown to bind to a mammalian 5′ untranslated region Iron Responsive Element (IRE) RNA. In conjunction with the Iron Regulatory Protein (IRP), IRE RNA is involved in cellular iron homeostasis at the translational level. This tight RNA/protein complex prevents ribosomal assembly, hindering translation initiation of iron storage proteins, e.g. ferritin, under low cellular iron conditions. Conversely, iron overload is conducive to complex dissociation, allowing for up-regulation of the same proteins. However, this system is not entirely efficient. Some anemic patients receive adjuvant chelation therapies upon chronic blood transfusions to sequester excess labile iron. The use of doxorubicin to promote RNA/protein dissociation could potentially allow for downstream up-regulation of ferritin. In this work, I show how doxorubicin interacts with IRE RNA using multidimensional nuclear magnetic resonance, fluorescence spectroscopy, and electrophoretic mobility shift assays. All three approaches converge on the observation that the IRE/IRP complex formation is disrupted by doxorubicin. Obtaining further data on the RNA/protein/drug interactions may lead to unveiling a validated RNA target as a complementary treatment of iron overload disease, e.g. sickle cell anemia.

SITE-SPECIFIC INTERACTION OF DOXORUBICIN IN THE IRON RESPONSIVE ELEMENT RNA: IMPLICATIONS IN CELLULAR IRON HOMEOSTASIS AND NON-IRON DEFICIENCY ANEMIA

by

Luigi Jhon Alvarado

Dissertation submitted to the Faculty of the Graduate School of the
University of Maryland, College Park in partial fulfillment
of the requirements for the degree of
Doctor of Philosophy
2014

Advisory Committee:

Professor T. Kwaku Dayie, Chair
Professor David Fushman
Professor Nicole LaRonde-LeBlanc
Professor Paul Paukstelis
Professor Steven Hutcheson

Acknowledgements

The elaboration of this work would have never been possible without the unconditional support from my mentor, collaborators, colleagues, friends, and family.

I would like to thank my advisor, Professor Kwaku Dayie for his long-standing support and guidance throughout my career at the University of Maryland. Dr. Dayie was particularly understanding when I was involved in several other commitments besides laboratory research. I will be forever in debt for his patience, especially when I started in the laboratory with no prior biochemistry experience.

I am also grateful to Dr. Adegboyega Oyelere for introducing us to this magnificent project, and establishing the basis for our studies with his 2008 publication. Also, I would like to thank our collaborator, Dr. Virginia Smith, for providing us with a vital protein in our studies. My collaboration with Dr. Smith is a great example of why attending conferences is a great idea: that is how I met. Our former visiting scientist, Dr. Patrick Arthur, co-author of my first publication here, for his expertise in molecular cloning.

The Dayie Lab has been instrumental in achieving my goals, from former members to the newest. Starting with Dr. Bin Chen, who guided me through my first protein purifications. Dr. Chandar Thakur for guiding me through my first ever RNA transcription. Dr. Eldho for teaching me about lab management. Dr. Yiling Luo (2012 graduate) for useful advice and late-night company in the lab. Regan LeBlanc, my classmate, for all the help with NMR dynamics. My Le, another classmate, for her wisdom in molecular biology. Shivani Rama Reddy for her enthusiasm outside the lab.

Andrew Longhini, for numerous scientific discussions in the office, the lab, and the bar. Hyeyeon Nam, the youngest member, for her constant smiles. My undergraduate students, Kyle Eggleston and Sam Lin, for their incredible diligence and willingness to learn new techniques through the years. They were mainly responsible for RNA preparation and RNA/drug fluorescence assays. Rachel Brown for her daily company, constant support, and fun personality.

I would like to thank Dr. Daoning Zhang, NMR facilities manager, for his incredibly useful advice when using the NMR spectrometers. He trained me in my early years, and trusted me to handle the instruments on my own as time went by. Additionally, I would like to thank Dr. Lorimer and his lab for allowing me to use their fluorescence spectrometer to collect vital data for my work.

Also, I would like to thank the awards committee of the Department of Chemistry & Biochemistry. They allowed me to obtain several awards and fellowships that allowed me to travel to conferences in unimaginable places.

Special thanks to my committee members for their support, useful guidance, and critique during my career at the University of Maryland. Particular thanks to Dr. Steven Hutcheson for partaking in my thesis dissertation committee as a Dean's representative.

Finally, I would like to thank my parents Dr. Carlos Alvarado and Mrs. Doris Martinez for their everlasting love, support, and patience with me being away from home for over seven years.

To my father, my greatest scientific inspiration.

To my mother, my greatest support through the years.

To Papa Ricardo, your “enano” is still working hard to make you proud.

Table of Contents

List of Tables

List of Figures

List of Abbreviations

APRT	Adenine phosphoribosyl transferase
ATP	Adenosine 5'-triphosphate
BSA	Bovine serum albumin
CK	Creatine kinase
CSA	Chemical shift anisotropy
CSP	Chemical shift perturbation
CTP	Cytidine 5'-triphosphate
CTPS	Cytidine 5'-triphosphate synthetase
DNA	Deoxyribonucleic acid
DSS	4,4-dimethyl-4-silapentane-1-sulfonic acid
DTT	Dithiothreitol
EDTA	Ethylenediaminetetraacetic acid
FPLC	Fast performance liquid chromatography
GS	Glutamine synthase
GTP	Guanosine 5'-triphosphate
HSQC	Heteronuclear single quantum correlation
IPTG	Isopropyl β-D-1-thiogalactopyranoside
K_A	Association constant
K_D	Dissociation constant
LB	Luria-Bertani
LDH	Lactate dehydrogenase
LNA	Locked nucleic acid
MK	Myokinase
NAD^+	Nicotinamide adenine dinucleotide
NADH	Nicotinamide adenine dinucleotide, reduced
NMPK	Nucleoside monophosphate kinase
NMR	Nuclear magnetic resonance
NOESY	Nuclear Overhauser effect spectroscopy
nt	Nucleotide
NTP	Nucleoside triphosphate
PAGE	Polyacrylamide gel electrophoresis
PEG	Polyethylene glycol
PEP	Phosphoenol pyruvate
PK	Pyruvate kinase
PRPP	5'-phosphoribosyl 1'-pyrophosphate
PRPPS	5'-phosphoribosyl 1'-pyrophosphate synthetase
R5P	Ribose 5'-phosphate
REMSA	Relative electrophoretic mobility shift assay

RK	Ribokinase
RNA	Ribonucleic acid
TEABC	triethylamine bicarbonate
TROSY	Transverse relaxation optimized spectroscopy
UDP	Uridine 5'-diphosphate
UMP	Uridine 5'-monophosphate
UPRT	Uridine phosphoribosyl transferase
UTP	Uridine 5'-triphosphate
UV	Ultraviolet
Xgal	5-bromo-4-chloro-3-indolyl-β-D-galactopyranoside
XGPRT	Xanthine/guanine phosphoribosyl transferase

Chapter 1: RNA as a target for novel biomolecular therapeutics of anemia

Section 1: Prevalence of anemia

In the latest report from the World Health Organization, the Global Database on Anemia reported 24.8 % of the world's population (1.62 billion people) is affected by anemia.[1] Even more alarming, almost 50 % of preschool-age children, 42 % of pregnant women and 30 % of non-pregnant women are affected by anemia.[1] Anemia is defined as the reduction in the number of circulating red blood cells, hemoglobin or hematocrit. More commonly, the hemoglobin threshold is used as a diagnostic tool.[2] Figure 1.1 shows the worldwide prevalence of anemia in pregnant women, with African countries being the most affected, followed by Middle Eastern nations. Even in the United States, the frequency of anemia is considered mild with nearly 3.4 million affected.[3] Anemia, however, does not only affect those in good health but also 80 % of chemotherapy patients and 87 % of chronic kidney disease patients.[4,5]

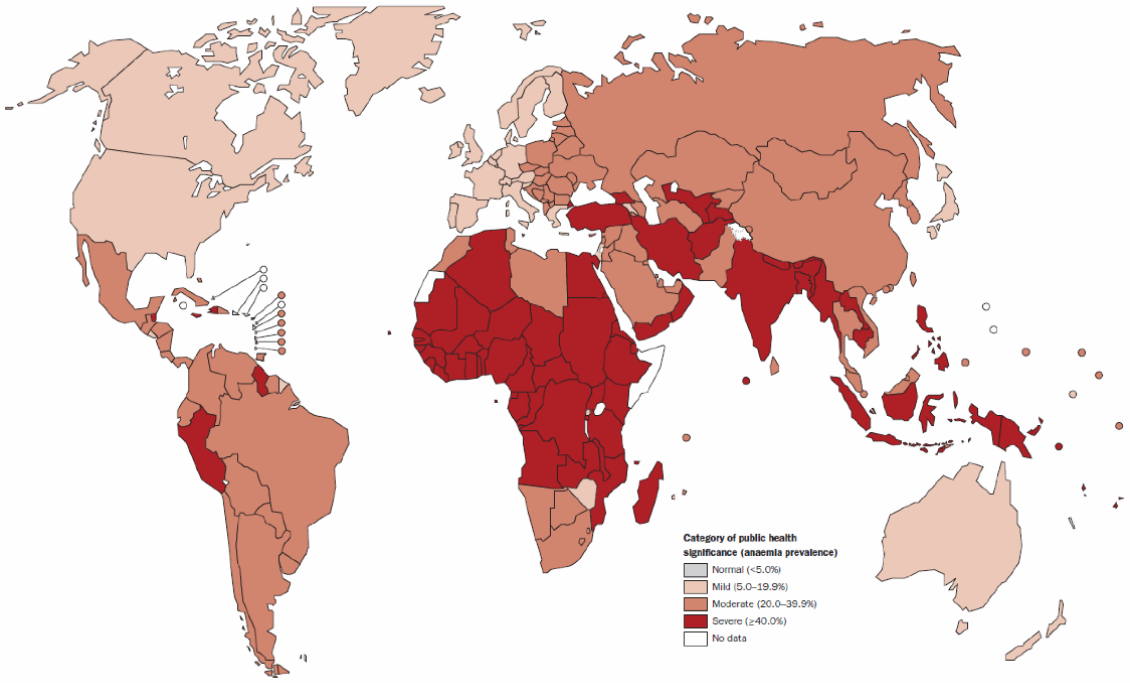

Figure 1.1. World prevalence of anemia in pregnant woman. Gray: normal (<5.0 %), pink: mild (5 – 19 %), dark pink: moderate (20 – 40 %), red: severe (>40 %), white: no data.[1]

Anemia, the disease can be broadly classified as iron- and non-iron deficiency anemia, with roughly equal distributions.[2] Iron-deficiency anemia is usually caused by inefficient absorption of dietary iron and a subsequent lack of incorporation into hemoglobin. The etiology of non-iron deficiency anemia is significantly more varied, ranging from genetic mutations to alcoholism, which leads to hemoglobin deficiency and subsequent iron accumulation.

Sickle cell and sideroblastic anemia are two well-known examples of non-iron deficiency anemia.[6–10] The treatment for both of these diseases target the recovery of normal plasma hemoglobin levels by introducing holo-hemoglobin from a donor (blood transfusion). An inevitable adjuvant component to blood transfusions is chelation therapy, whereby excess Fe(II) from the donor's hemoglobin is removed from both the

bloodstream and inside cells utilizing small molecule chelators of iron. Specifically, sickle cell disease is primarily treated by blood transfusion and often combined with deferiprone-based iron-chelation therapy. Sideroblastic anemia is treated solely by chelation therapy, which is used to circumvent formation of sideroblasts.[11] In general, treatment options seek to prevent iron over-accumulation, since this is linked to neuronal, endocrinological, obstetric and vascular disorders.[12–14]

By the same token, chelation therapy can also be detrimental for the patient. The United States Food and Drug Administration has approved two iron-chelating agents, deferoxamine and deferiprone. In 2009, 1,320 reported deaths were associated with deferiprone treatment.[15] Additionally, this drug currently holds an FDA boxed warning regarding hepatic and renal impairment.[16] This is not surprising as chelation therapy has been highly controversial for over a decade.[17–23] Among the various studies, chelation therapy was associated with nausea, joint pain, an upset stomach, low white blood cell count, zinc deficiency, and hepatic fibrosis. Brittenham et al. suggested that hepatic fibrosis might be related to deactivation of the chelating agent and thus ineffective chelation of iron.[18] Of note, Kontoghiorghes et al. suggested that in the future, treatment of non-iron deficiency anemia will not only involve chelating iron, but also preventing its cellular uptake.[19]

In accordance with Kontoghiorhes et al.'s suggestion to reduce iron intake, another option to reduce the side effects of iron chelating agents in non-iron deficiency anemia patients would be to increase safe intracellular iron storage. Therefore, our ultimate goal is to investigate the possibility of overexpressing a cellular iron-storage protein.

Section 2: Mammalian iron homeostasis

Prior to targeting a specific molecular player for our studies, an understanding of mammalian iron metabolism is required. Several reviews cover iron homeostasis at length.[24–27] However, I will briefly explain its main features. Iron homeostasis can be divided into systemic and cellular mechanisms. Systemic iron regulation is a well-studied field; however its details are beyond the scope of this study.

Cellular iron metabolism consists of the processes that take in, export, store, deliver, use, detoxify and regulate iron within a mammalian cell. For a generic mammalian cell, iron can be absorbed either as free circulating Fe^{3+} or transferrin-bound Fe^{3+} (often referred to as diferric transferrin). Free Fe^{3+} is transported by an integral membrane protein, divalent metal transporter 1 (DMT1), coupled with a ferrireductase (Dcytb), which reduces iron to Fe^{2+} for its incorporation into the intracellular iron pool.[28,29] Diferric transferrin is internalized via clathrin-mediated endocytosis, as it is recognized by another integral membrane protein, transferrin receptor 1 (tfr1).[30] Once internalized in an endosome, an ATPase actively pumps protons into its lumen, thus decreasing the pH and causing a dissociation of Fe^{3+} from transferrin.[28] As is the case for free Fe^{3+}, DMT1 coupled with another ferrireductase (Steap3) transports Fe^{2+} into the intracellular iron pool.[31,32] From this pool, Fe^{2+} can have several fates. In case iron is not needed, it can be stored in ferritin, a cytosolic protein capable of storing up to 4,500 Fe^{3+} atoms in the form of ferric oxyhydroxide phosphate ($Fe^{3+}O\text{-}PO_4$).[33,34] Otherwise, excess iron is exported from the cell by a specific membrane protein, ferroportin, coupled with a ferroxidase hephaestin, to oxidize Fe^{2+} to Fe^{3+}.[29,35] Alternately, iron can be delivered to the mitochondria via transport protein mitoferritin, where it is incorporated into heme

groups and later hemoglobin or into Fe-S clusters within an enzyme such as mitochondrial aconitase.[30]

Additionally, iron can be diverted to participate in a fascinating feedback regulatory system, the Iron Responsive Element RNA – Iron Regulatory Protein system.[28] The salient features of cellular iron metabolism are shown schematically in Figure 1.2.

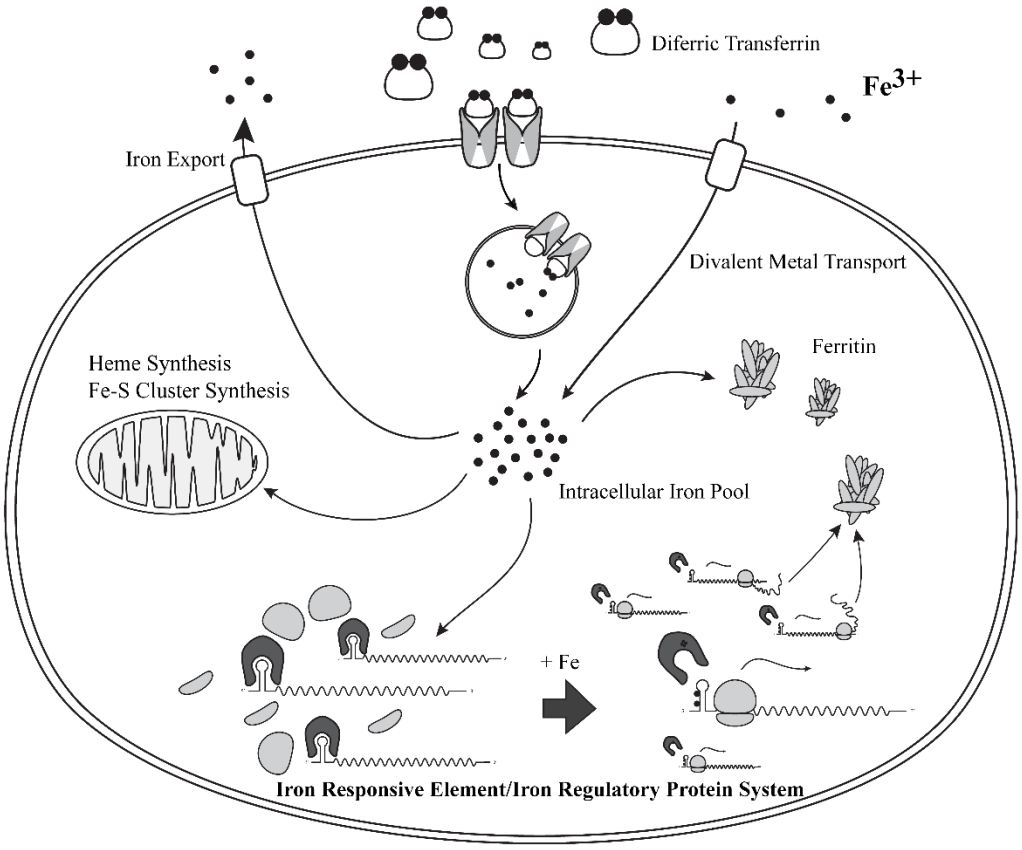

Figure 1.2. Cellular iron metabolism. Iron enters the cell as free Fe^{3+} or bound by transferrin. Free Fe^{3+} is reduced and incorporated into the intracellular iron pool. Diferric transferrin is endocytosed, and then iron is released and transported into the intracellular iron pool. From this pool, iron can be exported from the cell, stored in ferritin, transported to the mitochondria for heme or Fe-S cluster synthesis or diverted to the iron responsive element/iron regulatory protein system.

The role of iron in a feedback regulatory loop was suggested in the early 1980s. Dr. Elizabeth Theil, one of the most active scientists in the field, found that iron modulated the expression of ferritin in embryonic erythroid bullfrog cells.[36] Her initial work suggested iron increased the availability of ferritin mRNA for subsequent translation. As research progressed, it was established that this regulatory system is composed of an RNA element and a protein: an Iron Responsive Element (IRE) RNA and its trans-acting partner, the Iron Regulatory Protein (IRP).[37] The regulation scheme for the IRE-IRP system is shown in Figure 1.3. For illustration, under physiological cellular Fe^{3+} concentrations of 0.1 mM, the IRE-IRP interaction of ferritin mRNA prevents the association of the pre-initiation factors (eIF4E, eIF4G, eIF3) as well as the 40S small ribosomal subunit to the upstream region of the AUG initiation codon.[38–40] This in turn maintains a homeostatic level of ferritin-bound iron and the intracellular iron pool. When Fe^{3+} concentrations are high, there is a need to store its excess. In this scenario, the IRE-IRP interaction is disrupted, thereby allowing for formation of the pre-initiation complex recruitment, ribosomal assembly and translation of ferritin. The overexpressed ferritin is now able to retrieve excess intracellular iron.[38,40] These findings led to the conclusion that ferritin IRE RNA is a 5′ untranslated region (UTR) element, serving as a steric barrier to ribosomal pre-initiation factors and the 40S ribosome when bound to IRP. This was later tested and confirmed by a series of biochemical and biophysical characterizations of the IRE RNA.[41,42] However, ferritin is not the only protein regulated by this IRE-IRP interaction. The mRNA coding for the transferrin receptor is also under post-transcriptional control of this system.[43] In this case, the regulatory outcome for transferrin is opposite to that of ferritin. High iron content results

in low expression of the protein, consequently down-regulating the uptake of diferric-transferrin. Unlike ferritin, transferrin's mRNA contains a 3′ UTR IRE RNA element with similar characteristics to that of ferritin's 5′ UTR.[43] In summary, high iron levels are controlled by regulated sequestration and trafficking mechanisms. Conversely, low iron levels lead to decreased storage and increased intake.[38,44,45] To date, ten proteins have been shown to be under post-transcriptional control of this IRE-IRP system (Figure 1.3).[28]

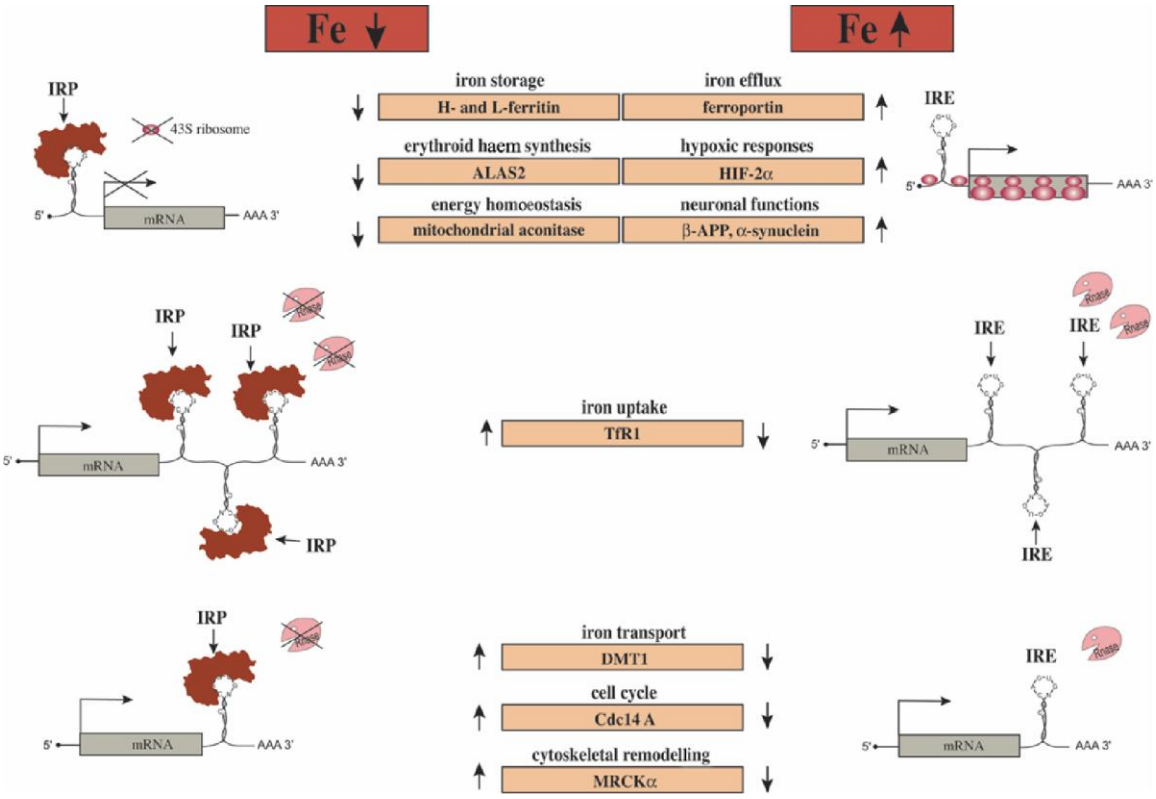

Figure 1.3. The Iron Responsive Element – Iron Regulatory Protein system for post-transcriptional control of iron metabolism and other proteins. When iron is deficient, IRE-IRP interactions are stable. Conversely, when iron is abundant or in excess, the interaction is disrupted. For mRNAs containing 5′ UTR IREs, presence of the protein binding partner restricts translation initiation. On the contrary, those with 3′ UTR IREs restrict endonuclease activity when bound to the IRP.[28]

Chapter 2: The Iron-Responsive Element RNA: a potential target for therapeutics

Section 2.1: Shifting the focus of medicinal chemistry

In our studies, I focused on the use of a small molecule drug targeted to the RNA in an RNA/protein interaction at the heart of cellular iron homeostasis. Our work is a proof of concept toward alternative treatments of non-iron deficiency anemia. Given that I focus on using a small molecule, our studies fall within the realm of medicinal chemistry of RNA: a field currently in its infancy.[46,47]

The focus of medicinal chemistry have long centered around finding small molecules that specifically target proteins, however, RNA-based drug discovery is an emerging and promising field of study. For over a decade, several authors have addressed the advantages of targeting RNA with a variety of small molecules.[48–50] Moreover, it has been suggested that fragment-based design, which has been used for protein targeting, can also be carried out for RNA.[47] To date, most RNA-binding drugs belong to the aminoglycoside family, which generally bind at the major groove with micromolar affinity.[46] One of the first and most studied RNA-small molecule interactions was the *E. coli* A-site RNA-Paromomycin complex.[51,52] The interaction was mediated by an A-A base pair and a single bulged adenine at the major groove of the RNA. This study led to the development of a number of aminoglycosides that bound either at the major or the minor groove of prokaryotic and eukaryotic RNAs. However, very few RNA-intercalating drugs have been developed or discovered. One such example is doxorubicin (Adriamycin®),[53,54] which is a potent and widely used chemotherapeutic. It is a DNA

intercalator expected to prevent topoisomerase II from eliminating DNA supercoiling during replication perhaps leading to double-stranded DNA breaks and eventual cell death.[55–58] However, off-target effects of doxorubicin have been suggested, some of which may also be involved in targeting carcinomas.[59,60]

In addition to its well-known ability to bind DNA, doxorubicin has recently been shown to bind to a 5′ untranslated region of the heavy-chain ferritin Iron Responsive Element (IRE) RNA.[61] Extensive biochemical and structural studies on this 30-nucleotide, highly-conserved hairpin RNA have led to a deeper understanding of its role in cellular iron homeostasis.[36,62–66] The RNA of interest belongs to a family of various IREs that are located either 5′ or 3′ of mRNAs encoding for proteins involved in iron intake, storage, export, and even heme synthesis.[41,67] The formation of a complex between the IRE RNA and the Iron Regulatory Protein (IRP) at the 5′ untranslated region prevents ribosomal assembly, hindering translation initiation of iron storage proteins, such as ferritin, under low cellular iron conditions.[28,68–70] Conversely, iron overload is conducive to complex dissociation, allowing for up-regulation of the proteins downstream. Upon losing its RNA-binding capability, free IRP behaves as a cytosolic aconitase, which contains a newly formed 4Fe-4S cluster responsible for its redox catalytic activity.[28,71,72] Originally, formation of this 4Fe-4S cluster was thought to be responsible for the dissociation of the IRP complex. However, it was recently shown that the direct interaction of iron(II) with the IRE RNA promotes dissociation of the complex.[64] These findings indicated that IRE RNA is also a transition metal ion binding RNA in a physiological context, similar to the Pb(II)-binding Phe-tRNA.[73,74]

Interestingly, the IRE/IRP regulatory system is not entirely efficient, nearly 50 % of ferritin mRNA is not translated even under iron overload,[67,75,76] a fact especially relevant in cases of non-iron deficiency anemia.[77] Traditional, and also outdated, therapies consist of extensive blood transfusions and adjuvant chelation therapies to sequester excess labile iron, mostly from plasma.[78–80] Alternately, it has been suggested that modern therapies of iron-overload diseases might avoid the use of chelators due to their noxious chronic effects.[81] Some of the deleterious effects observed for chelators are nausea, joint pain, low white blood cell count, zinc deficiency, hepatic fibrosis, and even death.[82]

From the available clinical and public health data, I propose that avoiding the use of iron chelators in the treatment of anemia is of utmost importance. The real question then becomes, how do I exploit our knowledge of cellular iron homeostasis toward this end? One such alternative is the exogenous manipulation of iron homeostasis via increased rate of ferritin synthesis which may lead to safer iron storage, however only few examples of such approach exist.[83] The ideal target for increasing ferritin synthesis would be the IRE RNA/IRP regulatory system.

Although most small-molecule/RNA interactions have been targeted to inhibit protein synthesis,[55,84,85] one example of downstream up-regulation was demonstrated by yohimbine. A stimulant and aphrodisiac, yohimbine, had previously been used in large excess to specifically disrupt the IRE/IRP complex *in vitro* and cause a subsequent increase in translation of the downstream message.[75] Yohimbine achieved a modest 8 % disruption of the complex *in vitro* at a thousand-fold molar ratio over the IRP concentration. Subsequent wheat germ extract translation assays showed an increase of

nearly 40 % in ferritin translation, which could not be entirely reconciled with their own results. Notably, reporter constructs such as luciferase also showed a 40 % increase in synthesis.

Similarly to yohimbine, the use of doxorubicin to promote RNA/protein dissociation could potentially enable downstream up-regulation of ferritin. I hypothesized that (i) doxorubicin intercalates specifically at two G•U wobble base pairs in the H-ferritin IRE RNA (Figure 2.1c) and that (ii) it causes partial RNA melting, with concomitant disruption of the IRE/IRP complex. In order to test these hypotheses, I used fluorescence spectroscopy, multidimensional solution nuclear magnetic resonance, and electrophoretic mobility shift assays to study how doxorubicin interacts with H-ferritin IRE RNA and how doxorubicin weakens the IRE/IRP interaction. All three approaches converge on the observation that doxorubicin disrupted the IRE/IRP complex molecular stability by roughly 45 %.

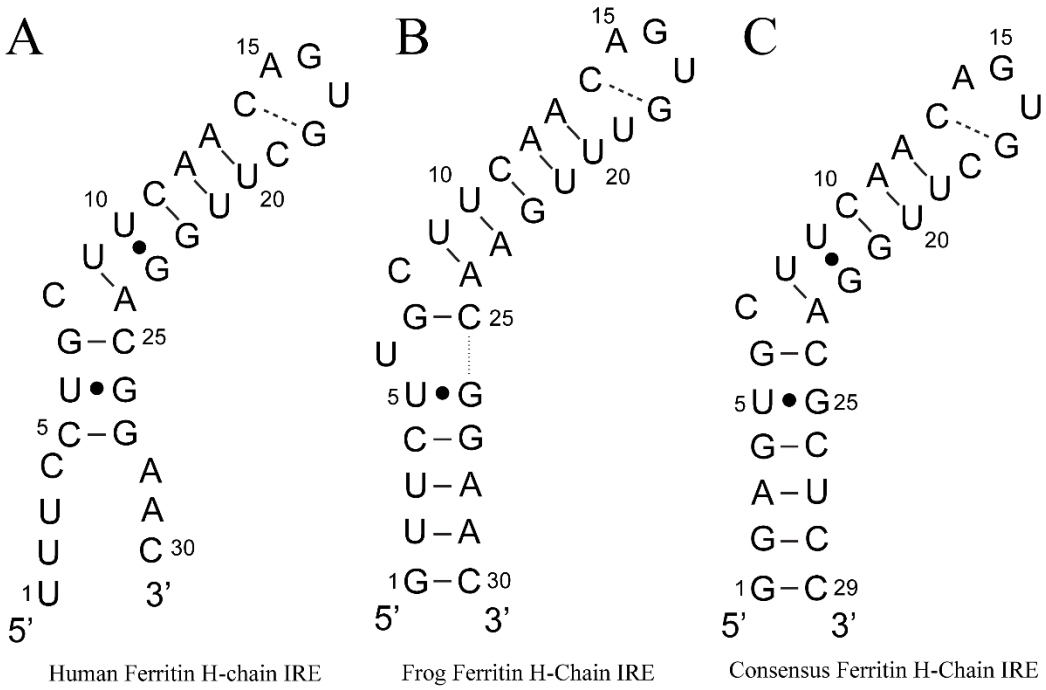

Figure 2.1. Secondary structures of ferritin heavy-chain iron responsive element RNA. (A) Human ferritin H-chain IRE.[61] (B) Frog ferritin H-chain IRE.[86] (C) A consensus-derived sequence of ferritin H-chain IRE.[87]

Section 2.2: The Iron Responsive Element RNA

Given that IRE RNAs are ubiquitous and conserved in iron homeostasis mRNAs, there is great interest in the binding specificity and affinity of the RNA to its protein partner, IRP.[88] As briefly explained above, IRE RNAs are 30-nucleotide (nt) long hairpins with a capping 6-nt loop.[89] The hexanucleotide loop has a 5′ CAG UGX 3′ conserved sequence (X is any ribonucleotide except G). Additionally, there is evidence for a closing C-G base pair, thus converting it into a pseudo-triloop.[90] The hairpin stem is split by a highly conserved C-bulge residue on the 5′ arm, kinking the stem by ~35°.[66] As revealed by NMR relaxation experiments, this C is fairly flexible in solution.[66,87] This

results in an upper and lower stem, the upper one being more conserved in sequence than the lower.[89] The upper stem contains five canonical Watson-Crick base pairs, with the possibility of a single G•U wobble base pair. The lower stem contains between 2 and 5 canonical Watson-Crick base pairs, and usually one G•U wobble pair closer to the C-bulge.[66,88–90] Figure 2.1 shows the secondary structures of three IRE RNAs from the ferritin heavy-chain mRNA of two different organisms and a consensus-derived sequence.

Initially, secondary structures were deduced from chemical protection assays, mutagenesis, cobalt hexamine binding, and radical probing.[91–93] Later, Pardi et al. determined the solution NMR structure of the free RNA, shown in Figure 2.2.[66,87] This structure confirmed the prediction of an A-form RNA helix and the flexibility of the various residues, including the C-bulge (Figure 2.2) and the 3rd, 4th and 6th nucleotides in the hexaloop. It also revealed both a *syn* conformation of the G15 in the hexaloop – suggesting its importance in IRP-recognition– and a base-stacking interaction of A14 onto C13-G17 in the hexaloop, shown in Figure 2.2. In addition, Hall et al. used a truncated IRE RNA and determined that overall it is a very flexible element, having comparable rates for global- and nucleotide-tumbling, shown in Figure 2.2b.[62] Finally, it was shown that this RNA element conforms to other RNAs of similar structures, such as the Rev response element, TAR RNA and a theophylline-binding RNA aptamer.[87]

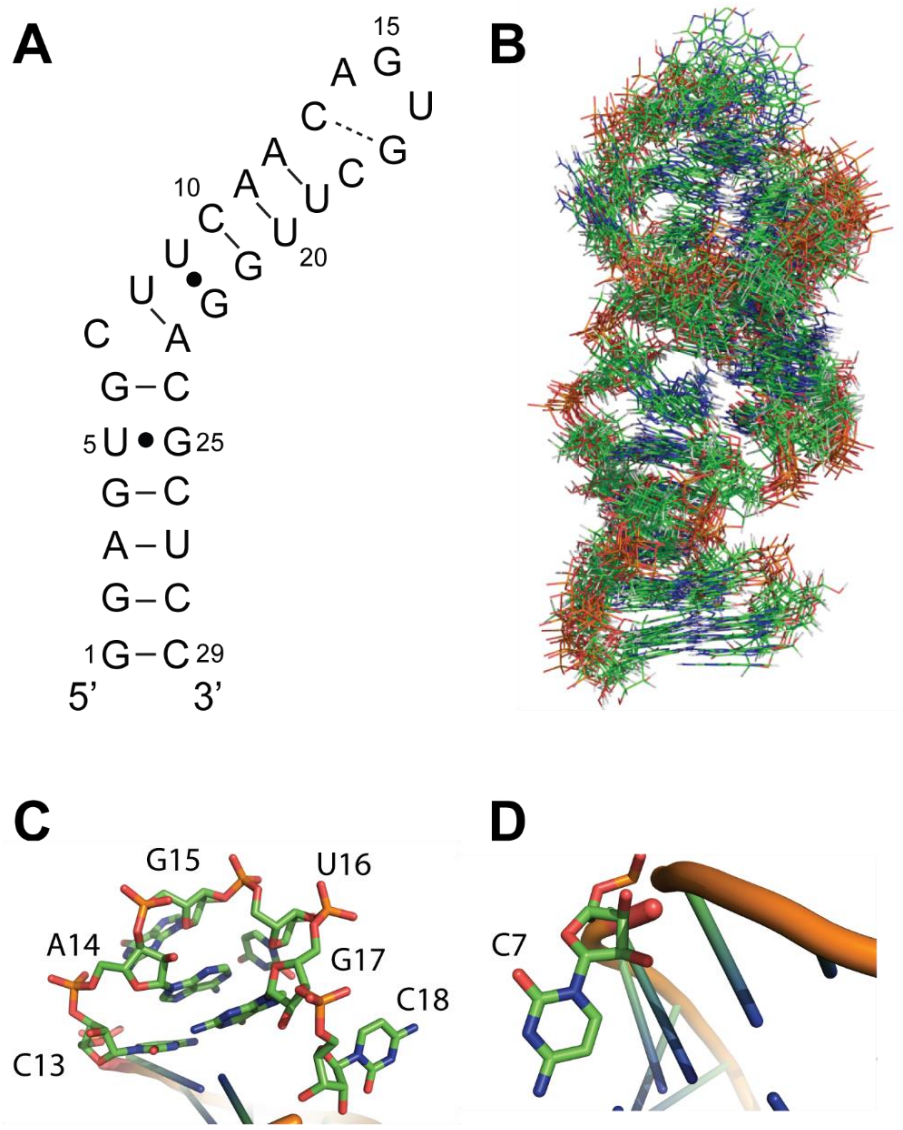

Figure 2.2. The iron responsive element RNA used in this study. (A) Heavy-chain ferritin Iron Responsive Element RNA. Solid line: canonical Watson-Crick hydrogen bonding. Dot: wobble Watson-Crick hydrogen bonding. Dashed line: canonical but variable Watson-Crick hydrogen bonding according to available solution structures.[66] (B) Overlay of fifteen NMR structures of the IRE RNA shown in (a). (C) The terminal hexaloop has a hydrogen bonding interactions between C13 and G17. (D) The stem bulge residue C7 is highly dynamic.

Section 2.3: The Iron Regulatory Protein

The human Iron Regulatory Protein (IRP) is a widely studied member of cytosolic aconitases. This 94.7 kDa monomeric protein has been characterized genetically, biochemically and structurally.[94] It consists of four clearly defined domains (I through IV), all of which make contacts with the IRE RNA. Notably, two human IRP isoforms exist.[95] Both isoforms behave similarly upon RNA-binding; they undergo a major conformational change where its domain IV is transposed by ~35 ° (Figure 2.3).[96,97] This structural rearrangement forms a complementary cavity for the IRE RNA. Interestingly, the two IRP isoforms are differentially expressed across human tissue: whereas IRP-1 is preferentially found in cardiac tissue, and IRP-2 in hepatic and kidney tissues.[98] Both bind the IRE RNA with similar estimated affinities, in the pM range.[68,87] Likewise, their mechanism of gene regulation is identical, as described above. The major difference between the two isoforms is that IRP-2 does not have the ability to form a 4Fe-4S cubane cluster. The absence of the redox-active cluster affects the degradation pathway of IRP-2 after being released from the IRE RNA under iron overload conditions. Free IRP-2 is rapidly ubiquitinated for proteosomal degradation, whereas free IRP-1 is not immediately tagged or removed.[99]

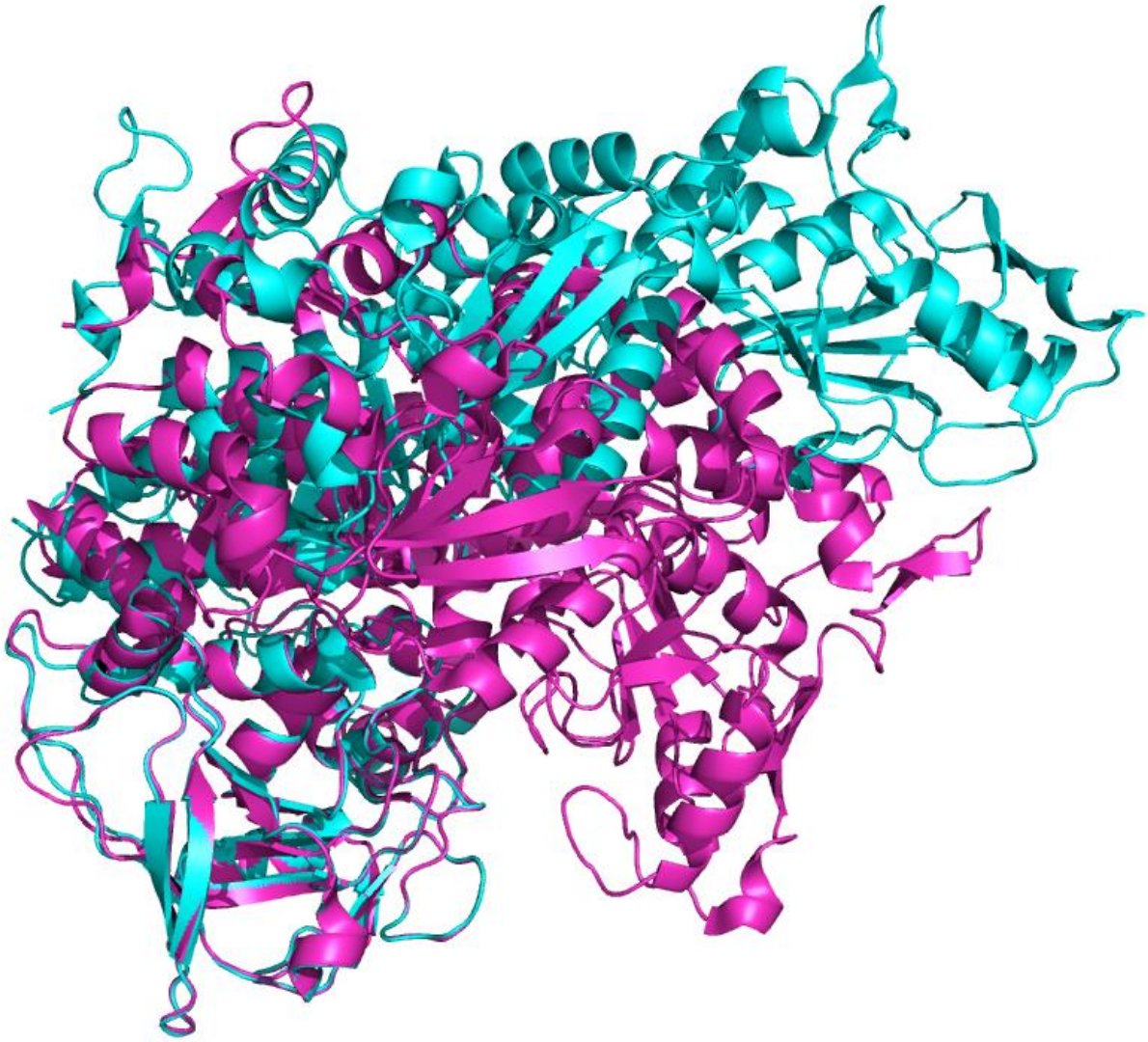

Figure 2.3. The human iron regulatory protein isoform 1. The holo-protein (magenta) shows a globular conformation, whereas the apo-protein (cyan) shows a more extended conformation in order to accommodate the IRE RNA. The holo-protein contains a 4Fe-4S cubane cluster.[86,96]

The crystal structure of the IRE RNA/hIRP-1 complex shows the extensive network of contacts that mediate this very specific interaction.[86] The RNA makes two base-specific interactions with a few amino acids in the IRP. For instance, the binding pocket of the stem bulge C consists of S681, P682, R713, R780, D781, and W782. A milieu of non-specific backbone contacts are also made between the RNA and the protein

(Figure 2.4a). Namely, phosphate backbone hydrogen bonds predominate along one face of the IRE RNA. This is especially important, as it leaves the RNA only partially engulfed by the IRP. In turn, the partial steric blockade of the RNA leaves room for any groove-binding or intercalating drugs, i.e. doxorubicin, to interact with the RNA/protein complex (Figure 2.4b). Here, I showed how this was, in fact, a partial reason for doxorubicin's ability to disrupt the IRE/IRP complex. Notably, the high-resolution data available is on a different RNA construct used herein. Walden et al. utilized the frog ferritin H-ferritin IRE RNA.[86] Its similarities with our RNA construct are the conservation of the stem-loop structure, the bulge C residue, and the hexaloop sequence. The main difference is the replacement of a G-C for a G•U wobble base pair in the upper stem of our construct.

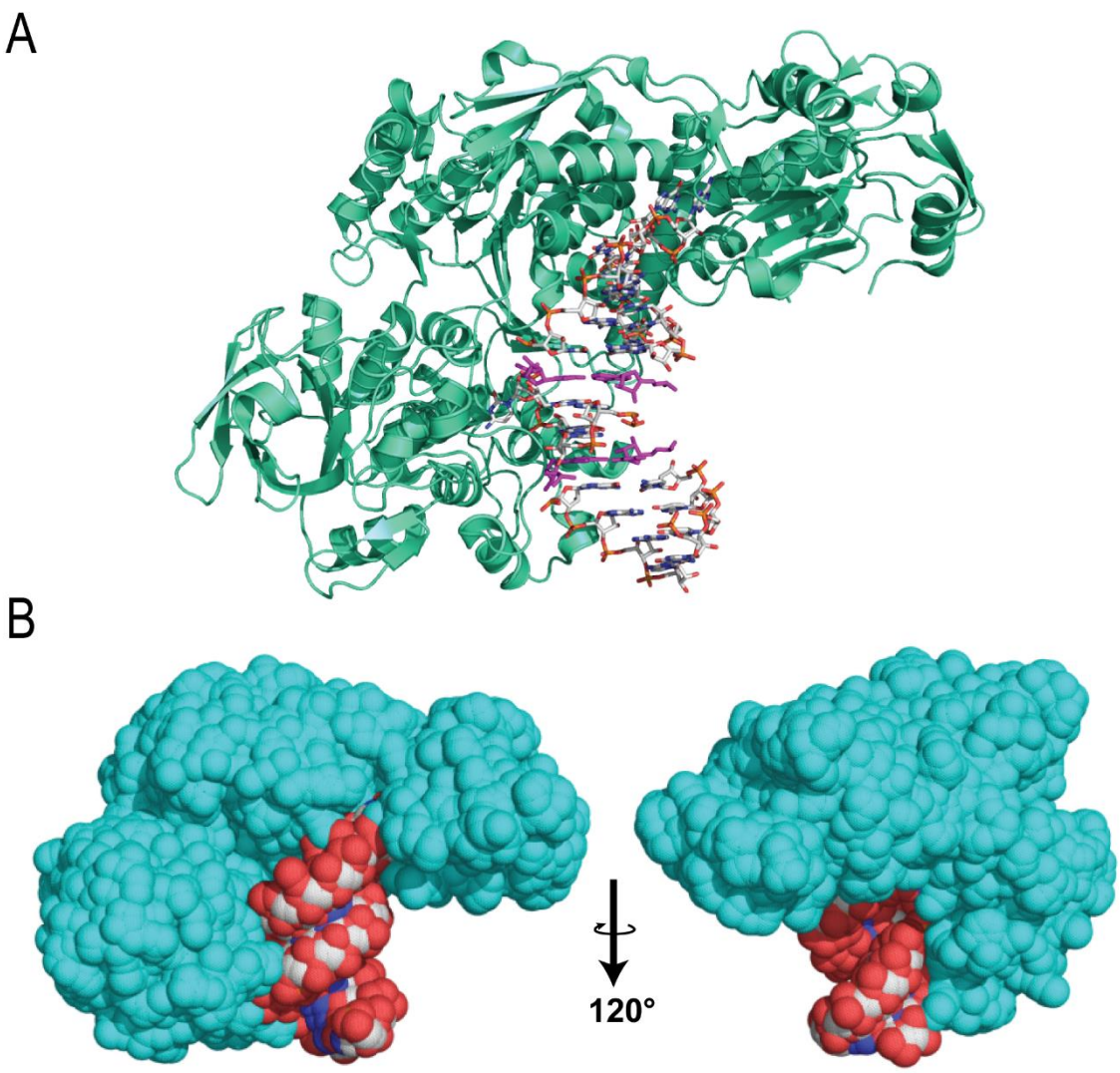

Figure 2.4. The iron responsive element RNA/iron regulatory protein complex. (A) The IRE RNA forms a high affinity complex with the IRP, mediated through a series of both specific and non-specific contacts. (B) Solvent-accessible surface representations of the IRE/IRP complex. Note the spatial engulfing of the RNA that leaves one full turn of the major groove exposed to solvent.[86]

Section 2.4: Facing the challenges

Next, this work will present the assessment of the potential of doxorubicin as an RNA-binder, and later as an RNA/protein disruptor. I utilized various methods including fluorescence spectroscopy, electrophoretic mobility shift assays and nuclear magnetic

resonance (NMR) to probe molecular interactions at both molecular- and atomic-resolution.

However, before venturing into the biochemical and biophysical characterization of our system via various methods, I explain some of the challenges associated with the NMR of RNA and the technology I developed to overcome some of these limitations using the IRE RNA as a model system. The following two chapters will address these topics at length. Then, I return to assess the RNA/doxorubicin interactions, followed by RNA/IRP interactions, and finally I evaluate the use of doxorubicin as a disruptor of this RNA/protein complex.

Chapter 3: Technology development to facilitate RNA studies by NMR: Cloning, expression, purification and assays of enzymes involved in nucleotide synthesis[100]

Section 3.1: Introduction

RNA molecules have taken center stage as fundamental transactors of catalysis and gene regulation (such as IRE RNAs) making them valuable targets for drug discovery efforts and biophysical characterizations.[101–115] Advances in methods for synthesizing labeled RNA[116–119] have fueled the development of new nuclear magnetic resonance (NMR) experiments specifically tailored for RNA characterizations.[112–114,120–122] Unfortunately, two challenges facing RNA NMR structural biology become even more acute for large RNAs: extensive spectral crowding and increased resonance linewidths.[123,124] Overcoming both challenges necessitates the development of alternate enzymatic synthetic labeling strategies using the enzymes of the E. coli pentose phosphate pathway, as depicted in Figure 3.1.[116–118] For a detailed description of challenges, see Chapter 4.1. This method enables the synthesis of all four nucleoside triphosphates (ATP, CTP, GTP, and UTP) using three phosphoribosyltransferases and CTP synthetase, and ribokinase (if using ribose), or hexokinase and three other enzymes if starting with glucose. Ribose-5-phosphate (R5P), synthesized from glucose or D-ribose, is then converted to 5-phospho-D-ribosyl-α-1-pyrophosphate (PRPP) by PRPP synthetase.

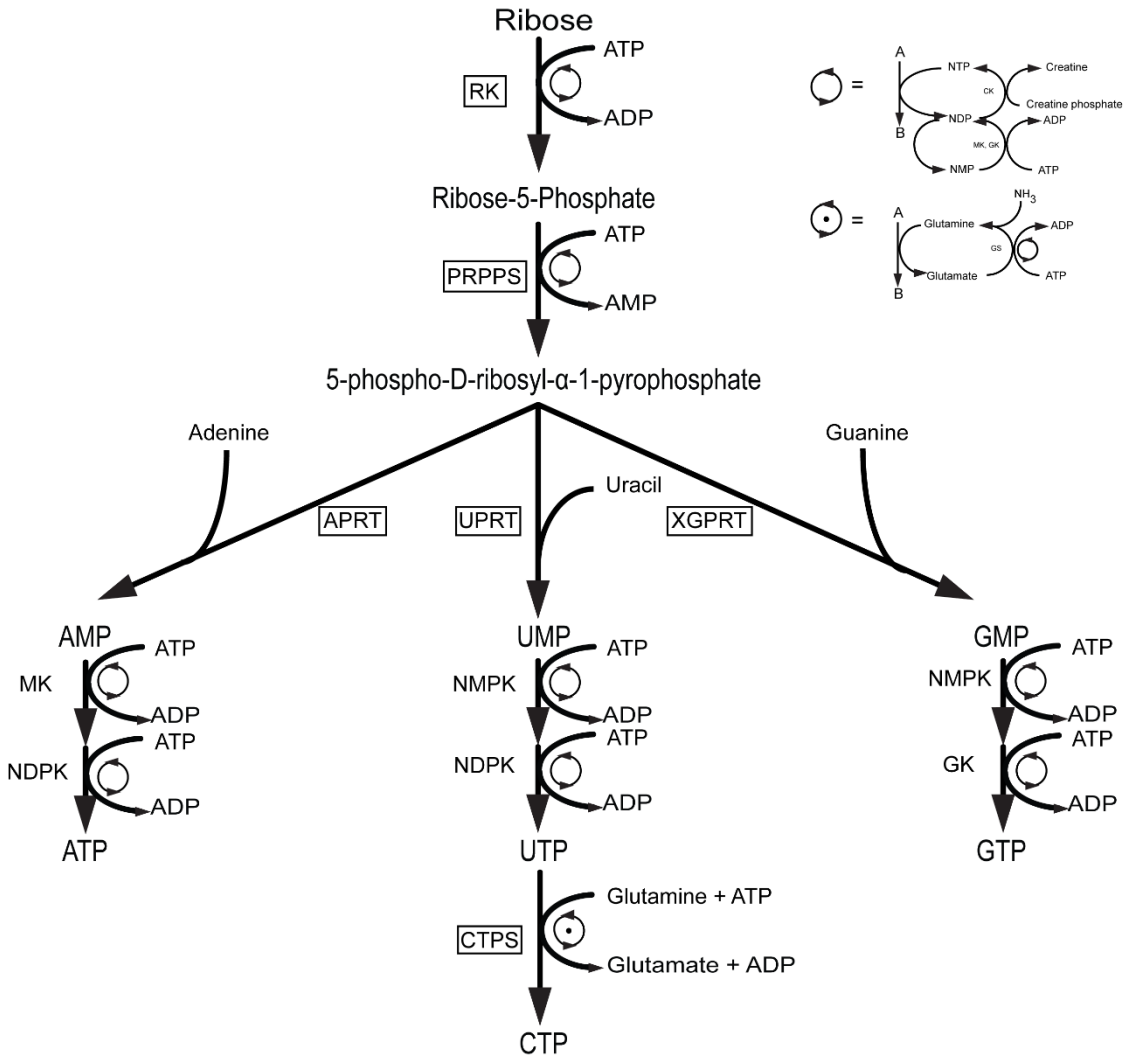

Figure 3.1. Nucleotide salvage branch of the pentose phosphate pathway. This scheme of reactions is proposed to enzymatically synthesize site-specific labeled nucleoside triphosphates (NTPs), where the boxed enzymes were expressed, purified and characterized in this work, the rest are commercially available. Starting from ribose, ribokinase (RK) would make ribose 5-phosphate. Then, phosphoribosyl pyrophosphate synthetase (PRPPS) would react on it to synthesize the activated ribose phosphate, 5-phospho-D-ribosyl-α-1-pyrophosphate. Following that, the respective adenine, uracil or xanthine/guanine phosphoribosyltransferases (APRT, UPRT, XGPRT) would synthesize AMP, UMP or GMP, respectively. The nucleoside monophosphates would then be phosphorylated by myokinase (MK), nucleoside monophosphate kinase (NMPK), nucleoside diphosphate kinase (NDPK) or guanylate kinase (GK) to the nucleoside triphosphate stage. Finally, CTP would be synthesized from UTP by CTP synthase (CTPS). Notice the ATP and glutamine regeneration schemes utilizing creatine kinase (CK) and glutamine synthase (GS), respectively.

A key advantage of this labeling scheme is the ability to differentially combine labeled glucose or ribose with labeled bases. Using this general strategy, the Williamson group has produced several isotopic labeling patterns[116,123–127] valuable for NMR spectroscopic analysis of RNA structure and dynamics. Unfortunately, one limitation of this enzymatic approach is that 6 out of the 18 enzymes required for synthesis are not commercially available and must be produced from over-expressing *E. coli* strains. This hurdle must be overcome to make this method widely adopted by the biophysics and chemical biology communities. Of these six enzymes, only ribokinase and adenosine phosphoribosyl transferase (APRT) have robust activities of 350-700 U (U is the unit of activity, defined as μmol of substrate turned over per min) per liter of bacterial culture.[128] The other five are only moderately over-expressed with activities of 28-40 U, making the enzyme preparation labor intensive.[116,125,127] By finding constructs that highly over-express the commercially unavailable enzymes, the cost and labor required to synthesize isotopically labeled NTPs could be significantly reduced. Once these constructs are produced, it is expected that the process for obtaining specifically labeled NTPs will be facile and streamlined. Ribokinase, RK (E.C. 2.7.1.15), catalyzes the phosphorylation at the ribose C5′ position to produce ribose-5-phosphate.[129] Phosphoribosyl pyrophosphate synthetase, PRPPS (E.C. 2.7.6.1), catalyzes the addition of a β,γ-diphosphate from ATP to the C1′ position of ribose 5-phosphate, activating it for the addition of a nucleobase.[130] The phosphoribosyl transferases catalyze the formation of a β-substituted ribose-5-phosphate with a specific base starting from PRPP.[131] Adenine and uracil phosphoribosyl transferases, APRT (E.C. 2.4.2.7) and UPRT (E.C. 2.4.2.9), catalyze the reaction between adenine or uracil and PRPP to form AMP or UMP, respectively.[132,133] Xanthine/Guanine

phosphoribosyltransferase, XGPRT (E.C. 2.4.2.22), catalyzes not only the transfer of guanine to PRPP to form GMP, but also the transfer of xanthine or hypoxanthine to form XMP or IMP, respectively.[134] For this study, the relevant reaction is that with guanine to form GMP. In the proposed nucleotide synthesis pathway utilizing the pentose phosphate pathway, cytosine triphosphate is not synthesized by a phosphoribosyl transferase and a kinase as is the case for ATP, GTP and UTP; there is no known cytidine phosphoribosyltransferase. Rather, CTP synthethase, CTPS (E.C. 6.3.4.2), is utilized in a separate reaction as the catalyst in the ATP-dependent production of CTP from UTP, using glutamine or ammonia as the source of nitrogen.[127,135]

In this study, I subcloned the genes encoding RK, APRT, UPRT, and XGPRT into pET15b vectors. Then I transformed these four constructs, CTPS and PRPPS into *E. coli* BL21(AI) strains for enzyme overexpression. Subsequently, I purified all six proteins by a one-step Nickel Nitrilotriacetic acid (Ni-NTA) affinity chromatography yielding enzymes with high purity and activity for use in NTP enzymatic synthesis. The production of these enzymes should make it seamless and straightforward to produce labeled nucleotides for biophysical applications.

Section 3.2: Methods

3.2.1. Cloning of RK, UPRT, APRT and XGPRT into His-tagged expression vectors

I designed the following primers (Table 3.1) to contain both XhoI and BamHI restriction sites which allowed the amplified DNA fragments to be ligated into a pET15b vector (Novagen).

Table 3.1. DNA primers used for cloning of RK, UPRT, APRT and XGPRT.

RK forward primer	dCGCCTCGAGATGCAAAACGCAGGCAGCCTCGTTGT
RK reverse primer	dGCGGGATCCTCACCTCTGCCTGTCTAAAAATGCGT
UPRT forward primer	dCCGCGCCTCGAGATGAAGATCGTGGAAGTCAAACAC
UPRT reverse primer	dGCGGGATCCTTATTTCGTACCAAAGATTTTGTCACC
APRT forward primer	dCGCCTCGAGATGACCGCGACTGCACAGCAGCTTG
APRT reverse primer	dGCGGGATCCTTAATGGCCCGGGAACGGGACAAGGC
XGPRT forward primer	dCGCCTCGAGATGAGCGAAAAATACATCGTCACCTG
XGPRT reverse primer	dGCGGGATCCTTAGCGACCGGAGATTGGCGGGACGA

The corresponding sequences of the genes were all amplified from plasmids (kindly provided by Professor Williamson at The Scripps Research Institute, La Jolla, CA) by PCR using Pfu polymerase (Stratagene). The PCR products for the different genes were gel purified using Qiagen kit and ligated into either pCR4-TOPO (Invitrogen) or pGEMT (Promega) vectors. The vectors were transformed into DH5α cells (Invitrogen), and then plated on LB/agar plates containing 100 μg/mL ampicillin and 1 μg/mL IPTG and Xgal for blue/white screening, and at least three positive white colonies were cultured in 20 mL LB media containing 100 μg/mL ampicillin. Plasmids were isolated using Qiagen Miniprep spin columns and restriction digest reactions were performed using *Xho*I and *Bam*HI (NEB). The positive plasmids were digested in a

stepwise manner with *Xho*I for 2 h at 37°C followed by DNA purification using Qiagen kit and then digested by *Bam*HI for 2 h at 37°C. Insert fragments as well as the digested pET15b were extracted from 1.5 % agarose gel using Qiagen gel extraction kit. Ligation reactions with T4 DNA ligase (NEB) were supplemented with 4 % PEG (8000 MW), and the ligated constructs were transformed into TOP10 cells (Invitrogen). The nucleotide sequences of cloned fragments were verified by sequencing. Plasmids from positive colonies, identified by digesting isolated plasmids with *Xho*I/*Bam*HI, were transformed into *E. coli* BL21(AI) for protein over-expression (Figure 3.2).

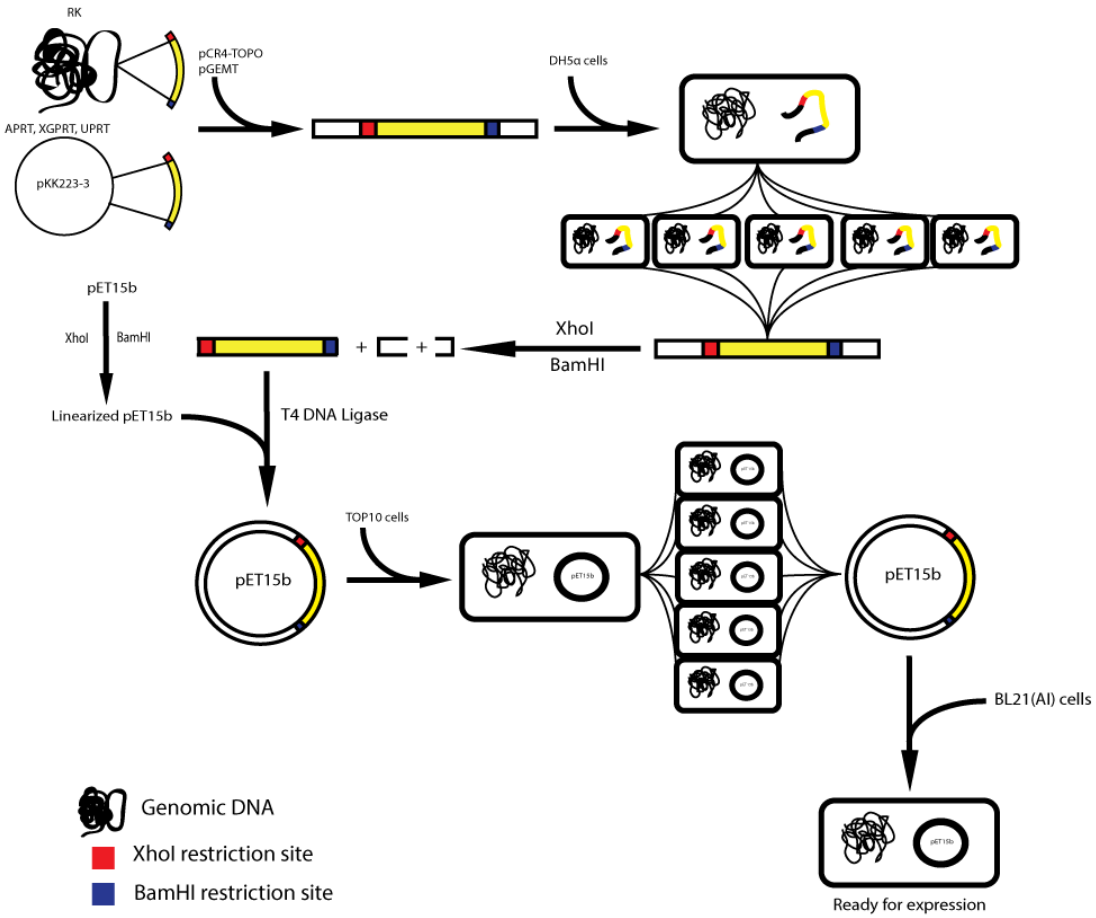

Figure 3.2. Cloning and sub-cloning of enzymes from the pentose phosphate pathway into high-copy plasmids for bacterial overexpression. The gene encoding for RK was extracted from *E. coli* genomic DNA by classical techniques. The genes for APRT, XGPRT and UPRT were all sub-cloned from an existing low-copy plasmid. All genes were then inserted into a linearized plasmid, propagated and digested by XhoI and BamHI restriction enzymes. The products were ligated into a pET15b high-copy plasmid under T7 RNA polymerase transcription, propagated and finally transformed into *E. coli* strain BL21(AI).

3.2.2. Protein expression of RK, UPRT, APRT and XGPRT

All four enzymes not obtained commercially were overexpressed and purified using similar procedures. The pET15b plasmid constructs prepared in this work, were all transformed into *E.coli* strain BL21(AI) (Invitrogen) for protein overexpression under arabinose regulation and IPTG induction. All protein expressions and purifications were

carried out for RK as described previously with very little modification.[129,136] Cells transformed with the RK construct were grown onto LB plates supplemented with 100 μg/mL ampicillin. A single colony was grown at 37˚C in a 5-mL starter culture of LB media with 100 μg/mL ampicillin to OD_{600}=0.60 (ca. 4h). The cells were harvested by centrifugation at 3800 rpm for 15 min, resuspended in fresh LB, and added to 100 mL LB media with 100 μg/mL ampicillin. The cell culture was grown at 37°C to OD_{600}=0.60 (ca. 2h); then the cells were harvested by centrifugation at 3800 rpm for 15 min and resuspended in fresh LB and added to 1 L LB media with 100 μg/mL ampicillin. Expression was induced with 0.05 % L-(+)-arabinose at 37°C for 2 h followed by addition of 1mM IPTG for 3 h at 37°C. The cells were harvested by centrifugation at 4500 rpm for 25 min at 4°C, and stored at - 80°C.

3.2.3. Protein expression of PRPP synthetase

The plasmid used for expression of full length human PRPP synthetase was cloned into the *Nde*I and *Xho*I restriction sites of pET22b(+) expression plasmid (a generous gift from Professor Sheng Li, Graduate school of the Chinese Academy of Sciences, Shanghai) was transformed into the *E.coli* BL21(AI) cells (Invitrogen) to produce an overexpressing strain of isoform 1 of human PRPPS. PRPPS expression and purification were carried out as described previously with some modifications [31]. A single colony was grown at 37˚C in a 5-mL starter culture of LB media with 100 μg/mL ampicillin to OD_{600}=0.60 (ca. 4h). The cells were harvested by centrifugation at 3800 rpm for 15 min, resuspended in fresh LB, and added to 100 mL LB media with 100 μg/mL ampicillin. The cell culture was grown at 37°C to OD_{600}=0.60 (ca. 2h); then the cells were harvested by centrifugation at 3800 rpm for 15 min and resuspended in fresh LB

and added to 1 L LB media with 100 μg/mL ampicillin. Expression was induced with 0.05 % L-(+)-arabinose at 37°C for 2 h followed by addition of 1mM IPTG for 3 h at 37°C. The cells were harvested by centrifugation at 4500 rpm for 25 min at 4°C, and stored at -80°C.

3.2.4. Protein expression of CTP synthetase

The CTP synthetase gene sub-cloned into pET15b (a kind gift of Professor Stephen L. Bearne, Department of Biochemistry and Molecular Biology, Dalhousie University, Halifax, Nova Scotia) was transformed into *E.coli* BL21(AI) strain and overexpressed. A single colony was grown at 37˚C in a 5-mL starter culture of LB media with 100 μg/mL ampicillin to OD_{600}=0.60 (ca. 4h). The cells were harvested by centrifugation at 3800 rpm for 15 min, resuspended in fresh LB, and added to 100 mL LB media with 100 μg/mL ampicillin. The cell culture was grown at 37°C to OD_{600}=0.60 (ca. 2h); then cells were harvested by centrifugation at 3800 rpm for 15 min and resuspended in fresh LB and added to 1 L LB media with 100 μg/mL ampicillin. Expression was induced with 0.05 % L-(+)-arabinose at 37°C for 2 h followed by addition of 1mM IPTG for 3 h at 37°C. The cells were harvested by centrifugation at 4500 rpm for 25 min at 4°C, and stored at -80°C.

3.2.5. Protein purification

Conditions for the purification of all the recombinant his-tagged enzymes were optimized for maximal yield and purity by nickel affinity chromatography, and, as an optional step, size exclusion chromatography could be performed using Sephadex S75 gel filtration column for all the proteins. The frozen cell pellet was resuspended in lysis buffer (50 mM NaH_2PO_4, 300 mM NaCl, 10 mM imidazole, pH 8) supplemented with 1

mg/mL lysozyme and placed on ice for 30 min without addition of nucleases. The cells were disrupted by sonication at 4°C for 1 min with 1 min resting periods. The cellular debris was pelleted by centrifugation at 46000 g and 4°C for 30 min and the viscous nucleic acids were manually removed using a pipette. The purifications were carried out following the QIAexpressionist handbook (Qiagen) with very little modification. The supernatant was applied to pre-packed Ni-NTA beads in column mode, previously equilibrated with lysis buffer.

Following incubation, the Ni-NTA column was washed with 6 bed volumes of wash buffer (50 mM NaH_2PO_4, 300 mM NaCl, 50 mM imidazole, pH 8). Recombinant proteins were then eluted from the Ni-NTA column with elution buffer (wash buffer with 400 mM imidazole). The volume of the two eluates were reduced using Amicon ultra tubes (Milipore), typically to 200 µL and then buffer-exchanged to its final storage buffer (50 mM NaH_2PO_4, 150 mM NaCl or 300 mM NaCl for PRPPS only) to a final volume of 1 mL. Equal volume of 100 % glycerol was added and the proteins were stored at -20°C. The different stages of purification were monitored by SDSPAGE. Protein concentrations were determined by Bradford assay employing BSA as the standard.

3.2.6. Enzyme activity assay for RK

The spectrophotometric assay is based on the coupled enzyme system[116,137] as seen in Figure 3a. The assay mixture (1 mL) contained 50 mM Tris-HCl buffer at pH 7.8, 5 mM Ribose, 3 mM ATP, 1 mM PEP, 100 mM KCl, 10 mM $MgCl_2$, 0.2 mM NADH, 2 U of lactate dehydrogenase, and 2 U of pyruvate kinase. The mixture was incubated for 5 min until a steady baseline was obtained and then a 2-µL aliquot of ribokinase was added

to initiate the reaction. The absorbance change at 340 nm (ΔA_{340}) was monitored as a function of time using the linear range of the kinetic trace. Units of activity were calculated as a function of the total reaction volume (V in L), path length (l in cm), time (t in min), change in extinction coefficient of 6220 M^{-1} cm^{-1} at 340 nm for oxidation of NADH to NAD^+ and K = 1:

$$U = \frac{V * \Delta A}{K * \varepsilon * t * l}$$

3.2.7. Enzyme activity assay for PRPP synthetase

The spectrophotometric assay is based on the coupled enzyme system [39] as shown in Figure 3b. The assay mixture (1 mL) contained 50 mM Tris-HCl buffer at pH 7.5, 5 mM R5P , 3 mM ATP , 1mM PEP , 10 mM $MgCl_2$, 0.2mM NADH, 2 U of lactate dehydrogenase, 2 U of pyruvate kinase, and 2 U of adenylate kinase. The mixture was incubated for 5 min until a steady baseline was obtained and then a 2-µL aliquot of PRPP synthetase was added to initiate the reaction. The absorbance change at 340 nm (ΔA_{340}) was monitored as a function of time using the linear range of the kinetic trace. Units of activity were calculated using equation (1), where ε = 6220 M^{-1} cm^{-1} at 340 nm and K = 2.

3.2.8. Enzyme activity assay for APRT

The spectrophotometric assay is based on the coupled enzyme system[116,137] [17,39] as shown in Figure 3c. The assay mixture (1 mL) contained 50 mM Tris-HCl buffer at pH 7.8, 1.5 mM PRPP, 3 mM ATP, 1 mM PEP, 1.5 mM adenine hydrochloride, 10 mM $MgCl_2$, 0.2 mM NADH, 2 U of lactate dehydrogenase, 2 U of pyruvate kinase

and 2 U of adenylate kinase. The mixture was incubated for 5 min until a steady baseline was obtained and then a 2-μL aliquot of APRT was added to initiate the reaction. The absorbance change at 340 nm (ΔA_{340}) was monitored as a function of time using the linear range of the kinetic trace. Units of activity were calculated using equation (1), where $\varepsilon = 6220\ M^{-1}\ cm^{-1}$ at 340 nm and K = 2.

3.2.9. Enzyme activity assay for XGPRT

The spectrophotometric assay is based on monitoring the conversion of guanine (246 nm) to GMP at 257.5 nm using the change in extinction coefficient of ε=5817 $M^{-1}\ cm^{-1}$ as shown in Figure 3d.[138–140] The assay mixture (1 mL) contained 100 mM Tris-HCl buffer at pH 7.5, 1 mM PRPP, 50 μM of guanine, 100 mM $MgCl_2$ and a 2-μL aliquot of XGPRT. The reaction mixture was incubated without guanine for 5 min. Then, the reaction was initiated by the addition of guanine, and the formation of GMP was monitored at 257.5 nm at 25 ˚C until it reached saturation after 5-7 min.[139] Units of activity were calculated using equation (1), where $\varepsilon = 5817\ M^{-1}\ cm^{-1}$ at 257.5 nm and K = 1.

3.2.10. Enzyme activity assay for UPRT

The spectrophotometric assay is based on monitoring the conversion of uracil (271 nm) to UMP using the change in extinction coefficient of ε=2763 $M^{-1}\ cm^{-1}$ as shown in Figure 3e.[116] The assay mixture (1 mL) contained 50 mM Tris-HCl (pH 7.5), 1.5 mM PRPP, 0.1 mM of uracil, 5 mM $MgCl_2$ and a 2-μL aliquot of UPRT. The reaction was incubated without uracil for 5 min. Then the reaction was initiated by addition of uracil, and the formation of UMP was monitored at 271 nm at 25 or 37˚C until it reached

saturation after 5-7 min. Units of activity were calculated using equation (1), where ε = 2763 M^{-1} cm^{-1} at 271 nm and K = 1.

3.2.11. Enzyme activity assay for CTP synthase

The spectrophotometric assay is based on the increase in absorbance at 291nm following conversion of UTP to CTP using the change in extinction coefficient of ε=1338 M^{-1} cm^{-1} as shown in Figure 3f.[116,141] The assay mixture (1 mL) contained 50 mM Tris-HCl (pH 8.0), 10 mM $MgCl_2$, 1 mM UTP, 1 mM ATP, 0.25 mM GTP, 10 mM glutamine and a 2-µL aliquot of CTPS. The reaction was incubated without glutamine for 5 min. Then the reaction was initiated by addition of glutamine, and the formation of CTP was monitored at 291 nm at 25 or 37˚C until it reached saturation after 12-15 min. Units of activity were calculated using equation (1), where ε = 1338 M^{-1} cm^{-1} at 291 nm and K = 1.

As an independent method for cross-validating the spectrophotometric method, ^{1}H-^{13}C heteronuclear single quantum correlation (HSQC) NMR experiment was performed on a 600 MHz Bruker Avance III spectrometer at 37°C. The NMR assay is based on the appearance of ^{13}C –labeled CTP and disappearance of ^{13}C –labeled UTP as monitored through the C5 aromatic carbons of UTP and CTP. The UTP C5 carbon resonates in a spectral region (~103 ppm) distinct from CTP's C5 (~97 ppm) carbon. This separation makes it very straightforward to monitor the formation of CTP from UTP using two-dimensional NMR. Unfortunately, 1D NMR fails because the H5 proton resonances of both UTP and CTP overlap with their ribose H1′ proton resonances. The carbon resonances remove this degeneracy. Under our reaction conditions, CTP is made quantitatively in 30 min from UTP. The assay mixture (250µL) contained 90 % D_2O, 50

mM Tris-HCl (pH 8.0), 10 mM $MgCl_2$, 1 mM ^{13}C-^{15}N-UTP (Sigma-Aldrich), 1 mM ATP, 0.25 mM GTP, 10 mM glutamine and a 0.5-µL aliquot of CTPS. The reaction was incubated without glutamine for 5 min. The reaction was initiated by the addition of glutamine. The formation of CTP and disappearance of UTP were monitored at 37 °C until the reaction reached saturation after 30 min. The results were fit the following equation:

$$Y = Y_o + (Y_{sat} - Y_o) * (1 - e^{(-R*t)})$$

were Y_o is the y-intercept, Y_{sat} is the y-value at saturation, R is the first-order rate constant and t is the time elapsed. Data processing and analysis were performed with TopSpin 2.0 and GraphPad Prism 5 softwares.

Section 3.3: Results

Labeled nucleotides are valuable for use in *in vitro* transcription of labeled RNA for structural and dynamics studies, yet a number of enzymes of the pentose phosphate pathway needed to make these nucleotides cost-effectively are currently not commercially available. I have therefore focused on elaborating optimal conditions of facile protein production to help in making these nucleotides for NMR studies of RNA.

3.3.1. Cloning and subcloning of genes encoding for RK, APRT, UPRT and XGPRT

The RK gene was subcloned from the genomic DNA into pGEMT vectors and transformed into DH5α *E. coli* cell line for selection of positive colonies, and subcloned into the pET15b vector, encoding an N-terminal His_6 tag. The new construct was

transformed into *E. coli* BL21(AI) cell line for protein overexpression. Sequencing, preparative scale protein expression and diagnostic SDS-PAGE confirmed the successful cloning and expression of the RK construct.

Similarly, the genes for APRT, UPRT and XGPRT, all initially in a pKK223-3 vector, were subcloned into a pCR4-TOPO plasmid and the subsequent selection, propagation, isolations and subcloning were identical to those performed for the RK gene. The new constructs were again inserted into a pET15b vector and the resulting genes were expressed efficiently in BL21(AI) *E. coli*. Sequencing, preparative scale protein expression and diagnostic SDS-PAGE confirmed the successful cloning and expression of the gene constructs. Similarly, for the clones of PRPPS and CTPS, the respective vectors were transformed into *E. coli* BL21(AI) strain for protein overexpression.

3.3.2. Expression and purification of proteins

Subcloning and transforming all the genes into identical expression hosts facilitated the expression and purification of these six enzymes, using a simplified and generalized protocol by a one-step NiNTA affinity chromatography. With this protocol, the overexpression and purification of all six enzymes was performed in two days.

The overexpression of the proteins produced reproducibly milligram amounts of protein. Test expressions were performed with a combination of different concentrations of L-(+)-arabinose, lactose and IPTG to optimize conditions for overexpression. Induction of one-liter cultures for 2 h under 0.05 % L-(+)-arabinose and immediately after for 3 h under 1 mM IPTG produced the greatest amount of protein per liter culture,

with an average of 8 g of wet cell pellet for all constructs. Nevertheless, the amount of final purified protein ranged from 1 to 24 mg per liter culture and each protein construct gave reproducible quantities.

For the His-tag purification, it was found that purification was most efficient for all six proteins using 50 and 400 mM imidazole in the wash and elution buffers, respectively, as judged by SDS-PAGE (Fig. 3.3). The percent recovery of protein from the crude supernatant of the whole cell lysate ranged from 0.5 to 5 % considering that total protein in the crude lysate ranged from 200 to 580 mg. The strain overexpressing PRPPS yielded the lowest amount of protein, whereas the strain overexpressing APRT gave the highest (Table 3.2). The SDS-PAGE analysis indicated that all six proteins have a purity of >90 % (Figure 3.3). This was also observed in the activity assays, as activities remained unaffected or were even higher than previously reported.

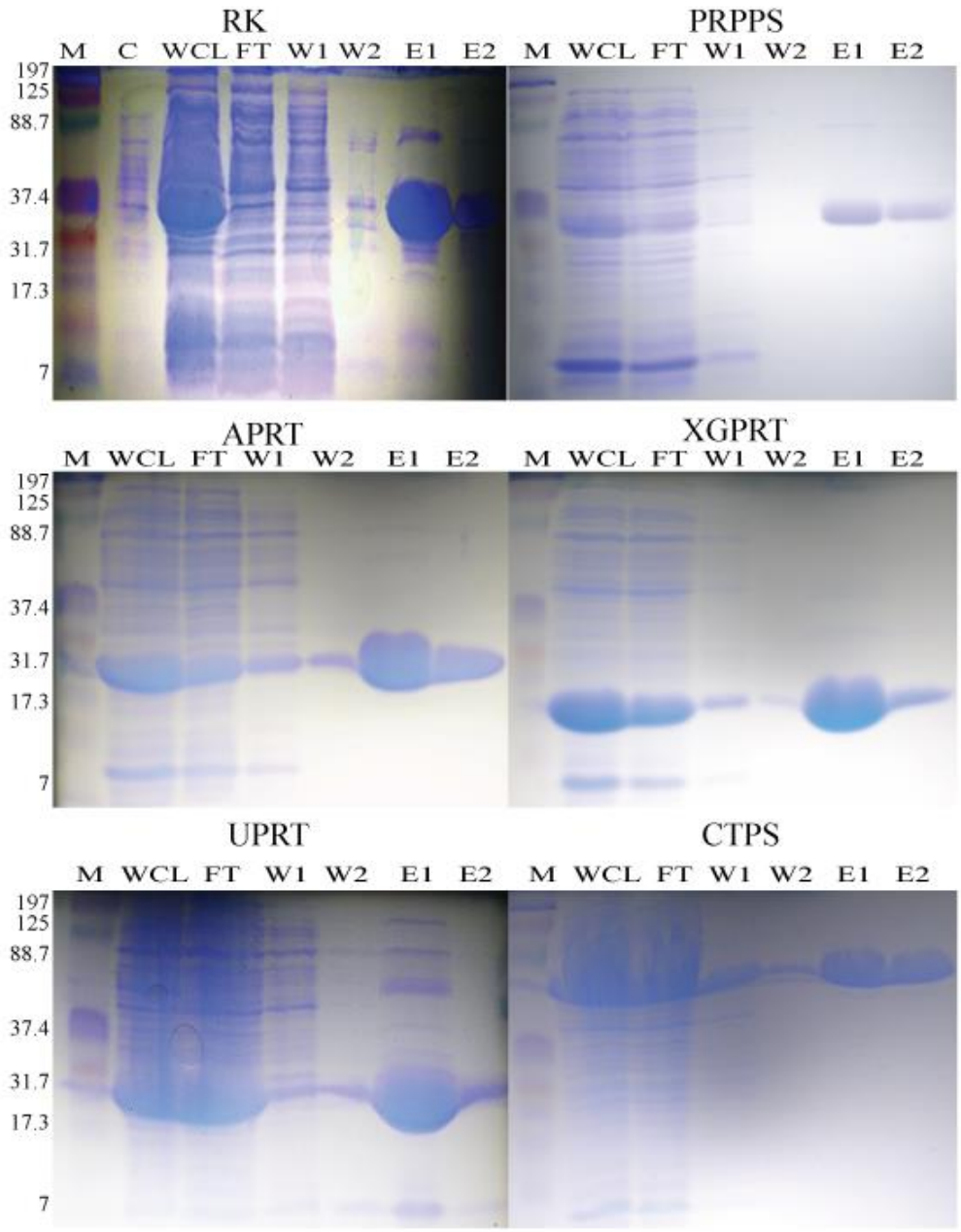

Figure 3.3. Representative SDS-PAGEs from each of the six pentose phosphate pathway enzyme purifications. (M) Marker (kDa) (C) Uninduced control (WCL) Supernatant of the whole cell lysate (FT) Nickel column flow-through (W1, W2) Column wash 1 and 2 (E1, E2) Fractions of imidazole eluted protein 1 and 2. The apparent molecular weights are 37, 34, 19, 15, 19 and 67 kDa for RK, PRPPS, APRT, XGPRT, UPRT and CTPS, respectively.

3.3.3. Enzymatic activity of purified His-tagged proteins

Direct and indirect continuous spectrophotometric assays were performed to check the activity of all six enzymes at the two stages of purification. XGPRT, UPRT and CTPS were assayed directly by monitoring the appearance of the nucleotide product at their respective wavelength. RK, PRPPS and APRT were assayed indirectly by coupling their activities with NADH oxidation (Figures 3.4 and 3.5). Initial rates and maximal activity were obtained from every reaction, and the purified RK, UPRT, XGPRT and CTPS yielded robust total activities of 1500 to 2300 U per liter of bacterial culture, whereas PRPPS yielded 22 U per liter and APRT 484 U per liter. In addition, the following specific activities for each enzyme were obtained: 70 U/mg for RK (Compare to 75 U/mg),[142] 22 U/mg for PRPPS (Compare to 25 U/mg),[143] and 21 U/mg for APRT (Compare to 14 U/mg).[144] Moreover, the specific activities for XGPRT, UPRT and CTPS were higher than previously reported, 128, 144 and 113 U/mg, respectively. These numbers should be compared to 95 U/mg;[145] 7 U/mg;[133] and 8 U/mg, respectively for the same proteins.[146] Purification folds calculated for these enzymes ranged from 1- to ~ 20-fold: APRT had a similar specific activity and negligible purification fold and XGPRT attained almost a 20-fold purification. Given that the specific activity of CTPS was unusually high with respect to recent work,[146] a ^{13}C NMR assay was conducted as an independent validation method (Fig. 3.6). The NMR method afforded a direct means of simultaneously monitoring the depletion of UTP and the accumulation of CTP using the distinct chemical shifts of uracil's C5 atom (at 103 ppm) and cytosine's C5 atom (at 97 ppm). The resulting total activity of CTPS was 2640 U per liter, which yielded a specific activity of 131U/mg, an activity comparable to that found using the spectrophotometric

assay at 37°C. This experiment conducted in 90 % H_2O gave a similar specific activity of 169 U/mg. The values obtained in this work are consistently higher than previously reported.

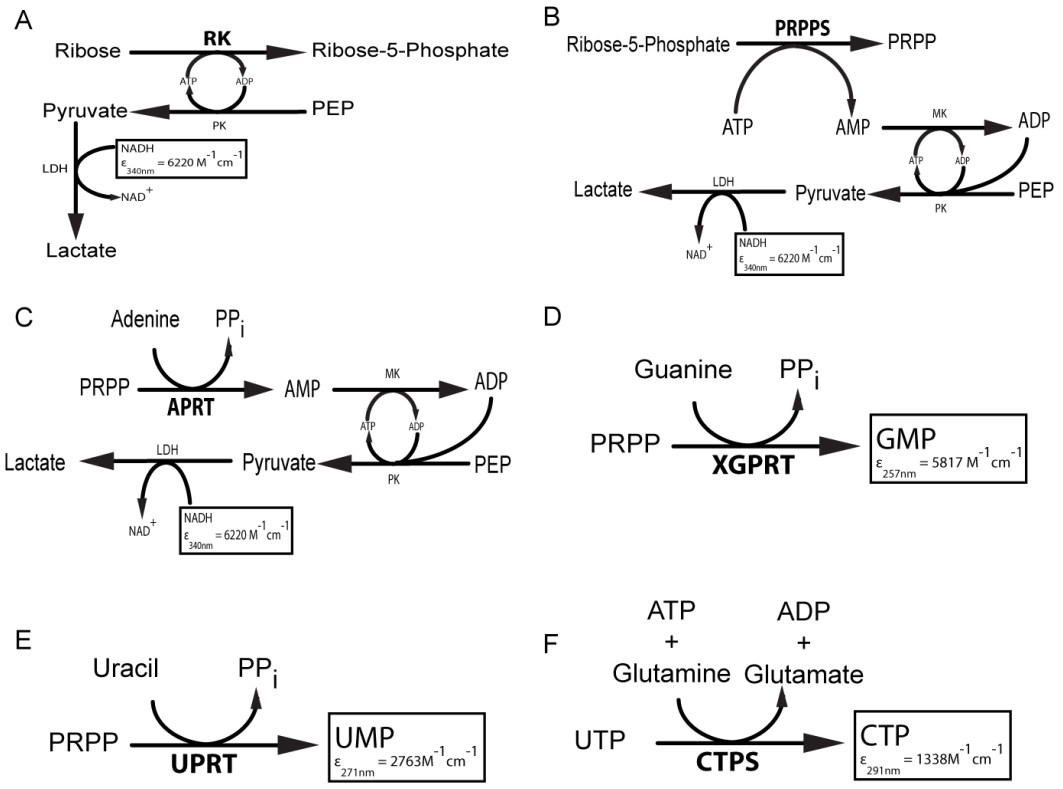

Figure 3.4. Direct and indirect continuous activity assays used for the six enzymes of the pentose phosphate pathway. (a) RK (b) PRPPS (c) APRT (d) XGPRT (e) UPRT (f) CTPS. The boxed molecule corresponds to the one being monitored during the assay at the specific wavelength with the corresponding molar extinction coefficient in $M^{-1}cm^{-1}$. MK: myokinase, PK: pyruvate kinase, LDH: lactate dehydrogenase, PEP: phopshoenol pyruvate, PP_i= inorganic pyrophosphate.

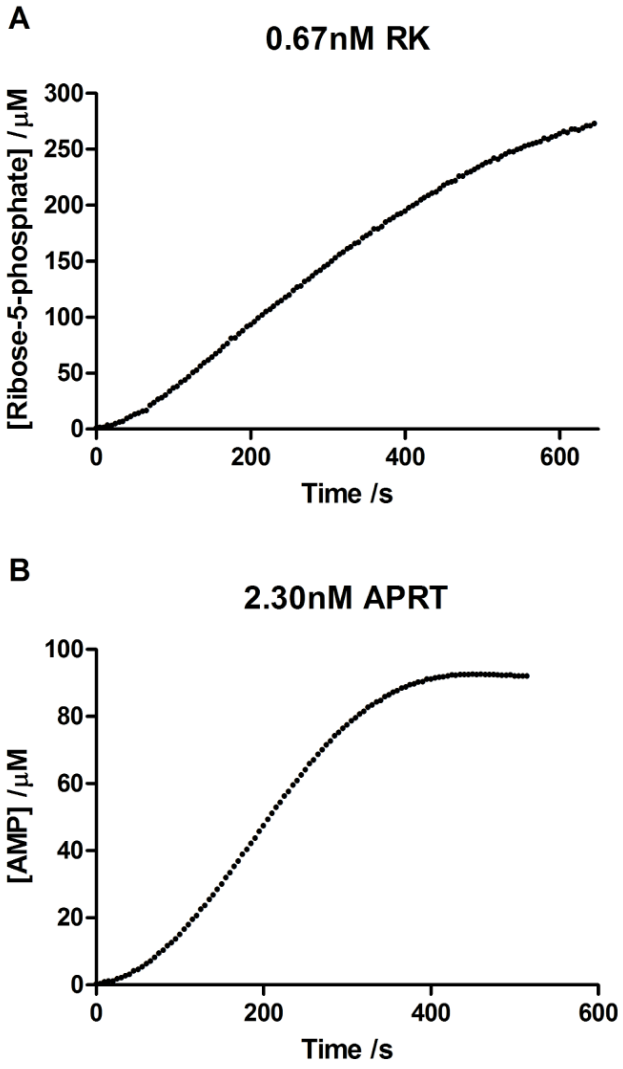

Figure 3.5. Representative progress curves obtained from the activity assays of ribokinas and adenine phosphoribosyl transferase. (a) RK progress curve assayed with [RK] = 0.67 nM, [Ribose] =5 mM, [ATP] = 3 mM. (b) APRT progress curve assayed with [APRT] = 2.30 nM, [PRPP] = 1.5 mM, [adenine-HCl] = 1.5 mM.

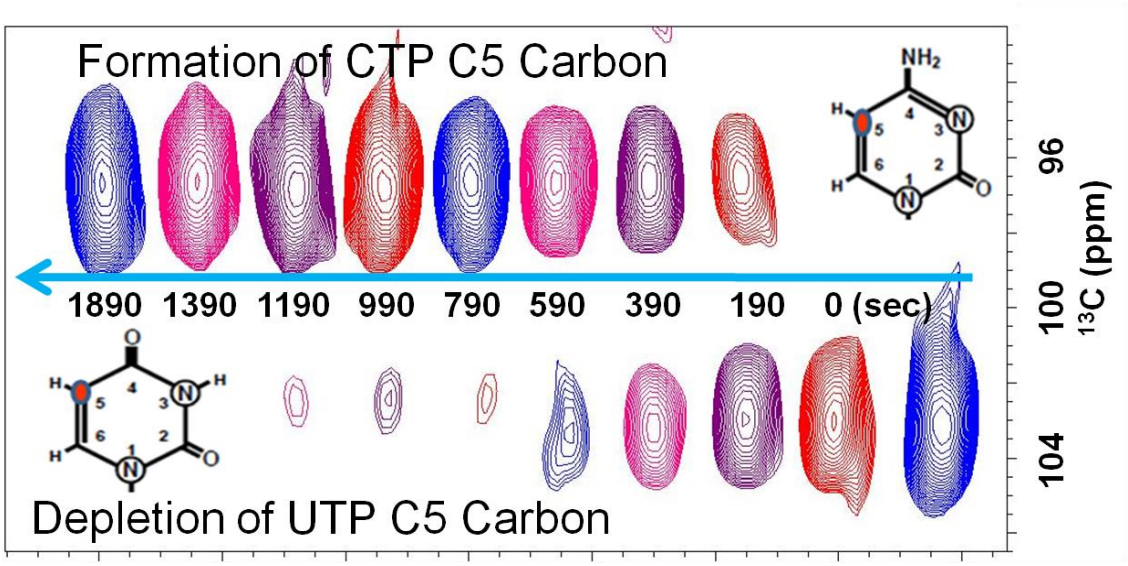

Figure 3.6. Activity assay for cytidine triphosphate synthetase monitored by ^{1}H-^{13}C HSQC NMR. The assay mixture (250 µl) contained 0.64 nM CTPS, 50 mM Tris-HCl (pH 8.0), 10 mM $MgCl_2$, 10 mM glutamine, 1 mM $^{15}N_2$-$^{13}C_9$-UTP, 1 mM ATP, 0.25 mM GTP and 90 % D_2O. The reaction was initiated by addition of glutamine and monitored over the course of 30 min. The arrow depicts the progression of the reaction.

Section 3.4: Discussion

The synthesis of nucleotides using the pentose phosphate pathway requires 17-18 enzymes (17 for systems using creatine phosphokinase for ATP regeneration) when starting from glucose or 12-13 when starting from ribose. When starting with glucose as the carbon source, 6 out of the 18 enzymes required for nucleotide synthesis are not commercially available and must be produced from overexpressing *E. coli* strains. Of these 6, only APRT was reported to have a significant activity of 350 U.

The other five are only moderately overexpressed with activities of 28-40 U, making the enzyme preparation labor intensive.[116,125,127] Similarly, when starting with

ribose as the carbon source, half of the enzymes required for nucleotide synthesis are not commercially available and other than ribokinase, most of the enzymes are only moderately active. Thus, our goal was to find cheaper avenues to make labeled nucleotides using constructs that highly overexpress several of the commercially unavailable enzymes.

In this study, six His-tagged recombinant proteins from the pentose phosphate pathway were, therefore, successfully expressed in *E. coli* and purified to homogeneity, yielding a single protein band of the expected molecular weight on SDS-PAGE for each protein (Figure 3.1). In the current study, the yields of pure recombinant protein, up to 25 mg per liter of crude *E. coli* supernatant, are higher than that obtained previously for purification of recombinant UPRT, APRT, XGPRT.[119] A number of steps were taken to improve the yield. Previous studies used vectors which contain additional features not present in the pET15b vector used in the current study. The pET15b vector contains only a His_6-tag and a thrombin cleavage site which facilitates straightforward purification and optional cleavage of the His_6-tag, should this be deemed to interfere with function; I did not find it necessary for any of the constructs as activities were similar or higher than previously reported. Finally, while the current study used affinity chromatography for the end stage, previous studies used streptomycin sulfate to precipitate the nucleic acids, ammonium sulfate to precipitate the proteins followed by a DEAE chromatographic step and a final ammonium sulfate precipitation steps.[125,127] Affinity chromatography is known to typically produce a higher protein yield and higher protein purity, compared to ammonium sulfate precipitations and gel filtration.[128] Use of uniform expression hosts

and single step affinity purification means that all six enzymes can be overexpressed and purified in two days, saving time and making the process less laborious.

In summary, His-tagged recombinant proteins have been purified to homogeneity, and found to possess comparable or superior activity to previously reported preparations. The method permits the production of substantial amounts of recombinant enzymes required for conducting enzymatic synthesis of nucleotides for biophysical studies such NMR spectroscopy, Raman spectroscopy and Mass spectrometry.

Chapter 4: Synthesis of site-specifically isotope-labeled nucleotides and their incorporation into IRE RNA for NMR studies

Section 4.1: Introduction

RNA is an established important player in cellular processes central to life. Beyond being a protein coding information carrier, RNAs are key regulators of gene expression in the form of riboswitches, miRNAs or large non-coding RNAs. Significantly, the amount of non-protein coding sequence appears to scale with organismal complexity to the extent that in humans, ~98.8 % of the DNA does not code for proteins; rather it is likely transcribed into RNA.[147] As a result RNAs are increasingly targeted for drug discovery and biophysical characterizations.[101–115,148] In spite of this centrality of RNA to biomedical science, I know far less about the 3D architectures of RNAs than those of proteins. For instance, as of September 2013, RNA accounts for only 1.1 % of the proportion of structures deposited in the Protein Data Bank (PDB) compared to 92.6 % for proteins.[149,150] This discrepancy arises from the difficulties in determination of RNA structures by either X-ray crystallography or nuclear magnetic resonance spectroscopy (NMR). The strong electrostatic repulsions between closely apposed phosphates groups with high negative charges on the RNA backbone as well as the inherent dynamic nature of the RNA molecules often preclude crystallization. Almost half of the RNA structures, for instance, deposited in the PDB were determined by X-ray crystallography and the other half by NMR spectroscopy, underscoring the centrality of NMR spectroscopy to tackle the structures of RNAs.[149] Advances in methodology,

sample preparation, isotopic labeling and spectrometer engineering have led to highly refined solution structures of several RNAs.[120–122,124,151–155]

Although NMR spectroscopy has demonstrated its potential to determine the structures and dynamics of RNAs, most high-resolution NMR structural studies have been satisfactorily applied to small RNAs (<25 nucleotides) using unlabeled and uniformly ^{1}H, ^{13}C, ^{15}N-labeled nucleotides.[123,124] The prevalence of structural data for small RNAs is due to several factors: (i) RNAs contain only four nucleotides, compared to protein's twenty amino acids, so that RNA's ^{1}H, ^{13}C, ^{15}N and ^{31}P nuclei tend to resonate in very narrow spectral ranges that lead to extensive chemical shift overlap. (ii) Larger RNA molecules have larger correlation times. This results in rapid NMR signal decay, reflected in broadened lines. (iii) Line broadening leads to diminished signal-to-noise ratios, thus rendering NMR spectra nearly useless. To address these problems, various labeling schemes have been proposed.[116,125,127,151,154,156–161]

However, structural and dynamics studies of RNA requires a different, more specific, approach to preclude cumbersome pulse programs and inaccurate data analysis from uniformly labeled RNA. For instance, it is known that ^{13}C-^{13}C residual dipolar, and direct one-bond scalar couplings are main contributors to relaxation in the micro- to millisecond time scales.[162–164] These strong couplings, present in uniformly labeled RNA, introduce undesired contributions to NMR relaxation dispersion-type experiments, and thus lead to erroneous data analysis and interpretation. Specifically, Thakur et al. had previously shown how dynamics measurements of R_1 longitudinal relaxation rates deviated from monoexponential decay for uniformly labeled RNAs in contrast to specifically labeled nucleotides.[159] As an added benefit, I have also shown how selective

labels effectively recover sensitivity and resolution, even when compared to constant-time NMR experiments. Hence, if not carefully taken into consideration, dipolar and scalar couplings of multi-spin systems may give rise to inaccurate dynamics measurements of non-exchangeable protons, e.g. pyrimidine's C6-H6. Given that all NMR-active nuclei influence relaxation rates, it follows that isolated nuclear two-spin systems would allow for accurate extraction of relaxation parameters. Unfortunately, to date, some of the techniques to obtain isolated two-spin systems have lacked both versatility, accessibility and reliability for production of site-specifically labeled RNA NMR samples.

To address the limitations of uniform labeling, five approaches are utilized to obtain site-specifically isotopically labeled RNA. (i) Total chemical synthesis of nucleotides, followed by solid-phase synthesis of RNA using phosphoramidite chemistry. This method is powerful in custom isotope incorporation in the RNA, but has problems of regio- and stereo-selectivity, along with low yields (<10 %).[165,166] (ii) *De novo* biosynthesis of NTPs, followed by *in vitro* RNA transcription produces labeled nucleotides at significant yields (<60 %).[167] This robust methodology comes at the cost of using ~18-23 enzymes, expensive precursor substrates, and inaccessibility to some labels. (iii) Biomass production of NMPs that are phosphorylated to NTPs for use in *in vitro* RNA transcription provides useful labeled nucleotides; however, the overall yield is low per labeled input metabolite, and isotopic scrambling often leads to inadequate suppression of ^{13}C-^{13}C couplings.[151,168,169] (iv) Selective biomass production of NMPs overcomes the isotopic scrambling problem with adequate suppression of ^{13}C-^{13}C couplings; however, the overall low yield remains an issue.[154,157–159,170–172] (v) Chemo-

enzymatic synthesis of nucleotides, followed by *in vitro* RNA transcription, is the most versatile of all methods developed thus far because of the potential to expand the range of labels accessible for various biophysical studies.[116]

To expand the range of labels accessible for various biophysical works, I use the chemo-enzymatic method to combine ribose (which has many commercially available site specific labels) with labeled uracil. As had been shown before by Santa Lucia et al.,[173] Kreutz et al. recently synthesized uracil using labeled potassium cyanide, and unlabeled bromoacetic acid and urea.[165] In particular, I present a streamlined and reliable chemical enzymatic synthesis of site-specifically labeled ^{13}C- and ^{15}N-pyrimidine nucleotides containing isolated two-spin systems in both the ribose and the nucleobase. With our method, I can incorporate ^{13}C and ^{15}N isotopes in uracil at any carbon site in the uracil ring, including nitrogens (Figure 4.1). The latter can be used simultaneously to address structural questions, such as secondary structure rearrangements or sub-populations at equilibrium. Herein, I report on the use of 6-^{13}C-1,3-$^{15}N_2$-uracil and 1′,5′-$^{13}C_2$-D-ribose as the building blocks of choice. Furthermore, I address the problems of accessibility, robustness, and more accurate dynamics measurements.

The chemo-enzymatic synthesis of site-specifically labeled uridine and cytidine nucleotides employs three to four enzymes from the pentose phosphate pathway (Figure 4.2). These enzymes are Ribokinase, RK (E.C. 2.7.1.15), which catalyzes the phosphorylation at the ribose C5′ position to produce ribose-5-phosphate (R5P).[129] Phosphoribosyl pyrophosphate synthetase, PRPPS (E.C. 2.7.6.1), catalyzes the addition of a β,γ-diphosphate from ATP to the C1′ position of R5P, activating it for the addition of a nucleobase.[130] Uridine phosphoribosyl transferase, UPRT (E.C. 2.4.2.9), catalyzes the

condensation between phosphoribosyl pyrophosphate and uracil to form uridine monophosphate.[131–133] Finally, CTP synthethase, CTPS (E.C. 6.3.4.2), is utilized in a separate reaction as the catalyst in the ATP-dependent production of CTP from UTP, using ammonia as the nitrogen source.[127,135] These enzymes have been previously cloned, expressed, purified and assayed; making their production in large milligram quantities nearly effortless.[100] Other enzymes and components used in the reactions are inexpensive and commercially available.

In this chapter, I show that the IRE RNA transcribed with our custom nucleotides exhibits improved NMR spectral properties and further provides more accurate dynamics measurements. Specifically, the IRE RNA showed enhanced relaxation properties, less signal crowding, and narrower linewidths as hypothesized. Moreover, the methods for the production of the site-specifically labeled nucleotides have been streamlined, becoming highly accessible to any biochemistry/NMR lab.

Section 4.2: Methods

4.2.1. Buffers and reagents:

All buffers were prepared in-house utilizing standard chemicals (Sigma-Aldrich, Fisher Scientific). Unless otherwise stated, all chemicals used were purchased from Sigma-Aldrich or Fisher Scientific.

4.2.2. Uridine triphosphate synthesis:

The site-specifically labeled 1′,5′,6-$^{13}C_3$-1,3-$^{15}N_2$-Uridine triphosphate was enzymatically synthesized *in vitro*. First, uridine monophosphate (UMP) was synthesized from uracil and ribose. The reaction was carried out in 50 mM Na_3PO_4 pH 7.5, 10 mM

$MgCl_2$, 2 mg/mL ampicillin, 10 mM DTT, 0.5 mM dATP, 100 mM creatine phosphate, 8 mM uracil, 10 mM ribose, 50 U/mL creatine kinase, 50 U/mL myokinase, 0.4 U/mL thermostable inorganic pyrophosphatase (New England Biolabs), 5 U/mL ribokinase, 3 U/mL phosphoribosyl pyrophosphate synthetase, and 5 U/mL uridine phosphoribosyl transferase. The reaction was incubated at 37 °C for 5 hours. UMP was then purified by boronate affinity chromatography and lyophilized to a powder. The powder was then resuspended, and assayed for UMP concentration by its UV trace at 262 nm wavelength (ε = 10,000 $M^{-1}cm^{-1}$). Our typical yield was 90 %.

Fresh UMP was then phosphorylated to synthesize UTP. The reaction was carried out in 70 mM Tris-HCl pH 7.5, 20 mM KCl, 20 mM $MgCl_2$, 2 mg/mL ampicillin, 10 mM DTT, 0.5 mM dATP, 100 mM creatine phosphate, 2.5 mM UMP, 5 µg/mL creatine kinase, 0.1 mg/mL BSA, and 50 µg/mL nucleoside monophosphate kinase (Roche). The reaction was incubated at 37 °C for 6 hours. UTP was then purified by boronate affinity chromatography and lyophilized to a powder. The powder was then resuspended, and assayed for UTP concentration by its UV trace at 262 nm wavelength (ε = 10,000 $M^{-1}cm^{-1}$). Our typical yield was >95 %. Consequently, our overall yield was >76 % using this method. The resuspended UTP was washed several times and finally stored as a 50 mM stock in 10 mM Tris-HCl pH 7.0, 1 mM EDTA at -20°C. The identity of all of the intermediates and products were confirmed by FPLC utilizing a reverse-phase analytical column.

Alternately, the phosphorylation of UMP can be achieved *in situ* immediately after its synthesis. Addition of 20 mM KCl and 50 µg/mL nucleoside monophosphate kinase from bovine liver (Roche), followed by incubation at 37 °C for 6 hours achieved

complete phosphorylation of UMP to UTP. The pH of the reaction was adjusted with either HCl or NaOH to fall between 7.5 and 8.0. In most cases, the reaction mixtures were also spiked with 0.2 mM dATP and 20 mM creatine phosphate. Our typical overall yield with this method was 90 % with respect to input uracil.

4.2.3. Cytidine triphosphate synthesis:

The site-specifically labeled 1′,5′,6-$^{13}C_3$-1,3-$^{15}N_2$-Cytidine triphosphate was enzymatically synthesized *in vitro* in a single-step reaction. The previously synthesized uridine triphosphate (UTP) was converted in a reaction with dATP and ammonium chloride, catalyzed by CTP synthetase. The reaction was carried out in 50 mM Tris-HCl pH 8.0, 10 mM $MgCl_2$, 2 mg/mL ampicillin, 4 mM dATP, 2 mM UTP, 20 mM ^{15}N-NH_4Cl, and 0.1 mg/mL CTP synthetase. The reaction was incubated at 37 °C for 6 hours. The reaction was then filtered through a 3,000 molecular weight cut-off filtering device. The flow-through was collected and assayed for CTP concentration by its UV trace at 273 nm wavelength (ε = 9,000 $M^{-1}cm^{-1}$). The recovered CTP at nearly quantitative yields was used directly in *in vitro* transcriptions. Our typical yield was 95 %.

4.2.4. RNA Preparation:

Iron Responsive Element RNA (5′GGAGUGCUUCAACAGUGCUUGGACGCUCC) was synthesized *in vitro* from synthetic DNA templates (Integrated DNA Technologies Inc.). The transcriptions were carried out in transcription buffer [40 mM Tris-HCl pH 8.0, 0.1 mM spermidine, 0.01 % Triton X-100, 10 mM DTT, 80 mg/mL PEG (8000MW)], supplemented with 2.0 U/mL thermostable inorganic pyrophosphatase (New England Biolabs, Inc.), 0.3 μM each DNA template, 10 mM $MgCl_2$, 5 mM NTPs (1.25 mM each NTP), and 0.25 mg/mL T7 RNA

polymerase. The T7 RNA polymerase was expressed in *E. coli* BL21(DE3) and purified on pre-packed Ni-NTA beads in column mode as previously described. The T7 promoter sequence used was 5′ CTA ATA CGA CTC ACT ATA G. The template strands of wild-type IRE RNA was 5′GGAGCGTCCAAGCACTGTTGAAGCACTC CTATAGTGAGTCGTATTAG. Two terminal 2'-O-methyl modifications in the template strands were introduced to substantially reduce transcript heterogeneity. All purchased DNA oligonucleotides were PAGE-purified. The transcription conditions were optimized by a sparse-matrix approach. The reactions were incubated at 37 °C for 3h. The reactions were then phenol-chloroform extracted and then ethanol-precipitated overnight with three volumes of absolute ethanol and 0.3 M sodium acetate pH 5.2. The precipitates were then re-suspended in a minimum amount of water and PAGE-purified in 8 M Urea/13 % acrylamide-bis (19:1) gels. The gel was UV-shadowed, the corresponding band was then excised and the RNA was then electro-eluted on an Elutrap electro-separation system (Schleicher and Schuell) at 200 V for 6-7 h. The elution fractions were pooled, concentrated and extensively dialyzed against a high-EDTA buffer (10 mM Na_3PO_4 or Tris-HCl pH 6.5, 10 mM NaCl, 10 mM EDTA) and a low-EDTA buffer (same as above, 0.2 mM EDTA). Prior to use, the RNA was heated to 90 °C for two minutes and immediately cooled on ice for 10 minutes to promote folding.

4.2.5. Nuclear Magnetic Resonance:

NMR experiments were conducted on the IRE RNA to show the incorporation of the newly synthesized site-specifically labeled nucleotides from above. All NMR samples contained 0.25 mM 4,4-dimethyl-4-silapentane-1-sulfonic acid (DSS) for ^{1}H and ^{15}N chemical shift referencing. IRE RNA was kept at a concentration of 0.2 – 1 mM. One-

dimensional proton, two-dimensional homo- and hetero-nuclear Overhauser (NOE), two-dimensional constant- and non-constant time ^{13}C and ^{15}N heteronuclear single quantum correlation (HSQC), three-dimensional ^{1}H-^{1}H-^{13}C NOESY-HSQC, and three-dimensional ^{1}H-^{13}C-^{15}N out-back HCN spectra were collected at 25 °C on a 600 MHz Bruker Avance III spectrometer equipped with a HCN triple resonance cryoprobe. All NMR data were processed using TopSpin 3.2, NMRpipe/NMRDraw, and NMRviewJ. The statistical quality factor utilized for the data fits was chi-squared (χ^2), as given by the equation below,

$$\chi 2 = \sum \frac{(E_i - O_i)^2}{E_i}$$

where E_i is the expected value, O_i is the observed value for any given measurement.

Section 4.3: Results

4.3.1. Synthesis of site-specifically labeled UTP

In this work, I aimed to chemo-enzymatically synthesize site-specifically labeled pyrimidine nucleotides, UTP and CTP. These were then used for *in vitro* transcriptions of the IRE RNA (Figure 2.1c). In order to synthesize nucleotides, I expressed and purified four enzymes from the pentose phosphate pathway: ribokinase, phosphoribosyl pyrophosphate synthetase, uridine phosphoribosyl transferase, and cytidine triphosphate synthetase. As described in our previous work and in Chapter 3,[100] I induced the expression of the His_6-tagged enzymes in bacterial systems by the addition of L-(+)-arabinose and IPTG to the cell cultures. The isolated proteins were purified by immobilized metal affinity chromatography. From a one liter culture, 21 mg of ribokinase

(RK), 5 mg phosphoribosyl pyrophosphate synthetase (PRPPS), 15 mg of uridine phosphoribosyl transferase (UPRT), and 25 mg of cytidine triphosphate synthetase (CTPS) were isolated at or above 90 % purity. Their specific activities were also consistent with our previous findings: 70 U/mg; 22 U/mg; 150 U/mg and 120 U/mg, respectively. It was determined that given the purity and specific activity of the enzymes, they did not need further purification or His_6-tag cleavage. These enzymes were then used for the subsequent nucleotide synthesis reactions.

Prior to the synthesis of uridine triphosphate, I aimed to synthesize one of its building blocks: uracil. Its chemical synthesis had been previously described,[173] and has now been optimized to obtain yields of synthesis >82 %.[165] This readily accessible reaction consisted of a three-step coupling of commercially available precursor compounds: 2-bromoacetic acid; $^{15}N_2$-urea; and K^{13}CN (See Figure 4.1). Using these reagents, the final ^{13}C-labeled position in the uracil ring was C6. The synthesis was optimized to obtain gram quantities at very low expense. The identity of 6-$^{13}C_1$-1,3-$^{15}N_2$-uracil was confirmed by nuclear magnetic resonance (NMR), as previously described.[165]

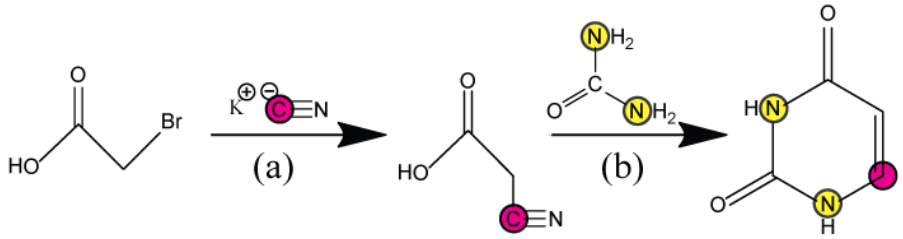

Figure 4.1. Chemical synthesis of uracil. (a) sodium carbonate, pH 9, 3 h at 80 °C, 20 h at room temperature; (b) urea in acetic anhydride, 30min at 90 °C, 5 % Pd/BaSO4 in 50 % aqueous acetic acid, 36 h at room temperature; (c) ribokinase, phosphoribosyl pyrophosphate synthetase, uridine phosphoribosyl transferase, nucleoside monophosphate kinase in sodium phosphate pH 7.5, 10 h at 37 °C; (d) cytidine triphosphate synthetase in Tris-HCl pH 8.0, 6 h at 37 °C. Magenta: ^{13}C; yellow: ^{15}N.

The *in vitro* one-pot, two-step synthesis of UTP was readily accomplished in high yields, > 80 %. The first step in the reaction is the formation of UMP from 1′,5′-$^{13}C_2$-ribose (omicron biochemicals) and 6-$^{13}C_1$-1,3-$^{15}N_2$-uracil (Figure 4.2). The reaction proceeded to completion within 5 hours, with nearly complete depletion of uracil as seen in Figure 4.3. Of note, I utilized a slight molar excess of ribose, as they were shown to have better reaction yields than when utilizing equimolar amounts or excess uracil (data not shown).

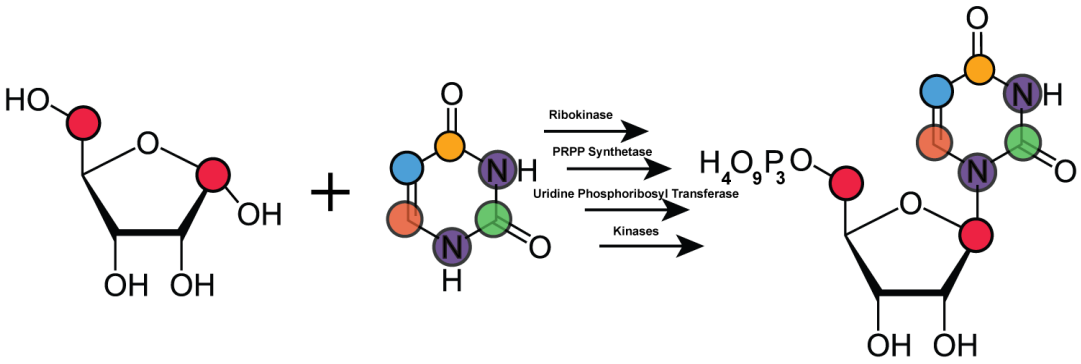

Figure 4.2. Two-step chemo-enzymatic synthesis of uridine triphosphate. Notice the coloring scheme of the uracil moiety, in relation to its enzymatic synthesis, where every carbon in the ring can be differentially labeled. The first step is carried out through uridine phosphoribosyl transferase; the second consists of the phosphorylation of UMP. The reaction mixture consists of ribokinase, phosphoribosyl pyrophosphate synthetase, uridine phosphoribosyl transferase, nucleoside monophosphate kinase in sodium phosphate pH 7.5, and 10 h at 37 °C.

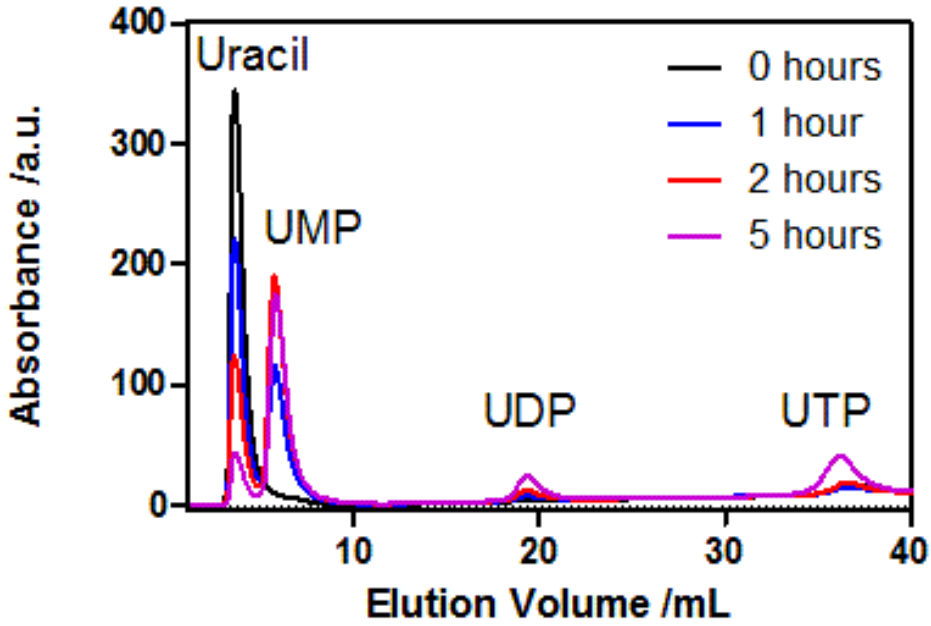

Figure 4.3. Chromatography profile of the synthesis of uridine monophosphate. Reverse-phase high-pressure liquid chromatography reveals the depletion of uracil with concomitant synthesis of UMP. Notice that at five hours (purple), this reaction begins non-specific phosphorylations of UMP. Leftover uracil corresponds to the 1.2 molar excess in comparison to ribose used in the reaction.

To verify the synthesis of UMP, I carried out two-dimensional HSQC spectroscopy experiments. These experiments were used as a direct continuous assay of the enzymatic reactions. To our advantage, the chemical shift of C1′ of ribose and UMP are vastly different in both proton and carbon dimensions. Therefore, by observing the slow exchange process of the C1′-H1′ of the substrate (ribose) to product (UMP), I confirmed the synthesis of UMP at nearly quantitative yields (Figure 4.4). Additionally, I monitored the C6-H6 spin system of uracil (substrate), since it also showed a drastic chemical shift change upon coupling to ribose. The ^{13}C-^{1}H HSQC experiments also revealed conversion of ribose to UMP (Figure 4.5). Finally, as an additional orthogonal

method of verifying the synthesis of our mononucleotide, I performed a two-bond ^{15}N-^{1}H HSQC experiment, where I correlate both H5 and H6 of the uracil base to both nitrogens, N1 and N3, via through-bound correlations. As expected, the chemical shift differences of the substrate and product were substantially different for the ^{1}H-^{15}N correlations, thus allowing us to follow and confirm the progress of the reaction (Figure 4.6). Altogether, I showed from HPLC and NMR results that 1′,5′-$^{13}C_2$-1,3-$^{15}N_2$-UMP was synthesized from ribose and uracil in five hours at nearly quantitative yields.

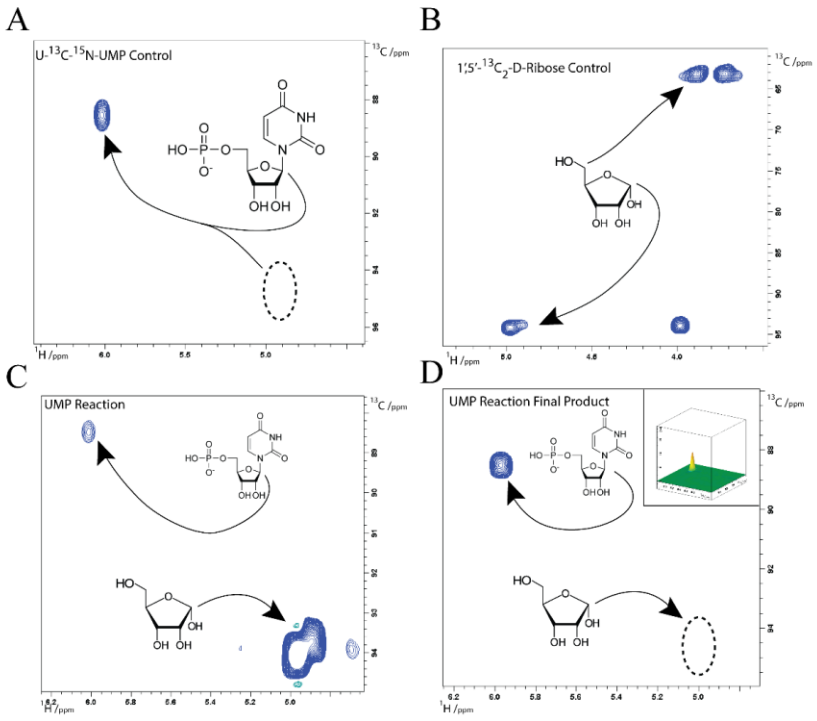

Figure 4.3. Synthesis of uridine monophosphate observed by ^{13}C-^{1}H HSQC NMR of the ribose ring. (A) Positive control: Uniformly labeled $^{13}C/^{15}N$ uridine monophosphate, observing the C1' moiety. Dotted circle: expected site of C1′ resonance as free ribose. (B) Negative control: 1′,5′-$^{13}C_2$-D-ribose, observing both C1′ and C5′ resonances. (C) Early time point of the chemo-enzymatic synthesis of UMP. Notice the appearance of a resonance at the same chemical shift as the positive control, corresponding to the C1′ of the newly formed UMP. (D) End point of the synthesis of UMP, showing complete formation of UMP and depletion of ribose. Inset: three-dimensional view of the same window to show that there is no trace of substrate left.

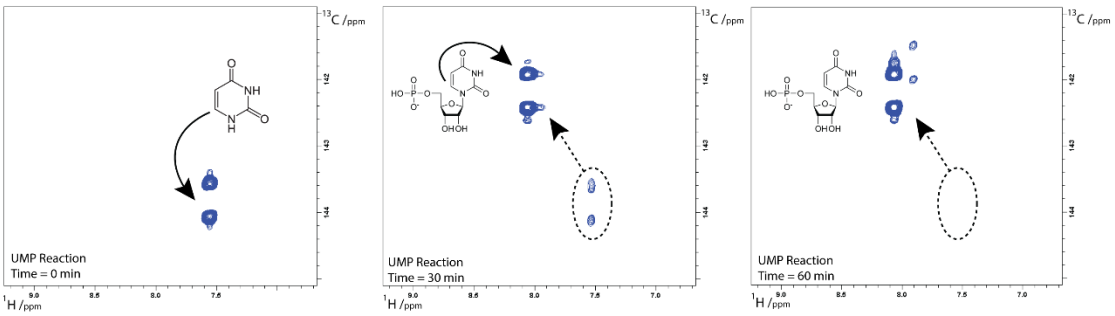

Figure 4.5. Time course of the synthesis of uridine monophosphate observed by ^{13}C-^{1}H HSQC NMR of the uracil ring. From left to right, notice how the resonances corresponding to C6-H6 shift upfield on the ^{13}C dimension and downfield on the ^{1}H dimension as the reaction progresses. After 60 minutes, the resonances corresponding to uracil's C6-H6 have completely disappeared. This experiment used ^{13}C-^{15}N uniformly labeled uracil as a substrate, hence the doublets observed.

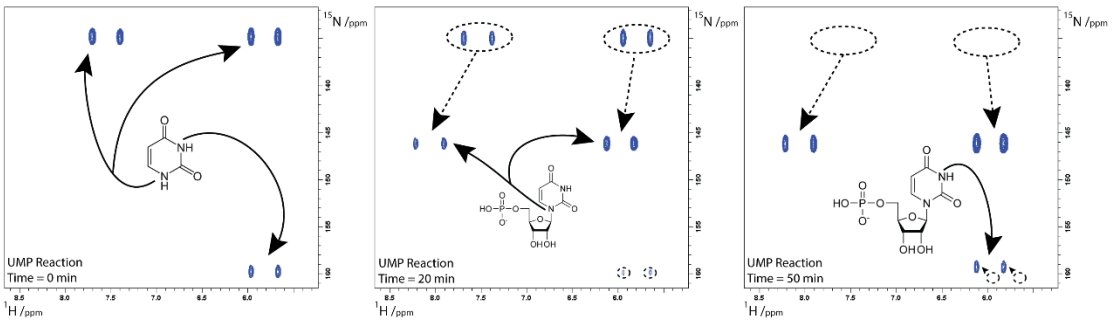

Figure 4.6. Time course of the synthesis of uridine monophosphate observed by two-bond ^{15}N-^{1}H HSQC NMR of the uracil ring. From left to right, notice how the resonances corresponding to H5-N1 and H6-N1 shift downfield both on the ^{15}N and ^{1}H dimensions as the reaction progresses. Meanwhile, the H5-N3 resonances slightly shift downfield on the ^{1}H dimension and upfield on the ^{15}N dimension. After 60 minutes, the resonances corresponding to uracil's H5-N1, H6-N1 and H5-N3 have completely disappeared. This experiment used ^{13}C-^{15}N uniformly labeled uracil as a substrate, hence the doublets observed.

To our surprise, at the end of the UMP synthesis reaction, a significant amount of UDP and UTP had been formed. These were products of non-specific phosphorylation. For this reason, I hypothesized that adding the minimal components needed for nucleoside monophosphate kinase (NMPK) to function would deplete UMP and phosphorylate it through UTP. Addition of KCl and NMPK along with a small replenishment of dATP and creatine phosphate enabled straightforward and effective phosphorylation; this was the second step of our reaction. The HPLC chromatograms indicated a negligible amount of residual substrates or intermediates (Figure 4.7). The newly synthesized UTP was then purified by boronate affinity chromatography; a representative chromatogram is shown in Figure 4.8. Although the enzymatic reactions appeared to have a quantitative yield, the recovery of isolated product after purification was nearly 90 %. I presume that some of the indispensable reaction components such as DTT may have interfered with the chemistry of the purification due to their diol functional groups. As well, it had been suggested that highly charged groups, i.e. UTP, may also interfere with binding to the solid phase of the column.[127]

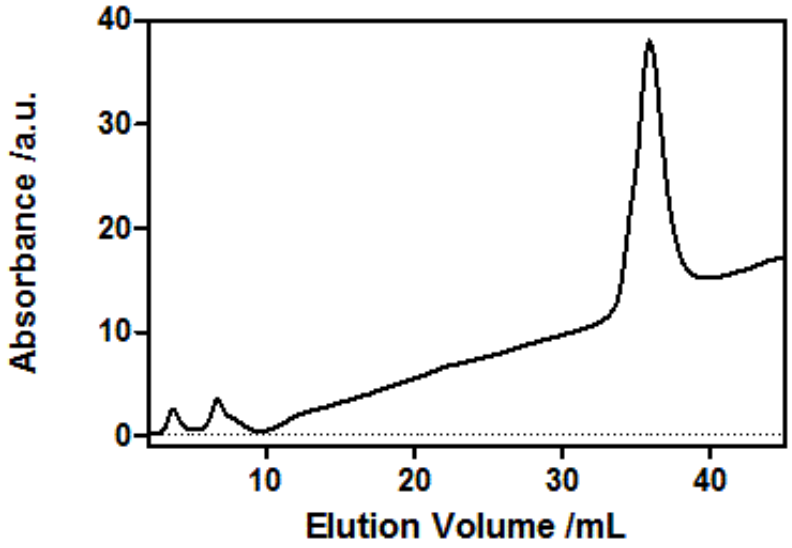

Figure 4.7. Chromatography profile of the phosphorylation of uridine monophosphate. Reverse-phase FPLC reveals the depletion of UMP and the appearance of UTP. Notice that there is no detectable UDP in the chromatographic trace.

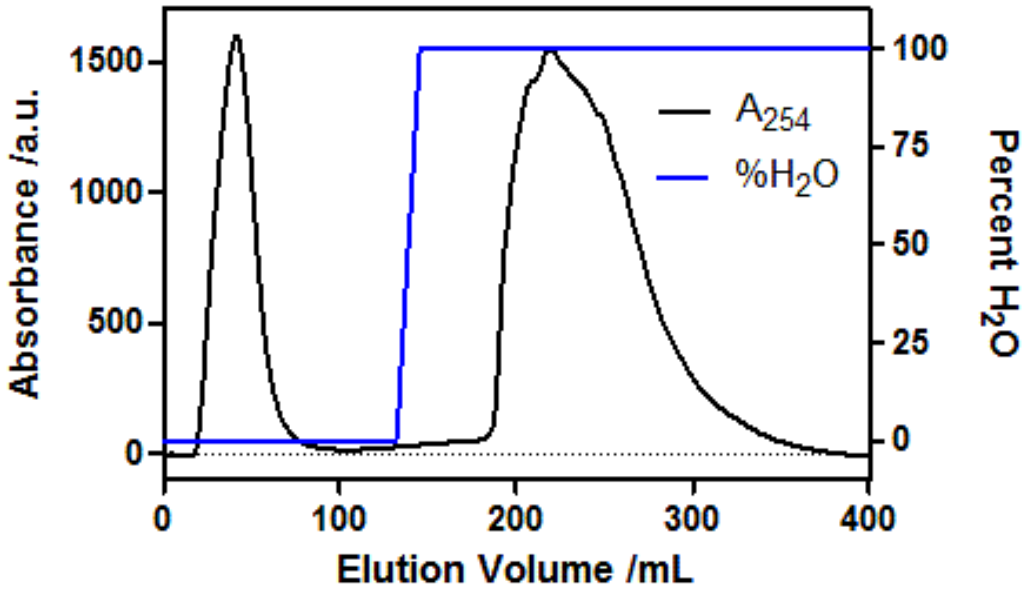

Figure 4.8. Boronate purification of uridine triphosphate. Fast-performance liquid chromatography purification of nucleotides on pre-packed Affigel boronate beads. The first peak in the chromatogram represents unbound sample, i.e. dATP. The second broad peak represents the eluted nucleotides over the course of several column volumes.

Before the freshly made UTP was used directly for our downstream applications, I performed a series of quality control experiments. The identity of 1′,5′,6-$^{13}C_3$-1,3-$^{15}N_2$-UTP was confirmed by FPLC and NMR (Figure 4.9). First, one dimensional ^{13}C and ^{31}P spectra were collected to confirm the incorporation of 6-^{13}C in the uracil ring and the phosphorylation stage of UTP, respectively. As seen in Figure 4.9a, one major peak is observed near 146 ppm, which represents the C6 moiety. The smaller peak observed ~104 ppm likely corresponds to an impurity. The phosphorous one-dimensional spectrum confirmed the presence of all three phosphate groups attached to UTP (Figure 4.9c). The presence of both 1′- and 5′-^{13}C was confirmed by a one dimensional ^{13}C spectrum (Figure 4.9e). Next, I carried out a series of two-dimensional experiments that confirmed our one-dimensional results. These were 2D ^{15}N- and ^{13}C-^{1}H HSQC experiments, our results showed the labeling of both base nitrogens, C6, C1′ and C5′ (Figure 4.9b,d,f). Altogether, our results showed us that our newly synthesized UTP had incorporated all the site-specific ^{15}N and ^{13}C isotopes, and that its phosphorylation state was adequate for use in *in vitro* RNA transcriptions.

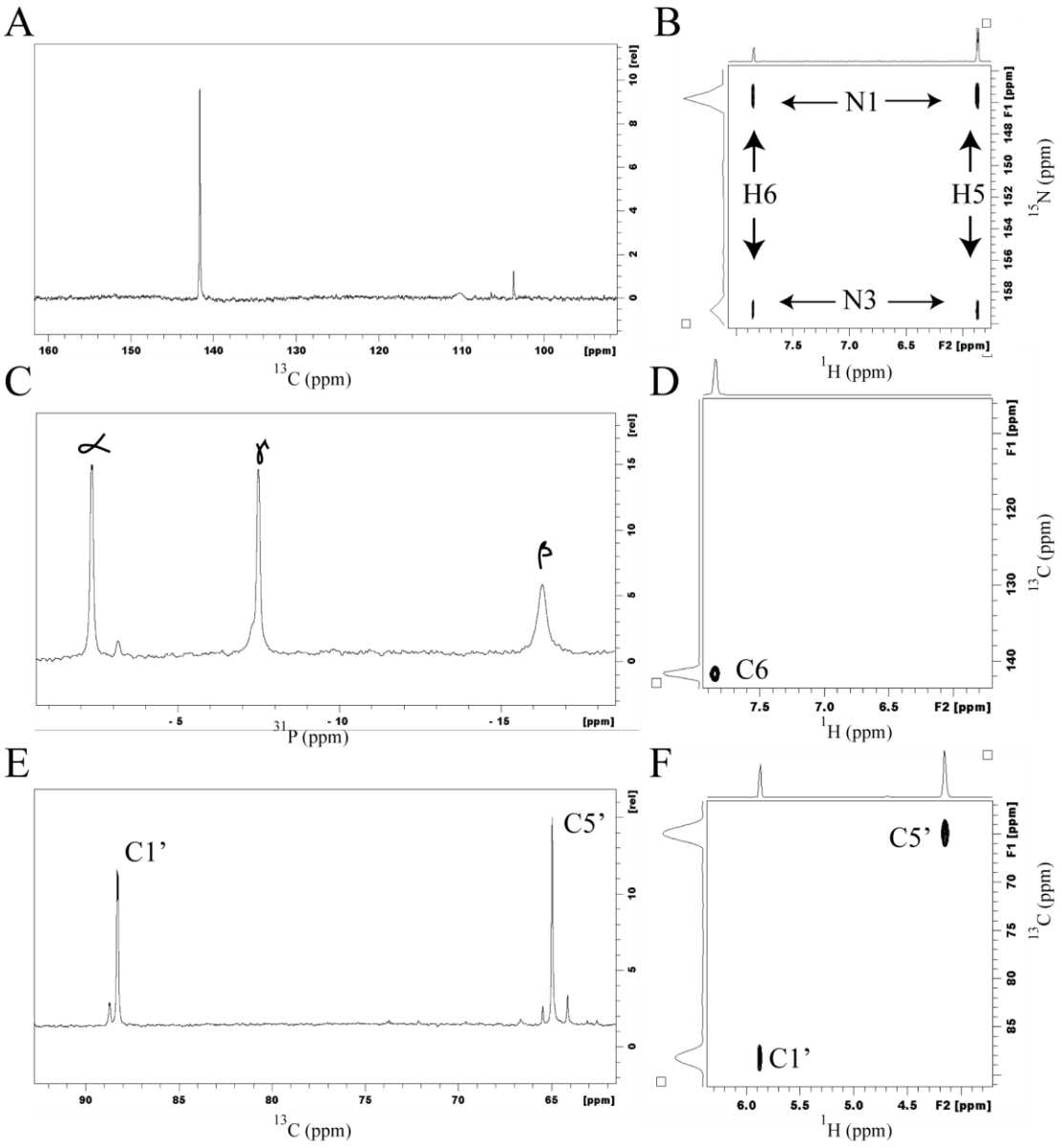

Figure 4.9. Spectra of 1′,5′,6-$^{13}C_3$-1,3-$^{15}N_2$-uridine triphosphate. (A) One-dimensional carbon spectrum, showing the only labeled carbon in the uracil base. (B) Two-dimensional two-bond ^{15}N-^{1}H HSQC spectrum, showing resonances of H5-N1, H6-N1, H5-N3, and H5-N1. (C) One-dimensional phosphorous spectrum, showing all phosphate moieties in UTP. (D) Two-dimensional ^{13}C-^{1}H HSQC spectrums showing C6 of UTP and the absence of C5. (E) One-dimensional carbon spectrum, showing the two carbon atoms in the ribose ring. (F) Two-dimensional ^{13}C-^{1}H HSQC spectrum, showing both C1′ and C5′ of the ribose region, notice the lack of J-coupling.

4.3.2. Synthesis of site-specifically labeled CTP

Next, I aimed to synthesize site-specifically labeled CTP from our freshly made UTP. In our reactions, 1′,5′,6-$^{13}C_3$-1,3,4-$^{15}N_3$-CTP was synthesized by the ATP-dependent amination of 1′,5′,6-$^{13}C_3$-1,3-$^{15}N_2$-UTP with $^{15}NH_4Cl$ using CTP synthetase, as shown in Figure 4.10. Potential substrates for the amination include both L-glutamine and ammonia, with nearly similar catalytic efficiencies.[174,175] For our purposes, I utilized $^{15}NH_4Cl$ as our nitrogen source.

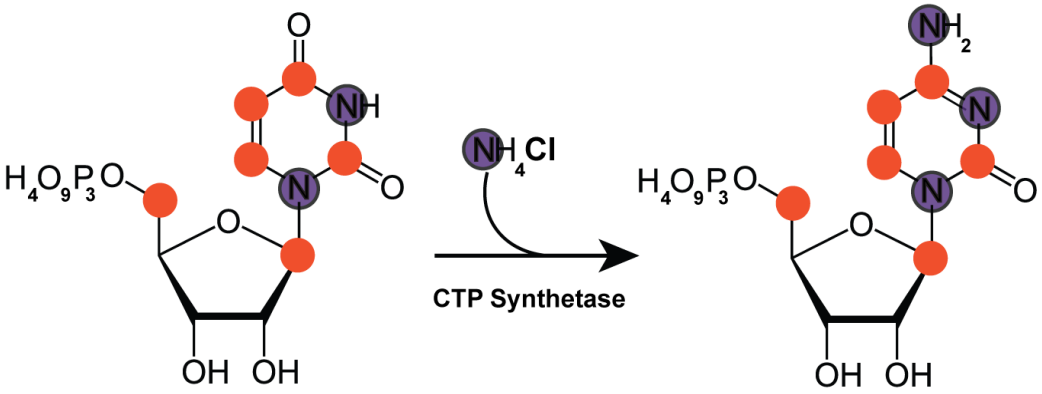

Figure 4.10. One-step enzymatic synthesis of cytidine triphosphate. CTP synthetase catalyzes the amination of UTP on C4. As mentioned above, the uracil ring, and thus the cytidine too, may be selectively labeled on any carbon.

After optimizing the reaction conditions, I obtained nearly quantitative CTP synthesis. The reaction reached completion at 4 h, as evidenced by our FPLC chromatograms (Figure 4.11). In contrast to UTP, CTP was not purified by boronate chromatography because the enzymatic reaction was performed under *in vitro* transcription-like conditions. That is, the buffer components and salt conditions were within the same order of magnitude of those used in *in vitro* transcriptions. Specifically, I

filtered the reaction through a 3,000 Da molecular weight cut-off filtering device to separate the enzyme from the reaction mixture. Therefore, I virtually obtained quantitative yields from our enzymatic reactions. After confirming the identity of 1′,5′,6-$^{13}C_3$-1,3,4-$^{15}N_3$-CTP by FPLC, one-, and two-dimensional NMR, the freshly made CTP was used directly for *in vitro* RNA transcriptions without further purifications.

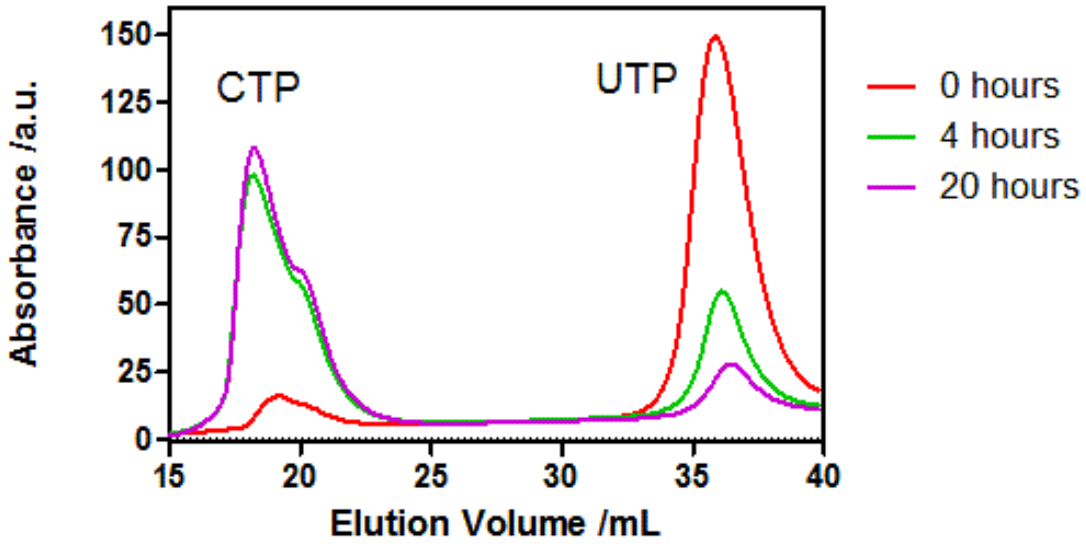

Figure 4.11. Representative chromatography profile of the synthesis of cytidine triphosphate. Reverse-phase high-pressure liquid chromatography reveals the depletion of UTP with concomitant synthesis of CTP. Synthesis of CTP ends after four hours.

4.3.3. Structural analysis of the IRE RNA synthesized with site-specifically labeled nucleotides

Our enzymatic reactions, in milliliter scales, yielded milligram amounts of site-specifically ^{13}C- and ^{15}N-labeled nucleotides that were then used in *in vitro* transcriptions of the IRE RNA (Figure 2.1c). This 29-nucleotide 5′ untranslated region hairpin has also been heavily studied due to its role in cellular iron homeostasis, as detailed in chapters 1 and 2 herein.[66,68] This RNA is an excellent system for solution NMR dynamics studies as many of its residues are highly flexible, especially the stem-bulged cytidine

nucleotide.[62,66,87] Pardi et al. and Hall et al. have carried out dynamics measurements of this RNA, thus providing us with a reference and a point of comparison for our studies.[62,87]

The IRE RNA was *in vitro* transcribed using our site-specifically labeled nucleotides, then purified and characterized by NMR. The initial characterization for our construct consisted of one-dimensional proton experiments that confirmed the formation of secondary structure. Indeed, the IRE RNA showed a number of resonances in the imino proton region, which correspond to base-pair hydrogen bonding (shown in the following chapter, Figure 5.3).

The site-specific labeling of these RNAs significantly reduced spectral crowding, eliminated ^{13}C-^{13}C scalar couplings, and increased the signal-to-noise ratios. To show that our specifically labeled RNAs exhibited these characteristics, I performed a series of two-dimensional experiments in the RNA showcasing $^{13}C/^{15}N$ uniform, uridine-only, or our custom-made nucleotides. For the IRE RNA, the ^{13}C-^{1}H correlation spectra focused in the ribose region (3.6 – 6 ppm ^{1}H; 60 – 95 ppm ^{13}C) of these three labeling schemes clearly showed the uncluttering of the spectral window (Figure 4.12). Of note, from our results I can argue that RNAs shorter than 30 nucleotides already show significant uncluttering just by segmental labeling schemes, i.e. $^{13}C/^{15}N$ uridine-only (Figure 4.12b). However, the absence of resonances arising from C2′, C3′ and C4′ further simplify the spectra and provide other advantages addressed below.

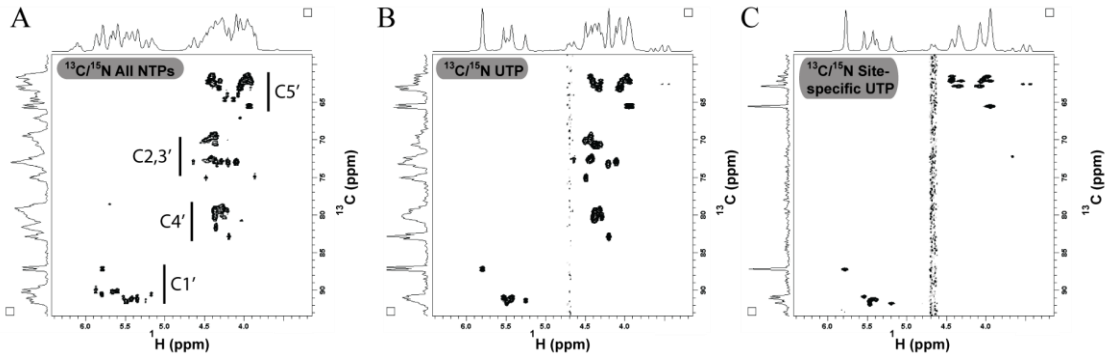

Figure 4.12. ^{13}C-^{1}H correlation spectra of the ribose region of the IRE RNA under different labeling conditions. (A) Two-dimensional ^{13}C-^{1}H HSQC spectrum of a uniformly-labeled IRE RNA. (B) Two-dimensional ^{13}C-^{1}H HSQC spectrum of a UTP-only uniformly-labeled IRE RNA. (C) Two-dimensional ^{13}C-^{1}H HSQC spectrum of a 1′,5′-$^{13}C_2$-ribose site-specifically-labeled IRE RNA showing the complete disappearance of resonances corresponding to C2′, C3′ and C4′ sites.

Further inspection of the ^{13}C-^{1}H HSQC spectra showed the absence of ^{13}C-^{13}C scalar couplings, since only positions 1′ and 5′ contained ^{13}C isotopes in the ribose ring (Figure 4.13). This is a very important feature since it eliminated the need of decoupling and the use of constant-time modules for refocussing $^{1}J_{CC}$ at the expense of lower sensitivity and limited spectral resolution.[128,158] Long delays in pulse programs sizably reduce resonance intensities of large RNAs due to rapid signal decay, often leading to complete signal loss.[128] Lastly, in combination with the use of cryo-cooled probes,[176,177] our site-specifically labeled RNAs were shown to provide better signal-to-noise ratios than uniformly labeled constructs. This was expected, as one of the main signal decay pathways – through dipolar couplings– was effectively reduced by our labeling schemes.

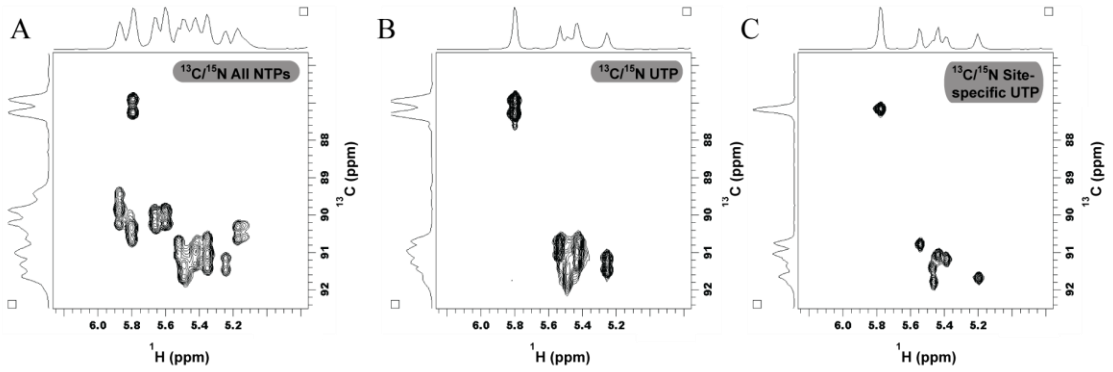

Figure 4.13. Site-specific labeling of the IRE RNA eliminates ^{13}C-^{13}C J-coupling. Correlation spectra of the C1′ ribose region of the IRE RNA under different labeling conditions, all images are zoomed-in versions of Figure 4.12. (A) Two-dimensional ^{13}C-^{1}H HSQC spectrum of a uniformly-labeled IRE RNA. (B) Two-dimensional ^{13}C-^{1}H HSQC spectrum of a UTP-only uniformly-labeled IRE RNA. (C) Two-dimensional ^{13}C-^{1}H HSQC spectrum of a 1′,5′-$^{13}C_2$-ribose site-specifically-labeled IRE RNA showing the absence of J-coupling at the C1′ site.

Additionally, I synthesized an IRE RNA with our site-specifically labeled CTP. I aimed to identify the degree of overlap between U and C residues, so as to prepare a doubly site specifically-labeled RNA. To our surprise, all the qualitative spectra collected on the CTP-labeled IRE RNA showed no major overlap issues in any of the regions observed: C1′; C5′; or C6 (Figure 4.14). From our results, I determined that utilizing an RNA sample with both C and U would be of our best interest for the subsequent relaxation dispersion analyses.

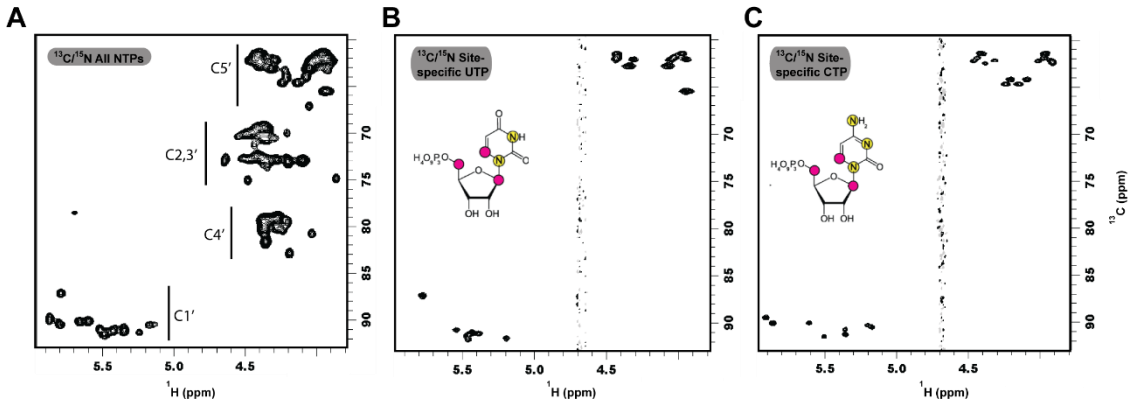

Figure 4.14. Site-specific labeling of both C and U in the IRE RNA does not cause overlap. By labeling both residues separately, I determined that the spectral quality remained untouched, and was amenable for dynamics studies of the construct. (A) ^{13}C-^{1}H HSQC experiment of a uniformly ^{13}C/^{15}N labeled IRE RNA, showing all ribose residues. (B) Same as (a), for a 1′,5′,6-$^{13}C_2$-1,3-$^{15}N_2$-UTP labeled IRE RNA. (C) Same as (a), for a 1′,5′,6-$^{13}C_2$-1,3,4-$^{15}N_3$-CTP labeled IRE RNA.

To further show the improvement in spectral quality by utilizing site-specifically labeled nucleotides, I evaluated linewidths and signal-to-noise ratios of two-dimensional spectra. Specifically, I compared 2D ^{13}C-^{1}H HSQC experiments from uniformly ^{13}C/^{15}N and U/C site-specifically labeled IRE RNAs. Interestingly, when observing all regions, C1′, C5′, and C6, I noticed a marked improvement in the linewidths of every resonance (Figure 4.15a-c). The narrower linewidths would prove more important to reduce peak overlap in larger RNA samples, i.e. >70 nt. When extracting one dimensional planes from the experiments, I did not observe a sizeable improvement in signal-to-noise ratios. Nonetheless, I exploited the C5′ methylene moiety in CH_2-optimized transverse relaxation-optimized spectroscopy (TROSY) experiments, selecting for the H component, the sharpest from the collection of eight peaks in an entirely de-coupled spectrum (Figure 4.15d).[178,179] These experiments were contrasted with traditional CH_2-optimized HSQC

experiments.[179] When extracting a one dimensional plane from the experiment, I observed a ~2:1 improvement in signal-to-noise ratios when utilizing our site-specifically labeled IRE RNA (Figure 4.15d-inset). Interestingly, the ^{13}C linewidths appeared to be larger than in non-TROSY experiments. This artifact is possibly due to a different spectral resolution utilized in the experimental parameters. This recovery of signal in contrast to a traditional HSQC experiment would prove useful in larger RNAs as well. Altogether, I have shown that our site-specifically labeled nucleotides have improved both signal-to-noise ratios and linewidths, as well as reduce spectral crowding in our 29-nt IRE RNA.

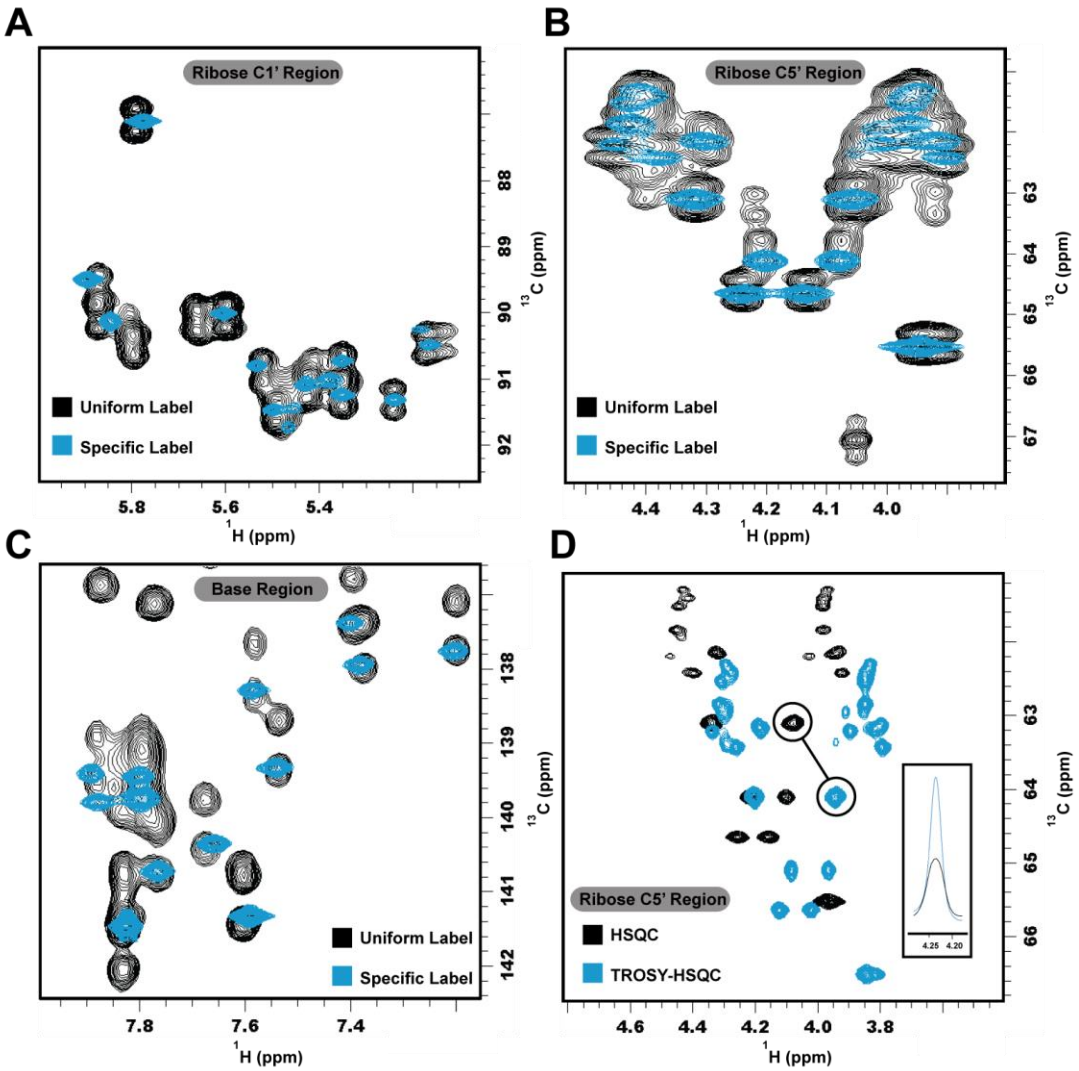

Figure 4.15. Site-specifically labeled RNA reduces spectral crowding and increases sensitivity. (A) 2D ^{13}C-^{1}H HSQC experiment focused in the C1′-H1′ region of the IRE RNA comparing a ^{13}C/^{15}N uniformly labeled and a site-specifically labeled sample. Notice that all peaks are resolved in the latter, along with a decreased linewidth for each. (B) Same as (a), focused in the C5′-H5′ region. (C) Same as (a), focused in the C6-H6 region. This region is of utmost importance as overlap is severe due to C8-H8 peaks from purines. (D) 2D ^{13}C-^{1}H methylene-optimized TROSY-HSQC provides increased signal-to-noise ratios compared to HSQC experiments even for RNAs as short as the IRE RNA (29 nt). Inset: 1D spectrum of the two peaks circled, notice the near two-fold increase in signal-to-noise ratio on the TROSY-based experiments. Note that in (d), the apparent shifting in the peak positions arises from the TROSY effect, in which from a collection of eight peaks, the bottom right is chosen. For more information, see Miclet et al.[178] The differences in ^{13}C linewidths may arise from different spectral resolutions used in the experiments.

I then aimed to assign the minimal set of resonances needed for a structural and dynamic analysis of the IRE RNA. I employed a combination of traditional and novel assignment methods, mostly based in the work by Dayie.[180] In his work, he presents a straightforward and rapid assignment protocol, consisting of a few experiments that aim to assign exchangeable base protons and their covalently attached nitrogens, followed by non-exchangeable base protons and their attached carbons. Then, base protons are correlated to ribose H1′ protons. In our work, I followed this methodology with minimal modifications. A series of two- and three-dimensional experiments allowed us to accurately and rapidly assign most resonances to their corresponding atomic nucleus in the RNA of interest. Exchangeable imino proton assignments (H1 and H3) were performed by a series of 2D ^{15}N-^{1}H HSQC and 2D ^{1}H-^{1}H NOESY experiments. Next, I confirmed base pair formation by 2D HNN COSY experiments. Additionally, I observed most C1′-H1′, C5′-H5′, C5′-H5″, and C6-H6 resonances by 2D ^{13}C-^{1}H HSQC experiments. By combining the information from imino protons and their through space connectivities to H2 or H4 due to the geometry of base pairing, I were able to assign those nuclei. I followed by performing a 3D HCCNH experiment, to assign H5, H6, and (G)H8 resonances. Taking advantage of our pyrimidine-only labeling scheme, I performed a 3D ^{1}H-^{1}H-^{13}C NOESY-HSQC experiment. In this experiment, I performed a sequential through-space walk from H1′ to its own intra "i" nucleotide H6 on to the sequential "i+1" nucleotide H1′ (Figure 4.16a). Using our labels, I avoid the spectral cluttering arising from H1 to H8 connectivities, and also H1 to other protons within distance, i.e. H2′, H3′, H4′, H5 (Figure 4.16b,c).

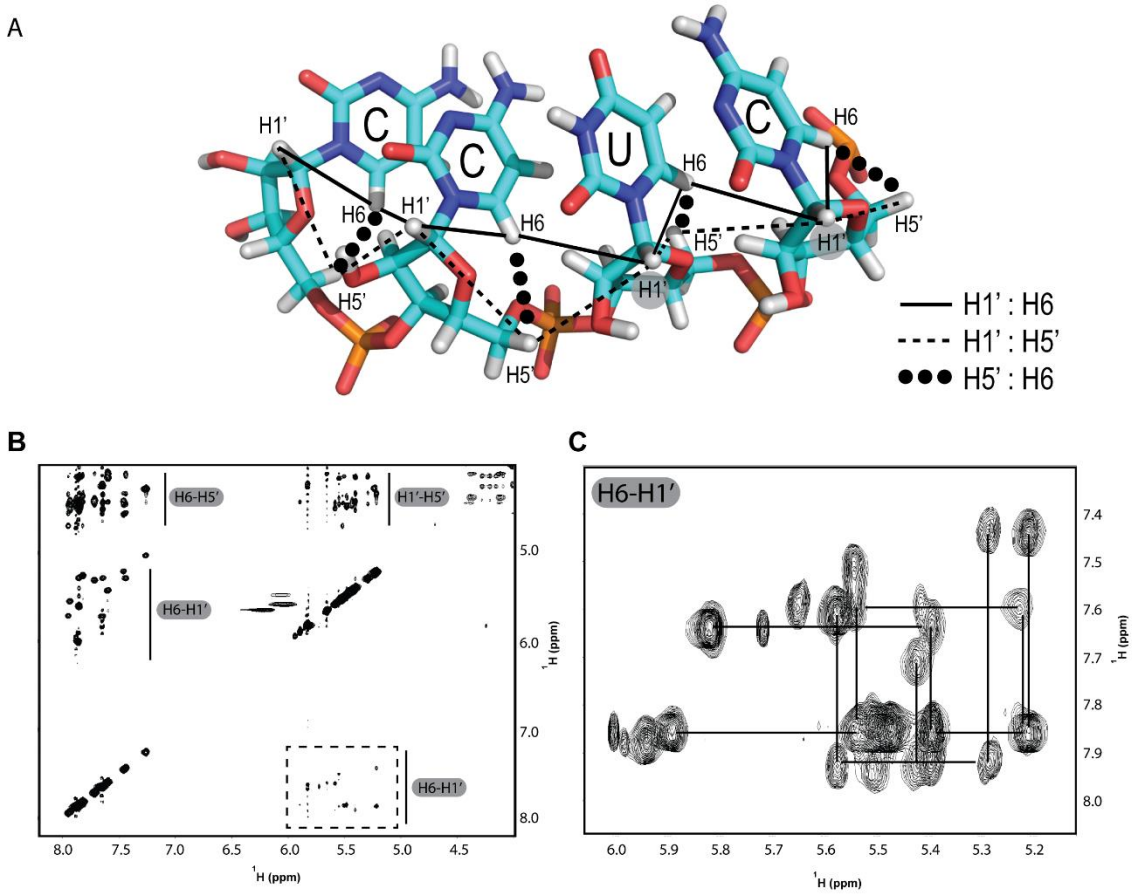

Figure 4.16. Three-dimensional ^{1}H-^{1}H-^{13}C NOESY-HSQC experiment for peak assignments by sequential through-space walks. (A) Through-space NOE walk in a pyrimidine stretch of the IRE RNA. I highlight all the potential connectivities observed utilizing out site-specifically labeled nucleotides (B) Two-dimensional projection of a 3D NOESY-HSQC experiment showing the well-resolved crosspeaks from aromatic H6 to H1′, H6 to H5′, and H1′ to H5′. The first is used for performing a sequential walk along helical segments in the IRE RNA that allows for peak assignment. (C) Focus on the region within the dashed lines in (a). Notice the sequential walk performed between the crosspeaks and the lack of any major overlap.

Next, to finish the rapid resonance assignment of the IRE RNA, I confirmed H1′ and H6 connectivities via through-bond experiments. I performed a 3D out-back HCN experiment which follows the coherence pathway from H1′ → C1′ → N1(pyrimidines)

and H6 → C6 → N1(pyrimidines, Figure 4.17a). The experiment showed us clear correlation peaks that corresponded to H1′ to H6 through-bond transfer (Figure 4.17b).

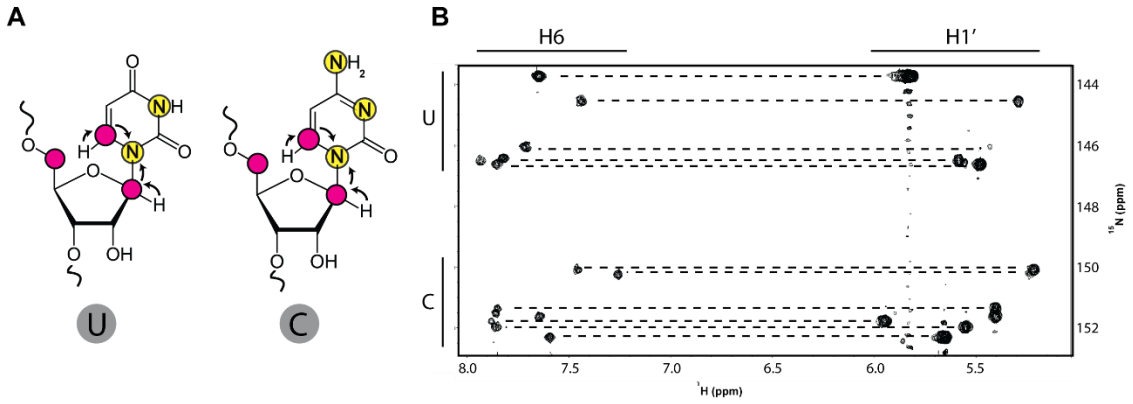

Figure 4.17. Three-dimensional out-back HCN experiment for peak assignments. (A) Scheme representing the magnetization transfer from protons in the ribose or base to the common N1 in pyrimidines used in our labeled IRE RNA. (B) Representative slice of a 3D HCN experiment, where I show the correlations between H6 and H1′ to allow for peak assignments. Notice the lack of overlap and the high signal-to-noise ratio.

Altogether, our battery of experiments allowed us to readily assign the minimum set of resonances needed for dynamics measurements of the IRE RNA. The simplification of the spectra due to the use of our site-specifically labeled nucleotides was instrumental in performing the assignments. I were able to assign every C1′-H1′ and C6-H6 moiety (Figure 4.18 and Table 4.1), both of which were later used for measurement of R_1 and R_2 decay constants. Additionally, as explained above, I assigned other resonances, which are given in Table 4.2.

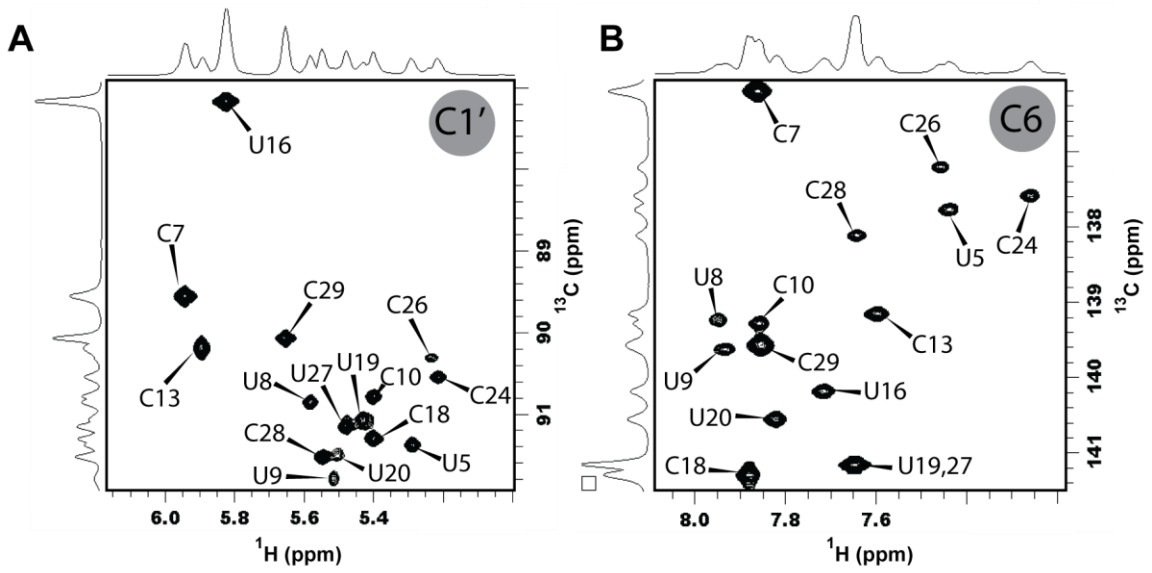

Figure 4.18. Initial ^{13}C-^{1}H assignments of the IRE RNA ribose and base moieties. (A) Assignments of C1′-H1′ resonances in a ^{13}C-^{1}H HSQC spectrum. (B) Assignments of C6-H6 resonances in a ^{13}C-^{1}H HSQC spectrum. Notice that all peaks are resolved.

Table 4.1. Partial resonance assignments of the IRE RNA, focused on residues utilized for dynamics measurements.[†]

Residue	*C1'*	*H1'*	*C6*	*H6*
U5	91.37	5.29	137.75	7.44
C7	89.54	5.94	136.19	7.06
U8	90.84	5.58	139.23	7.95
U9	91.78	5.52	139.62	7.94
C10	90.77	5.40	139.28	7.86
C13	90.19	5.89	139.15	7.60
U16	87.20	5.83	140.18	7.72
C18	91.29	5.40	141.31	7.88
U19	91.06	5.43	141.15	7.65
U20	91.50	5.50	140.54	7.82
C24	90.53	5.21	137.60	7.26
C26	90.30	5.23	137.21	7.46
U27	91.14	5.49	141.15	7.65

C28	91.51	5.55	138.09	7.64
C29	90.06	5.63	139.57	7.86

†All chemical shifts are in part-per-million (ppm)

Table 4.2 Partial resonance assignments of the IRE RNA, residues not involved in dynamics measurements.†

Residue	*N1*	*H1*	*Residue*	*C2*	*H2*	*Residue**	*N3*	*H3*
G1	147.59	12.61	A3	151.05	7.59	U5	158.72	11.60
G2	146.84	12.39	A11	149.35	6.72	U8	162.67	14.05
G4	148.55	13.59	A12	150.66	7.57	U9	158.20	11.73
G6	147.92	12.92	A14	151.17	7.84	U19	162.20	13.86
G17	144.05	10.94	A23	151.63	6.96	U20	162.37	13.08
G21	146.51	11.73				U27	162.67	14.07
G25	144.61	11.13						

†All chemical shifts are in part-per-million (ppm)
*U16 is not shown as it does not participate in base pairing; its imino H3 proton is in rapid solvent exchange, thus not observable in our experiments.

Next, to test the hypothesis that relaxation properties of our site-specifically labeled RNA are more favorable than those of uniformly-labeled RNAs, I conducted a series of relaxation experiments in our C- and U-labeled IRE RNA. Among the experiments I chose were: T_1 and $T_{1\rho}$ to measure ps – ns dynamics. Onward, a significant portion of the results obtained and their analysis were performed by Regan LeBlanc.

In particular, I chose the C6 position in the uracil and/or cytidine rings and the C1′ position in the ribose ring as our nuclear probes. Both C6 and C1′ have good chemical shift dispersion (7 – 8 ppm ^{1}H; 135 – 145 ppm ^{13}C, and 5 – 6 ppm ^{1}H; 88 – 96 ppm ^{13}C, respectively), have no $^{1}J_{CC}$-coupling in our constructs, and have been extensively used for

dynamics measurements in a number of systems.[164,181] Below, I highlight results from our findings.

Data from our T_1 experiments showed a good fit to a mono-exponential decay for the IRE RNA. The IRE RNA is only a 29-nucleotide RNA, and as such it was expected to behave favorably toward relaxation experiments. As stated above, I measured dynamics parameters of C1′-H1′ and C6-H6 moieties. The equation utilized to fit T1 data was:

$$M(t) = M_{eq} * (e^{-t/T_1});$$

Where, M(t) is the magnetization as a function of time, M_{eq} is the normalized magnetization at the start of the experiment, t is time, and T_1 is the decay constant. The parameter determined from each experiment for each residue was T1 which inverse magnitude provides the R_1 rate constant (in s^{-1}). Analogously, to obtain an R_2 constant from T1ρ experiments, I utilized the following equation:

$$R_{1\rho} = R_1 * cos^2\theta + R_2 * sin^2\,\theta; \text{ and}$$

$$\theta = \arctan(\omega/\Omega)$$

Where, θ is the tilt angle, ω is the spin-lock power level (3 KHz), and Ω is the resonance off-set. Data fits from T_1 and $T_{1\rho}$ experiments of this uniformly labeled RNA showed χ^2 values < $2x10^{-2}$, indicating robust fits to a mono-exponential decay (Figure 4.19a-b). Notably, some χ^2 values were as low as $7x10^{-4}$ for residues in the C6-H6 moiety. I then determined the R_1 and R_2 relaxation decay rates (in Hz) for every C and U residue in the

IRE RNA. R_1 and R_2 values can, for instance, be suggestive of conformational exchange in the moiety or residue in the micro- to millisecond time-scale. However, other relaxation mechanisms contributing to R_1 and R_2 relaxation rates cannot be discarded. Consistent with the available three-dimensional solution structure, the residues suggesting the largest conformational exchanges in the IRE RNA were C7, C13, U16, and C29 (Figure 4.19c-d).[87] C7 is a stem bulge residue, C13 is loosely base paired to G17 in the terminal loop, U16 is unconstrained in the terminal loop, and C29 is the closing base pair of the hairpin possibly undergoing end-fraying. I then proceeded to measure identical dynamic parameters in our C- and U-site specifically labeled IRE RNA for purposes of comparison.

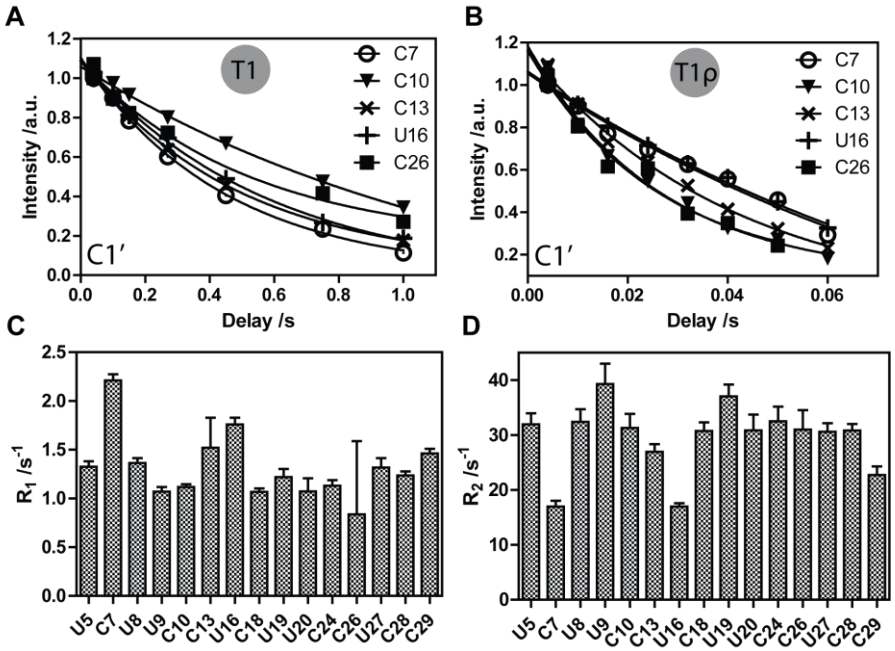

Figure 4.19. Dynamics data obtained from uniformly $^{13}C/^{15}N$ labeled IRE RNA. (A) Longitudinal relaxation (T_1) dynamics curve fits on five residues of the IRE RNA, focused on the C1′-H1′ spin system. (B) Rotating frame relaxation ($T_{1\rho}$) dynamics curve fits on the same five residues, focused on the C6-H6 spin system. (C) Decay rates determined for each residue of the IRE RNA from T_1 experiments. (D) Same as (c), but from $T_{1\rho}$ experiments. Error bars are shown as standard deviation.

Both labeling schemes, $^{13}C/^{15}N$ uniform and site-specific, yielded similar yet distinguishable results for R_1 and R_2 relaxation rates. It is important to note that the χ^2 values of the data fits from the specifically-labeled IRE RNA were frequently an order of magnitude smaller than those of the uniformly labeled construct, e.g. $2.4x10^{-3}$ and $1.3x10^{-2}$, respectively (Figure 4.20a). In order to compare our results, I plotted the R_2/R_1 ratio for each measured residue under uniform or specific labeling schemes (Figure 4.20b).

Notably, most residues retained the same dynamic parameters within error, except for at least three residues, U8, C13 and C26. The R_2 and R_1 fits of these residues in the uniformly labeled RNA noticeably deviated from a mono-exponential decay, displaying standard errors ~ 20 % of the determined decay rate. However, when utilizing our custom-made labels, I recovered a robust exponential decay fit, with χ^2 values from $2.7x10^{-4}$ to $2.3x10^{-3}$ and standard errors < 6 % for the residues analyzed. Another trend I can highlight is that uniform labeling seemed to consistently underestimate the R_2/R_1 ratio, with a few exceptions, i.e. C13, C24, and C26. Also, of note, some χ^2 values for the fits from the specifically labeled RNA were in the order of 10^{-5}.

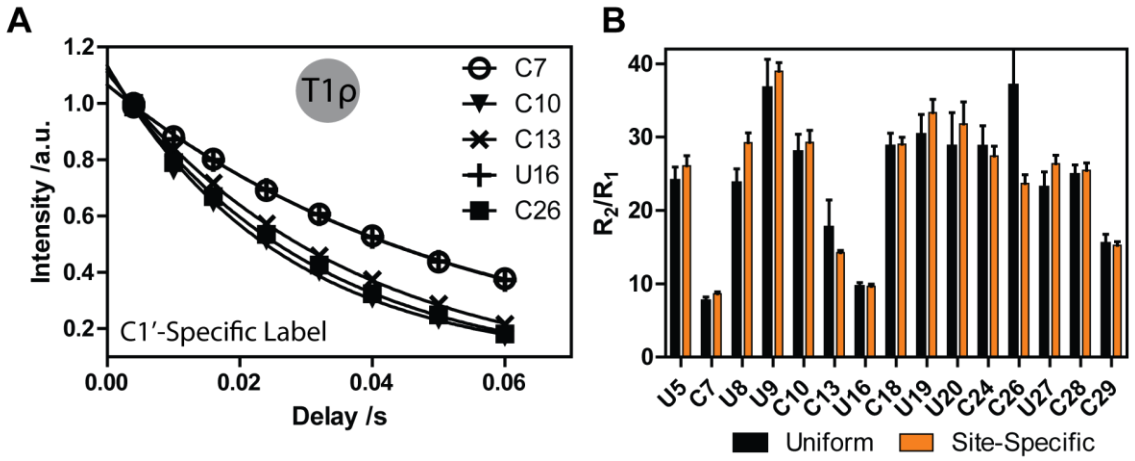

Figure 4.20. Site-specific labeling of the IRE RNA improves dynamics measurements of the IRE RNA. (A) Curve fits of $T_{1\rho}$ experiments on five residues of the IRE RNA. Notice the excellent fitting to a monoexponential decay. (B) Comparison of overall dynamics (R_2/R_1 ratio) of all U and C residues of the IRE RNA when the molecule was $^{13}C/^{15}N$ uniformly or site-specifically labeled. U8, C13 and C26 show sizeable differences in error. Most other residues remain unaffected. Errors bars are shown as standard deviation from three independent experiments. The error bar in C26 spans up to an R_2/R_1 value of 50 as is not shown in its entirety for illustrative purposes.

Altogether, our results have highlighted the usefulness of site-specific labeling of RNA. I showed that reduced spectral crowding along with segmental labeling aided in performing rapid peak assignment. In most cases, peak assignment represents the limiting step in RNA structure elucidation. Additionally, I established that the determination of dynamic parameters is more robust when utilizing our site-specific labels in contrast to $^{13}C/^{15}N$ uniformly labeled RNA.

Section 4.4: Discussion

Solution NMR still encounters problems related to spectral crowding, broad linewidths, unfavorable relaxation properties and diminished signal-to-noise ratios. To date, several strategies have been developed to address these issues, and these exploit

$^{13}C/^{15}N/^{2}H$ site-specific labeling of the RNA of interest. Five major approaches have been described to produce nucleotides and their subsequent incorporation into RNAs. (i) chemical synthesis of NTPs, (ii) *De novo* biosynthesis, (iii) Biomass production of NMPs, (iv) site-specific biomass production of NMPs, and (v) chemical enzymatic synthesis of nucleotides, followed by *in vitro* RNA transcription.[116] Each of these have their own advantages and downsides. In our work, I elaborated on (v), as it presents an outstanding combination of yields, labeling versatility and experimental ease.

Here I have showed the straightforward production of two pyrimidine nucleotides that were used in *in vitro* transcriptions of the IRE RNA (29 nt). First, in collaboration with Dr. Cristoph Kreutz, I were able to synthesize uracil with placement of isotopic labels anywhere I desire.[165] Then, the chemo-enzymatic synthesis of UTP consisted of a two-step one-pot reaction of <12 hours, achieving yields of >80 %. The synthesis of CTP directly from UTP was a one-step 5-hour reaction, with yields of >90 %. This allowed for the production of gram quantities of nucleotides with ease utilizing relatively inexpensive substrates. Yields from other methods (see above), ranged from 10 % to 75 %.[158,165,167] Since the necessary substrates and enzymes are now available by our lab,[100] I claim that the chemo-enzymatic protocols presented herein may be carried out without difficulties and with minimal hands-on work by any RNA/protein biochemistry laboratory.

I utilized 1′,5′-$^{13}C_2$-D-ribose as the sugar moiety in our enzymatic condensation reactions. This labeling pattern provides the best chemical shift dispersion of the ribose ring with no coupling between the two ^{13}C sites. Additionally, the C1′ position and its proton have also been used previously as dynamics probes,[164,182] especially in samples where the C5 position of pyrimidines is not labeled, i.e. 6-^{13}C-uracil (see above). As an

added benefit, the C5′ atom is an excellent probe for tailored methylene-optimized TROSY-based experiments, which I briefly used herein (Figure 4.15d). This experiment, which exploited the CH_2 group of the C5′ moiety, showed that our specific labels increased the signal-to-noise ratio by a factor of two. Additionally, as seen in Figure 4.16a, the assignment of the C5′, H5′ and H5′ is now more accessible. Previously, 2D total correlation experiments relying on uniformly labeled ribose rings and long transfer sequences were used to, at best, ambiguously assign C5′, H5′, and H5″.[126,180,183] Of note, the ribose molecule used herein is available commercially (Omicron biochemicals), as are several other labeling combinations of ribose, however at higher expense. Currently, I are exploring the possibility of chemically synthesizing ribose, incorporating ^{13}C and/or ^{2}H isotopes at specific locations.

Our site-specifically labeled nucleotides were shown to improve the relaxation properties of our medium-sized RNA. Various residues in the IRE RNA showed larger errors in their relaxation rates as a uniformly labeled molecule when compared to a site-specifically labeled sample. Incorporation of our site-specifically labeled nucleotides noticeably reduced the errors in longitudinal relaxation parameters, as shown in the mono-exponential decay fits of the experimental data for U8, C13, and C26. Strong scalar couplings, present in uniformly labeled RNA, introduce undesired contributions to NMR relaxation experiments, and thus can lead to erroneous data analysis and interpretation.[128,154] Given our results with a 29-nucleotide RNA, I think that RNAs larger than 30 nucleotides would greatly benefit from the use of $^{13}C/^{15}N$ site-specifically labeled nucleotides, and that the chemo-enzymatic synthesis of such nucleotides is a robust method for their production.

As an added benefit, our $^{13}C/^{15}N$ site-specifically labeled nucleotides also simplified spectral crowding, resolved ^{13}C-^{13}C scalar couplings and recovered some sensitivity challenges. Regardless of the RNA size, spectral crowding, especially near the C1′ and C5 region is problematic for peak assignments, dynamics measurements or any other type of spectral analysis. As such, I carefully picked the two building blocks (uracil and ribose) to synthesize versatile labels that contained isolated two-spin systems. Additionally, removing scalar couplings avoided the use of constant-time decoupling pulses. These pulses entail delays, which lead to signal loss, which is more dramatic with RNAs >30 nucleotides due to their longer correlation time.[128,180] Moreover, constant-time experiments do achieve effective decoupling, however at the expense of spectral resolution.[184–187] Other methods, such as broadband decoupling have the intrinsic disadvantage of precluding the observation of some decoupled nuclei, i.e. C2′.[180,188] The synergism of the two aforementioned improvements –lack of constant-time and decoupling pulses–, resulted in increased signal-to-noise ratios and resolution of the spectral data. Two of the major contributors to our improvements are: (i) the lack of direct one-bond scalar couplings, and (ii) a reduced number of dipolar couplings.

The full potential of the site-specifically labeled RNAs shown here has yet to be entirely explored. Here, I presented a battery of two- and three-dimensional experiments to assign peak resonances, analyze the structure, and dynamics of our system. However, there are several pulse programs that can be tailored to exploit the isolated two-spin systems presented herein. For instance, the C5′ moiety has been shown to be an excellent probe for CH_2-optimized TROSY.[178] Moreover, due to the spatial proximity of C5′ moieties in continuous nucleotides, there is potential to utilize TROSY-NOESY

experiments to obtain a distance-dependent ladder along the RNA backbone. This would in turn complement more traditional NOESY walks connecting C1′/C8/C6 moieties along the RNA which are heavily dependent on ribose pucker and syn/anti base orientation. In our work, I presented some preliminary data of the TROSY enhancement effect on the C5′ moiety. Current work in our laboratory is ongoing to further optimize the pulse program and incorporate other modules such as NOE and CPMG.

Further alterations can be made to our labeling schemes in order to increase their versatility and usefulness. Since our chemo-enzymatic method of synthesis is independent of the substrate labeling pattern, any combination of $^{13}C/^{15}N/^{2}H$ isotopes may be used. For instance, I have successfully transcribed RNAs containing unlabeled ribose rings and uniformly labeled uracil rings. The limitation to the labeling patterns of our pyrimidine nucleotides is, at this point, the ribose ring. Its chemical synthesis has proven cumbersome, yet improvements have been made, and recently more labeling combinations have been made commercially available. For instance, if placed strategically, ^{2}H may greatly enhance the relaxation properties of certain spin systems. Specifically, it has been shown that the CSA of the C5-H5 spin system is highly detrimental to dynamics measurements, especially for larger RNAs.[128,189,190]

Altogether, Chapters 3 and 4 have presented the groundwork for the future widespread use of $^{13}C/^{15}N$ site-specifically labeled nucleotides in NMR studies of RNA. The advantages of using custom-made nucleotides vastly overcome the cost and labor to synthesize them. Here, I have shown the efficacy of our nucleotides for structural and dynamic analyses of the IRE RNA. Notably, the study of RNA by NMR spectroscopy has been consistently picking up pace, especially in the last decade. Interestingly, the use of

dynamics to address biological questions has become of major interest to RNA biophysicists and biochemists.[191,192] Therefore, I strongly believe that technology development to facilitate studies will contribute to the continuing development of the field.

In the following chapters I return to addressing our overarching biological question of doxorubicin as a disruptor of the IRE RNA/IRP complex disruptor. Chapter 5 focuses on the biophysical characterization of the RNA/doxorubicin interaction, namely utilizing NMR spectroscopy. Chapter 6 focuses on the biophysical characterization of the RNA/protein interaction by biochemical methods. Finally, Chapter 7 addresses the potential of doxorubicin in disrupting the RNA/protein complex.

Chapter 5: Doxorubicin, a Chemotherapeutic Drug, as an Intercalator of the IRE RNA

Section 5.1: Introduction: Repurposing an Old Drug

The exogenous manipulation of cellular iron homeostasis by increasing the rate of ferritin synthesis may lead to better treatments, however few examples of such treatments exist.[83] Although most small-molecule/RNA interactions are targeted toward the inhibition of protein synthesis,[55,84,85] one example of downstream up-regulation was demonstrated by yohimbine. A stimulant and aphrodisiac, yohimbine, had previously been used in large excess to specifically disrupt the IRE/IRP complex and cause a subsequent increase in translation of the downstream message.[75] Yohimbine achieved a modest, yet significant, 8 % disruption of the complex *in vitro* while at a thousand-fold excess, presumably by binding to an internal bulge of the RNA, precluding specific RNA-protein contacts. Subsequent assays showed an increase of nearly 40 % in translation products, which could not be entirely reconciled with *in vitro* results.

Likewise, the use of doxorubicin to promote RNA-protein dissociation could potentially allow for downstream up-regulation of ferritin. I hypothesize that (i) doxorubicin intercalates specifically at two G•U wobble base pairs in the H-ferritin IRE RNA (Figure 2.1c) and that (ii) it causes partial RNA melting. In the following chapter I will address the concomitant disruption of the IRE/IRP complex by doxorubicin. In this chapter, I use fluorescence spectroscopy, multidimensional nuclear magnetic resonance, and electrophoretic mobility shift assays to study how doxorubicin interacts with H-

ferritin IRE RNA. All three approaches converge on the observation that doxorubicin intercalated in the IRE RNA with low micromolar affinity.

Section 5.2: Methods

5.2.1. RNA preparation:

Iron Responsive Element RNA (5′GGAGUGCUUCAACAGUGCUUGGACGCUCC) and its double mutant G22A,G25A (5′GGAGUGCUUCAACAGUGCUUGAACACUCC) were synthesized *in vitro* from synthetic DNA templates (Integrated DNA Technologies Inc.). The transcriptions were carried out in transcription buffer [40 mM Tris-HCl (pH 8.0), 1 mM spermidine, 0.01 % Triton X-100, 10 mM DTT, 80 mg/mL PEG (8000 MW)], supplemented with 2.0 U/mL thermostable inorganic pyrophosphatase (New England Biolabs, Inc.), 0.3 μM each DNA template, 10 mM $MgCl_2$, 10 mM total NTP (2.5 mM each NTP), and 0.5 mg/mL T7 RNA polymerase (expressed in *E. coli* BL21(DE3) and purified on pre-packed Ni-NTA beads in column mode as previously described).[193] The T7 promoter sequence used was 5′CTA ATA CGA CTC ACT ATA G. The template strands of wild-type and double-mutant (G22A,G25A) IRE RNA were 5′GGAGCGTCCAAGCACTGTTGAAGCACTC CTATAGTGAGTCGTATTAG and 5′GGAGTGTTCAAGCACTGTTGAAGCACTC CTATAGTGAGTCGTATTAG, respectively. Two terminal 2'-O-methyl modifications in the template strands were introduced to substantially reduce transcript heterogeneity.[194,195] The transcription conditions were optimized by a sparse-matrix approach. The RNA was purified using denaturing 13 % polyacrylamide gels, electroeluted, extensively dialyzed and diluted into 10 mM Na_3PO_4 or Tris-HCl pH 6.5, 10 mM NaCl, 0.2 mM EDTA. NMR samples were

prepared in phosphate buffers, whereas all other biochemical samples were prepared in Tris-HCl buffers. RNA transcripts containing ^{13}C and ^{15}N stable isotopes (Isotec/Sigma-Aldrich, Omicron) were transcribed under identical conditions, with the exception of NTPs, reduced to 5 mM total (1.25 mM each). Prior to any use, NMR or biochemical, the RNA was heated to 90 °C for two minutes and snapped cooled on ice for 10 minutes.

5.2.2. Fluorescence quenching of doxorubicin

I performed fluorescence quenching assays of doxorubicin to determine K_D values for the interaction of doxorubicin with IRE RNA. RNA-drug fluorescence quenching experiments were conducted on a spectrofluorimeter equipped with a precise temperature control unit. Experiments were conducted at 25 °C, with excitation wavelength of 480 nm, emission scanning wavelengths from 500 to 700 nm, and slit widths of 10 nm for both excitation and emission. The titrations of RNA into 7 µM doxorubicin were carried out in 10 mM Tris-HCl pH 6.5, 10 mM NaCl, 0.2 mM EDTA. These are the minimal buffer requirements for correct folding of the RNA. The data on the y-axis were plotted as fractional saturation. The data were fit to a Langmuir binding isotherm to determine the binding affinity and stoichiometry. All experiments were done in triplicates. All data were analyzed and plotted with GraphPad Prism 5.

5.2.3. Relative electrophoretic mobility shift assays

The interaction of the IRE RNA and doxorubicin were monitored with relative electrophoretic mobility shift assays. Prior to any assay, the IRE RNA was re-folded as described above. RNA-drug assays were incubated in 10 mM Tris-HCl pH 6.5, 10 mM NaCl, 0.2 mM EDTA for 30 min at room temperature. The RNA-drug complexes were then resolved in 15 % (19:1) acrylamide/bisacrylamide nondenaturing gels. The RNA

concentration was kept constant at 0.5 μM and the doxorubicin concentration varied from 0 to 100 μM. Likewise, RNA-protein assays were incubated in 24 mM HEPES-KOH pH 7.2, 60 mM KCl, 0.2 mM EDTA, 2 % β-mercaptoethanol, 5 % glycerol for 30 min at room temperature. The RNA concentration was kept constant at 0.2 μM and the protein concentration varied from 0 to 3 μM. Free and bound RNA was resolved in 6 % (19:1) acrylamide/bisacrylamide nondenaturing gels. Gels were run at 4 °C at 100 V. Free and bound RNA were visualized by staining with ethidium bromide. RNA-IRP-small molecule assays were carried out similarly, varying the drug concentration from 0 to 100 μM, keeping IRP-1 constant at 1.1 μM and visualizing the RNA. All gel images were quantified using GeneTools, and plotted with GraphPad Prism 5.

5.2.4. Nuclear Magnetic Resonance

The interaction of doxorubicin and IRE RNA was monitored with NMR spectra of the IRE RNA. The NMR samples contained 0.25 mM DSS for ^{1}H chemical shift referencing. IRE RNA was kept at a concentration of 0.1 – 0.2 mM, due to the poor solubility of doxorubicin in phosphate buffers. One-dimensional proton, two-dimensional homonuclear nuclear Overhauser, two-dimensional constant- and non-constant time ^{13}C and ^{15}N heteronuclear single quantum correlation (HSQC) spectra were collected at 25 °C on a 600 MHz Bruker Avance III spectrometer equipped with a HCN triple resonance cryoprobe. Standard protocols were used for the assignment of proton, carbon and nitrogen resonances. Three to four concentrations of drug were titrated into the RNA. All NMR data were processed using TopSpin 3.2.

Section 5.3: Results

5.3.1. IRE RNA and doxorubicin have low micromolar affinity

In order to test our hypothesis that doxorubicin specifically interacts with two G•U wobble sites in the IRE RNA, I performed a thermodynamic characterization of the interaction between the two molecules. The structure and ^{1}H NMR spectrum of doxorubicin is shown in Figure 5.1. As previously described, the natural fluorescence of doxorubicin was exploited to determine its apparent dissociation constant (K_D) with the IRE RNA.[196] Because doxorubicin undergoes fluorescence quenching upon interacting with nucleic acids, I were able to use fluorescence emission spectroscopy to monitor binding as a function of increasing RNA concentration with fixed drug concentration at 7 μM drug. A representative emission spectrum titration experiment is shown in Figure 5.2a. The fractional saturation was then plotted against the RNA concentration and the data were fit to a Langmuir binding isotherm to determine the apparent K_D of the interaction (Figure 5.2b). Note that these K_D's do not provide any conclusive information on the type of interaction occurring between the RNA and doxorubicin. The K_D's of doxorubicin with wild-type and G22A,G25A RNA were 730 ± 20 nM and 1300 ± 50 nM, respectively. The values of the Gibbs free energy of binding of doxorubicin to wild-type and mutant IRE RNA corresponding to the observed K_D values were calculated to be -4.3 ± 0.1 kcal/mol and -3.9 ± 0.2 kcal/mol, respectively. Our results showed that doxorubicin had a modest preferential binding to the IRE RNA construct containing G•U wobbles, a result that was consistent with previous findings using a similar IRE RNA construct.[61] Our results did not indicate specificity of doxorubicin toward the IRE RNA, but the data suggests that the interaction with the G•U-containing IRE RNA is marginally

favored. Similarly, the high nanomolar binding affinity of doxorubicin is expected, as its structure does not provide moieties to mediate several hydrogen-bonding interactions, salt-bridges or even shape-complementarity to either nucleobases or ribose rings.

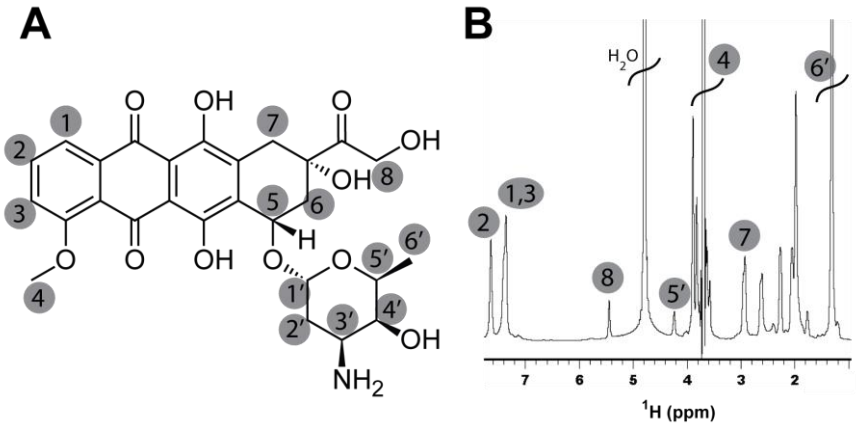

Figure 5.1. Doxorubicin, the DNA-intercalator used in our studies. (A) Structure of the anthracycline, the shaded numbers represent the non-exchangeable protons observable by NMR spectroscopy. (B) One dimensional proton spectrum of doxorubicin in water. The numbers correspond to the numbering scheme used in (a).

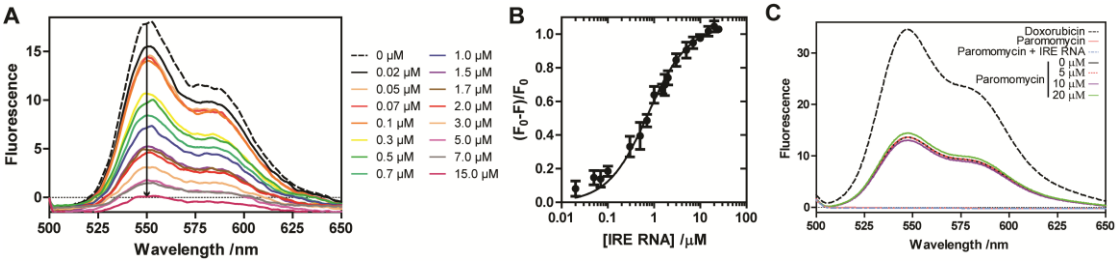

Figure 5.2. Doxorubicin has low micromolar-affinity interactions with the IRE RNA. (a) Representative fluorescence quenching profile of 7 μM doxorubicin's emission from 500 to 650 nm as increasing amounts of IRE RNA (0 to 25 μM) are titrated into the solution. (b) The emission intensity at 550 nm for every titration point was extracted and plotted against its corresponding IRE RNA concentration. The data were fitted to a Langmuir binding isotherm. Error bars represent standard deviation from three independent experiments. (c) Competition assay of paromomycin against doxorubicin. This order-of-addition experiment shows that increasing concentrations of paromomycin do not recover fluorescence, thus doxorubicin is not displaced by paromomycin from the IRE RNA.

Affinity measurements were also conducted with a close analog of doxorubicin, daunorubicin. The only difference between these two molecules is the substitution of an exocyclic α-hydroxyl by a methyl group. I hypothesized that the absence of the hydroxyl group weakens its binding affinity to the IRE RNA. The fluorescent properties of daunorubicin are identical to those of doxorubicin, hence I performed fluorescence quenching experiments to test our hypothesis. I determined daunorubicin's binding affinity to the wild-type IRE RNA to be 1600 ± 50 nM. These results showed that the absence of a single hydroxyl group affected the binding of the drug/RNA complex. Further, this data supported our previous results that doxorubicin preferentially binds IRE RNA.

Additionally, I performed competition assays with known RNA major groove binding agents to test both the specificity and affinity of doxorubicin to the IRE RNA. I hypothesized that doxorubicin binding to the IRE RNA was stronger and more specific than other aminoglycosides such as paromomycin, kanamycin, and streptomycin. The small molecules used were paromomycin, streptomycin and kanamycin. A competition experiment was carried out probing a doxorubicin-bound IRE RNA with increasing concentrations of aminoglycosides. A recovery in fluorescence signal represents effective displacement of doxorubicin from the IRE RNA. As seen in Figure 5.2c, addition of paromomycin up to 100 molar equivalents of doxorubicin did not recover any fluorescence, hence this small molecule was not able to displace doxorubicin. The other two molecules, streptomycin and kanamycin showed similar results, but were able to recover ~20 % of doxorubicin fluorescence at 100 and 1000 molar equivalents, respectively. These results indicate major groove binding aminoglycosides were not

specific for the binding site of doxorubicin and did not out-compete doxorubicin binding to the IRE RNA.

Having established interaction between the drug and IRE RNA by fluorescence experiments, I next investigated whether drug binding caused any major global conformational changes in the RNA. Interestingly, native gel electrophoresis did not show any significant migration changes even at doxorubicin concentrations in 1000-fold molar excess of the RNA; the R_f differences were <0.01. Notably, at concentrations ≥100 μM, doxorubicin is thought to dimerize, and such dimerization may impair interactions with the IRE RNA.[197] Doxorubicin's solubility is also poor ≥100 μM.

5.3.2. Doxorubicin interacts at G•U wobble base pairs flanked by G-C base pairs

To address our hypothesis of G•U wobble disruption and intercalation, I performed several nuclear magnetic resonance experiments aimed at dissecting the atomic and nucleotide-level interactions of doxorubicin with the IRE RNA. As observed in one-dimensional titration experiments, addition of the doxorubicin causes the disappearance, perhaps by solvent-exchange, of seven imino proton resonances (Figure 5.3a). The seven positions involved were G4, U5, G6, U9, G21, G22, and G25. The signal disappearance of G1-H1 can be attributed to end-fraying of the RNA, or perhaps due to non-specific electrostatic interactions with doxorubicin. The remaining six imino protons corresponded to both G•U wobble and their flanking G-C base pairs.

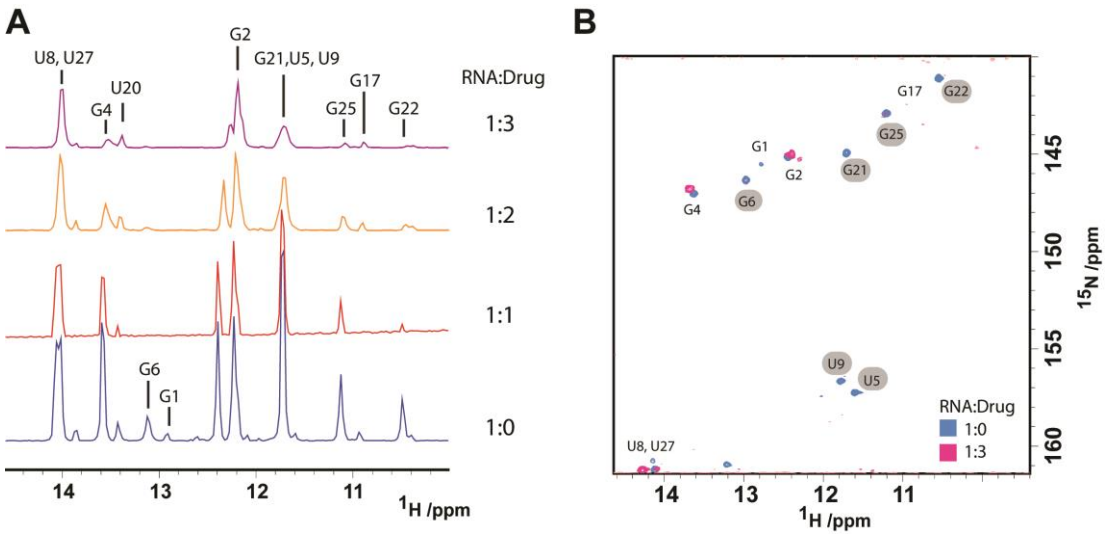

Figure 5.3. Doxorubicin disrupts four base-pair interactions in the IRE RNA. Representative NMR titration of doxorubicin into the IRE RNA. The resonances were assigned and are shown. Six resonances in the imino region undergo signal attenuation with increasing drug concentrations, as evidenced by their decrease in intensity. (a) One-dimensional titration, shaded ovals show the peak assignments. (b) Two-dimensional ^{15}N-^{1}H HSQC focused in the imino base-pairing region, shaded residues represent those undergoing a decrease in intensity, notice that the G25 resonance does not completely disappear.

To further support our hypothesis, I carried out two-dimensional ^{15}N-^{1}H single-quantum correlation spectroscopy (HSQC) experiments that correlate hydrogen-bonding imino protons to their nitrogen atoms (Figure 5.3b). The results corroborated the findings of the one-dimensional titrations; namely, only the two G•U wobble base pairs and their flanking G-C base pairs were affected by drug binding. The resonances corresponding to the G•U wobble and the flanking G-C base pair protons (U5, G6, U9, G21, G22, and G25) disappeared from the spectrum, whereas most other resonances remained unchanged (Figure 5.3b). The flanking G-C base pairs appeared to be disrupted to a lesser

extent. Additionally, at higher doxorubicin concentrations, other resonances appeared affected, suggesting further helix unwinding.

In order to test the notion that doxorubicin intercalated between both G•U and G-C base pairs, I performed two-dimensional ^{1}H-^{1}H nuclear Overhauser spectroscopy (NOESY) experiments (Figure 5.4, 5.5 and 5.6). NOESY experiments display off-diagonal resonances corresponding to two nuclei that are in close proximity (ca. 5 Å). Additionally, the intensity of the off-diagonal resonance peaks have a strong dependence on the distance between the two neighboring nuclei. For example, the imino proton of G25 is < 5 Å above the imino proton of G4, thus giving rise to a strong off-diagonal correlation peak (Figure 5.4a). Therefore, intercalation of the drug within two base pairs may increase the base pair rise and thus decrease the intensity of the involved off-diagonal peaks. As expected, in the absence of drug, I observed off-diagonal peaks of different intensities in the imino proton region corresponding to U5-H3•G25-H1, U5-H3•G6-H1, U9-H3•G22-H1, and U8-H3•G21-H1 (Figure 5.4a); all peak pairs were within 4.5 Å in the NMR solution structure.[66] Interestingly, upon titration of doxorubicin, the NOESY experiments showed a gradual attenuation of off-diagonal peaks corresponding to flanking base-pairs, i.e. U5-H3•G6-H1, and U8-H3•G21-H1, upon reaching equimolar amounts of drug (Figure 5.4b-c). In agreement with our previous ^{1}H and ^{15}N NMR data (Figure 5.3), the off-diagonal peaks corresponding to G•U wobble imino protons, i.e. U5-H3•G25-H1 and U9-H3•G22-H1, also had a dose-dependent signal decrease (Figures 5.4 and 5.5a).

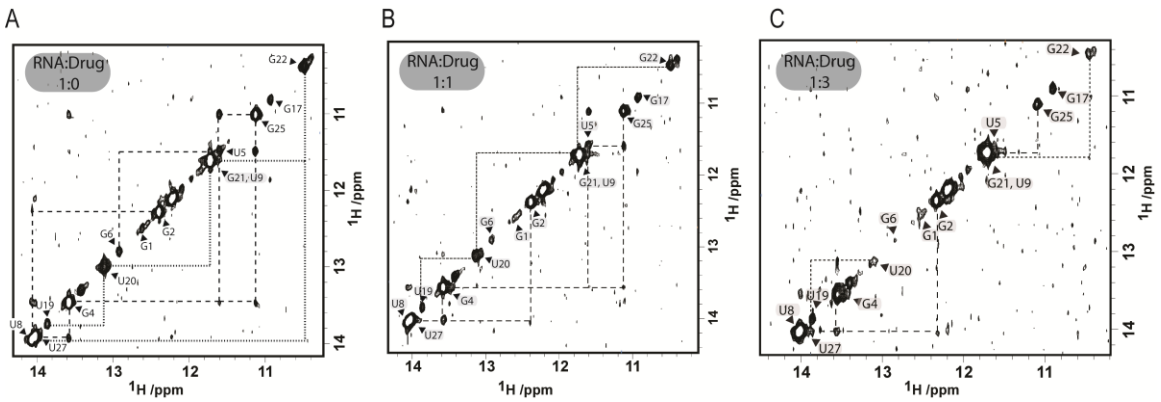

Figure 5.4. Doxorubicin disrupts the IRE RNA at G•U wobble base-pairs and suggests helix melting. Representative NMR titrations of doxorubicin into the IRE RNA are shown in these two-dimensional NOESY experiments showing the disappearance of imino-imino cross-peaks between G•U wobble and flanking G-C base-pairs. (a) Unbound RNA. (b) Complex of RNA:Doxorubicin in 1:1 molar ratio (c) Complex of RNA:Doxorubicin in 1:3 molar ratio. Solid lines: Upper stem, Dashed lines: Lower stem.

Because NOESY experiments show spatial connectivity between imino and amino protons of base pairs, I exploited this feature to titrate in doxorubicin. I found the off-diagonal resonance of G6-H1···C24-H4 was no longer observable (Figure 5.5b). The disappearance of the amino-imino resonance provided further evidence for the base-pair disruption of the G-C base pair that flanks the U9•G22 wobble. Upon further titrations of doxorubicin, the spectral signal-to-noise ratio increased, and other off-diagonal resonances disappeared from the spectrum, suggesting helical melting of the RNA. These results are consistent with previous data, where doxorubicin increased IRE RNA's T_m by 9.9 °C.[61] However, not all of the IRE RNA resonances disappeared. Specifically, the off diagonal peaks corresponding to G2-H1···C28-H4, and U27-H3···A3-H2 remained unaffected throughout the drug titrations (Figure 5.5b). Interestingly, the U20-H3···A11-H2 connectivity did show attenuation, however to a lesser extent than other residues. Furthermore, two-dimensional ^{15}N-^{1}H HSQC experiments that provide information on amino protons also demonstrate that major changes are not occurring in the RNA

structure, but that some guanine and cytosine amino residues disappear from the spectra. This line broadening effect may arise from solvent-exchange or fast exchange with doxorubicin. Two-dimensional data regarding carbon-proton correlations further provide support for no major conformational changes.

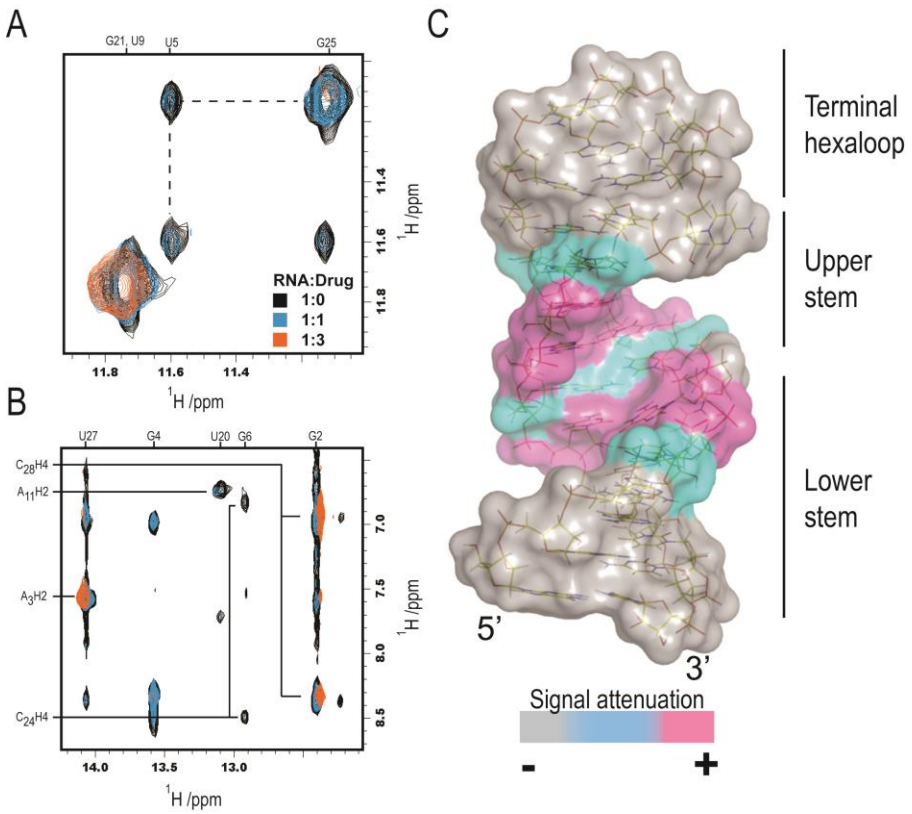

Figure 5.5. Doxorubicin disrupts the G•U wobble base pairs and their flanking G-C base pairs. (a) Expanded view of two-dimensional NOESY experiment of the U5•G25 base pair and their off-diagonal peak. Note the disappearance of both the imino signals and their corresponding cross-peak, likely represents the disruption of such base pair. (b) Two-dimensional NOESY experiment focused on the imino-aromatic proton region. The contacts of the G6 imino proton with the C24 amino (doublet at ~13 ppm) disappear upon addition of doxorubicin. Two connectivities not involved in the interaction are also highlighted, U27H3···A3H2 and G2H1···C28H4, and their intensities remain unaffected. Black: Unbound RNA, cyan: 1:1 RNA:drug complex, orange: 1:3 RNA:drug complex. (c) Base pairs that are affected by the interaction between the IRE RNA and doxorubicin. According to their signal attenuation, base pairs are represented from magenta (majorly attenuated) to gray (nearly unperturbed).

Next, I characterized doxorubicin's interactions with a double-mutant IRE RNA construct which replaced the two G•U wobble for two canonical A-U base pairs. As mentioned above, the G22A,G25A had a marginally larger dissociation constant with doxorubicin, 1300 ± 50 nM, than its wild-type counterpart, 730 ± 20 nM. Therefore, I hypothesized that the mutant IRE RNA base pair signal intensities and NOE contacts would be affected by doxorubicin to a lesser extent than with the wild type RNA.

The data obtained with the G22A,G25A double mutant IRE RNA showed similar, yet distinguishable, perturbation patterns upon doxorubicin titrations. Both one- and two-dimensional ^{1}H data showed a gradual disappearance of the two resonances produced by the newly introduced U5···A25 and U9···A22 base pairs. NOESY experiments showed drug intercalation as previously described for the wild-type RNA, however, the dose-dependent response was weaker. This was expected, as the apparent K_D of the double-mutant construct with doxorubicin was nearly two-fold larger in magnitude. It is important to note that these results do not let us claim an RNA-specific binding of doxorubicin to the H-ferritin IRE RNA, but rather its preference toward intercalation at G•U wobble base pair sites.

Additionally, since daunorubicin showed a similar binding affinity to the IRE RNA, 1.6 ± 0.1 μM, I hypothesized that it produced similar hydrogen-bonding and intercalation effects as doxorubicin. To test our hypothesis, I performed similar NMR experiments as described above for the characterization of doxorubicin's binding. Our results showed that daunorubicin also promoted base-pair opening at the same seven positions in the IRE RNA. Similarly, NOESY-type experiments showed decreased intensity of cross-peaks corresponding to G•U wobble base pairs and their flanking G-C

base pairs, albeit to a lesser degree than seen with doxorubicin. These results complemented the findings that daunorubicin has a decreased affinity toward the IRE RNA, yet its interactions are similar in nature: base pair disruption at G•U wobble base pairs.

Altogether, our results support our hypothesis that doxorubicin altered base pairing specifically at G•U and G-C base pairs in the H-ferritin IRE RNA, possibly by intercalation and subsequent helix melting at high doxorubicin:RNA molar ratios. Next, I aimed to test our hypothesis that doxorubicin, despite its weak binding affinity to the IRE RNA, is capable of disrupting the tight interaction of this RNA with is protein partner, IRP.

Section 5.4: Discussion

Doxorubicin is a strong chemotherapeutic agent widely used for a variety of carcinomas and its mechanism of action has been extensively characterized.[54–56] Its main interactions have been shown to be with genomic DNA, preventing cell division. However, non-specific interactions were suggested, and recently, this drug was shown to bind to the Iron Responsive Element (IRE) RNA *in vitro*.[61] The RNA/doxorubicin interaction, however, was not entirely characterized.

In this chapter, I characterized the interaction of doxorubicin with the consensus mammalian H-ferritin IRE RNA. The apparent dissociation constant of the IRE/doxorubicin complex was 730 nM, which was within an order of magnitude of previous work.[61] I showed, from our NMR results, that doxorubicin interacted at two G•U wobble and their flanking G-C base pairs, potentially affecting their hydrogen

bonding. Additionally, our data suggested partial RNA melting without a major conformational change in the IRE RNA structure. These results were not only consistent with previous reports by Canzoneri & Oyelere, but also with DNA-doxorubicin crystal structures (Figure 5.7).[53,54,198] In these crystal structures, doxorubicin intercalates between alternating G-C base pairs. The aromatic moiety of doxorubicin makes extensive pi-pi stacking interactions with the nucleotide bases. Additionally, its outer heterocyclic moiety makes hydrogen bond contacts with the phosphate backbone of the DNA, defining a type of anchoring that increases the affinity of the interaction. Likewise, from preliminary NMR results (not shown), I observed RNA/doxorubicin contacts at both aromatic and ribose moieties that may resemble the anchoring interactions found in DNA/doxorubicin crystal structures. Therefore, I put forward that a potential mode of interaction of doxorubicin is by major groove intercalation, accompanied by a few point contacts along the RNA's ribose and/or phosphate backbone. Current work in our laboratory is focused on obtaining a solution structure of the RNA/drug complex. It is important to note that no quantitative information could be obtained from our NMR experiments due to the concentration regimes of RNA and drug that were needed for reasonable experiment times, acceptable signal-to-noise ratios, and avoid doxorubicin precipitation. As mentioned above, doxorubicin is believed to self-dimerize at ≥ 20 μM, which likely partially hinders interaction with the RNA.

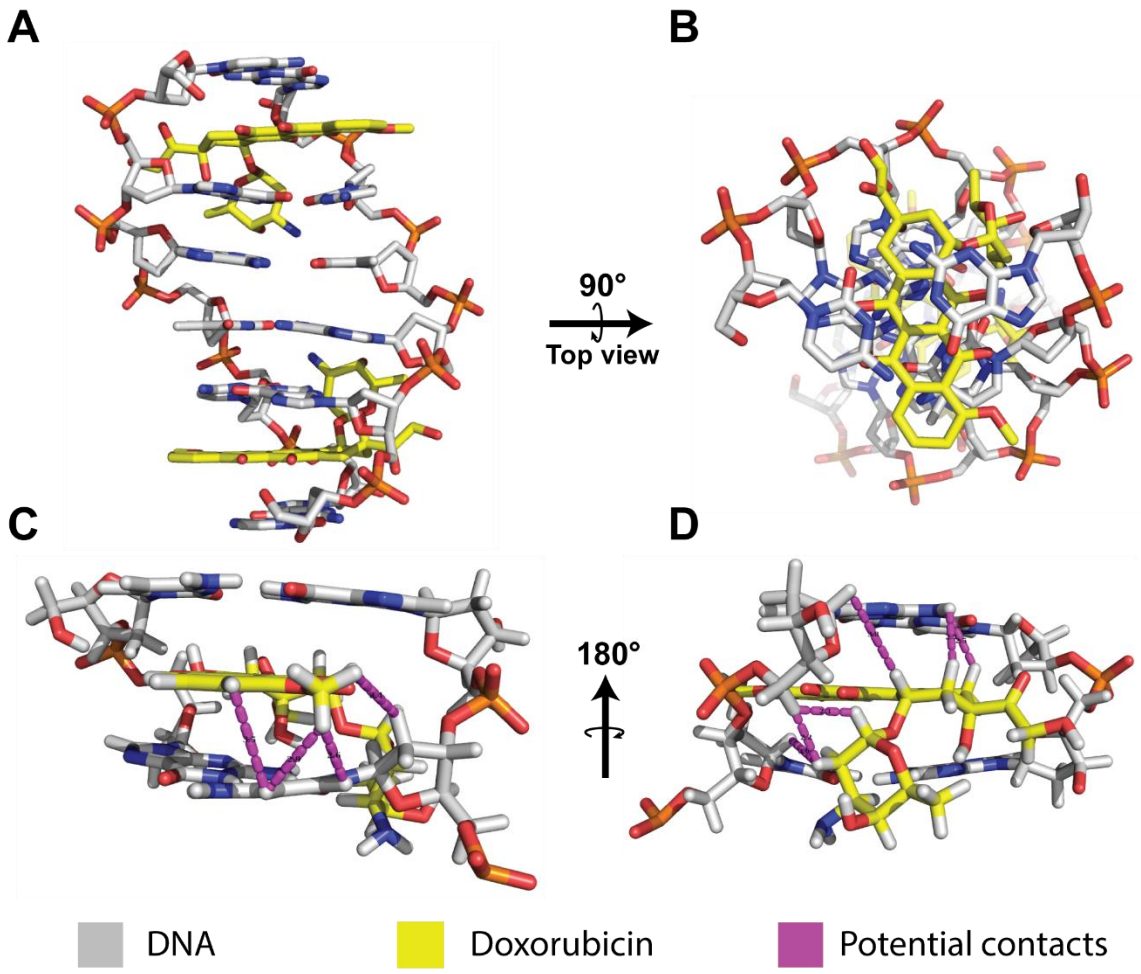

Figure 5.7. Crystal structure of doxorubicin in complex with DNA. (A) Overall view of the intercalation of doxorubicin in a DNA duplex. (B) Top view of the complex, notice the directionality of the intercalation and the aromatic stacking. (C) Close-up view of the binding site from the major groove, highlighting potential ^{1}H-^{1}H contacts below 5 Å. (D) Same as (c), but visualized from the minor groove.[54]

I recognize that doxorubicin does not provide exacerbated specificity or affinity. However, its binding affinity to the IRE RNA and the related free energy of binding are within those traditionally determined for other nucleic acid-intercalators and π- π interactions overall.[53,199–201] The removal of G•U wobbles in the mutant IRE RNA resulted in two-fold weaker binding affinities, showing the proclivity of doxorubicin

toward the wobble base pairs. One interesting approach to further develop doxorubicin, or any close derivative, would be to implement the work by Beal et al.[202] In their work, they modified an RNA intercalator to display peptide sequences that had affinity toward both RNA grooves. If the peptides chosen mimic the hIRP-1 aminoacids involved in RNA-binding, this may in turn increase both the affinity and specificity of the RNA/drug complex and further display enhanced competition against the IRP itself.

Of note, our studies were carried on a consensus RNA sequence for the 5′ UTR IRE of the human heavy-chain ferritin RNA. Other authors have performed extensive characterization of the complete sequence found in the human genome.[42,203,204] Our construct was chosen as it was representative of the wide variety of IREs, it consists of a portion of the human sequence, and it was amenable to NMR spectroscopy studies. From published reports, the human H-chain ferritin IRE RNA shares the following features with the construct used herein: (i) two distinguishable stems; (ii) 6-nt terminal loop of the sequence CAGUG(U/C); (iii) unpaired C-bulge residue five nucleotides below the hexaloop; and (iv) significant canonical secondary structure to maintain an A-form helix (Figure 2.1c). Further studies will focus in utilizing the human variant of the H-ferritin IRE RNA in assessing its binding to doxorubicin and hIRP-1.

Altogether, in Chapter 5, I have showed data that suggests doxorubicin is an intercalator of the IRE RNA. Additionally, the intercalation of doxorubicin produced a concomitant partial helix melting, leaving four base pairs stitching the RNA together. The binding affinity of the complex is 730 nM. The binding is weakened when utilizing either a mutant RNA or a close analog of doxorubicin. Our findings reconcile prior *in vitro*

data, and primes our studies for the future potential of doxorubicin as an RNA/protein disruptor.

Next, in Chapter 6, I characterize the IRE RNA/hIRP-1 interaction. I utilize various techniques, namely electrophoretic mobility shift assays and fluorescence spectroscopy to determine their apparent binding affinity. I present, to our knowledge, the first direct evidence of our specific RNA construct binding to the hIRP-1.

Chapter 6: Binding Studies of the IRE RNA / IRP Complex

Section 6.1: Introduction

Prior to evaluating the potential of doxorubicin as an RNA/protein complex disruptor, I aimed to characterize the complex biochemically. The IRE/IRP complex has been previously characterized by utilizing a combination of human, rabbit, and frog constructs.[65,75,86] However, this is the first time that hard evidence is presented on the binding of this particular human H-ferritin IRE RNA construct and the human Iron Regulatory Protein 1. Pardi et al. suggested having performed competition assays to estimate the binding affinity of the RNA/protein complex in the 20 – 40 pM range; however no direct evidence was presented to support these findings.[87] More recently, Goss et al. had characterized the binding of the IRE RNA/IRP complex, and determined its apparent binding affinity to be 14.2 ± 0.3 nM.[65] This binding affinity is well within the range of well-characterized RNA/protein interactions, which normally have a binding affinity in the low- to mid-nanomolar range.[205,206]

To our knowledge, this study represents the first direct evidence of our specific construct binding to the human Iron Regulatory Protein 1. Here, I sought to characterize the interaction, determining its binding affinity. With the K_D of the interaction at hand, I would be able to later assess the potential of doxorubicin as a *bona fide* disruptor of the complex.

The available high-resolution structural data on the IRE/IRP complex revealed a series of specific contacts that mediated the interaction, thus accounting for nanomolar complex binding.[86] Of note, the IRE RNA used by Walden et al. was that of frog, not the

human genome. Interestingly, hIRP-1 does not bind to the IRE RNA using traditional RNA binding motifs such as RNA-recognition motifs, zinc-fingers, or PUFs domains.[207] Instead, the IRE/IRP interaction may be classified separately due to the two-point interaction accompanied by partial protein engulfment. As seen in Figure 6.1a, the hIRP-1 adopts an extended conformation, an L-like shape to bind one IRE RNA molecule. Interestingly, if the complex is viewed from the top, one face of the RNA is entirely exposed to solvent (Figure 6.1b). More importantly, the minor groove of the IRE RNA makes most of the contacts with the IRP, thus leaving the major groove available for interactions with solvent, ions, or even small molecules (Figure 6.1c). The number of non-specific contacts, i.e. electrostatic contacts with the RNA's phosphate backbone, cover nearly 3000 $Å^2$, which contributes to the expected low nanomolar affinity.

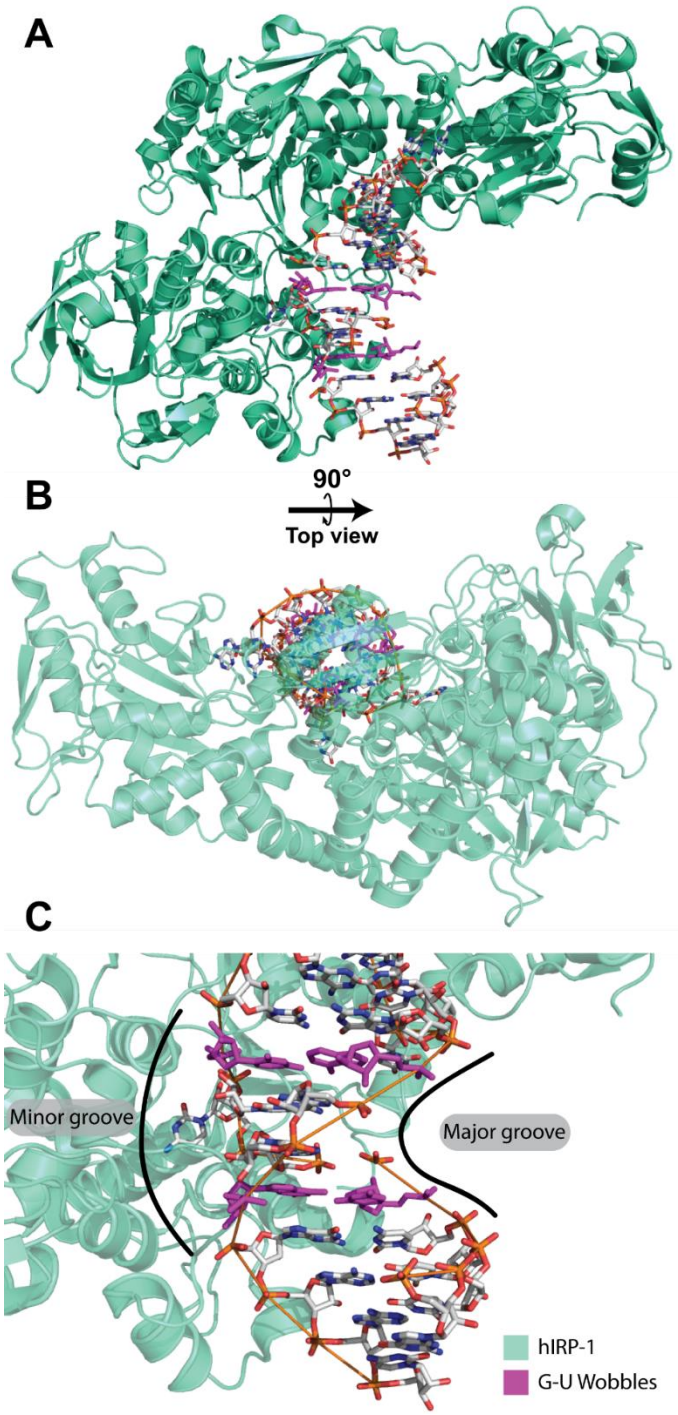

Figure 6.1. Crystal structure of the IRE RNA/hIRP-1 complex. (A) Overall view of the interaction. Note that the protein binds the RNA predominantly on one face. (B) Top view of the RNA/protein complex to show the solvent accessibility of nearly half of the RNA surface. (C) Close up view of the binding surfaces to show that most of the RNA/protein interactions are minor groove-mediated, whereas the major groove of the IRE RNA remains accessible to solvent.[86]

The specificity of binding is mainly due to buried nucleobases into aminoacid side chain cavities at two separate locations. Two terminal loop residues, A14 and G15 (using the numbering in Figure 5.1c), extend into a binding cavity between domains 2 and 3 of the IRP. Toward the center of the RNA, C7, buries into a pocket of domain 4 where it makes contacts with a number of aminoacid side chains. Specifically, C7 makes direct contacts with S681, P682, R713, R780, D781, and W782 (Figure 6.2). Another contributing factor to the specificity of the IRP for the IRE RNA is the ~30 Å separation between the C7 and G15 binding points. This distance is held in place by the upper stem's five base pairs, thus functioning as a molecular ruler. It is important to highlight that the G•U wobble base pairs do not participate in binding to the protein, yet, they are in close proximity to the residues involved in binding (Figure 6.2).

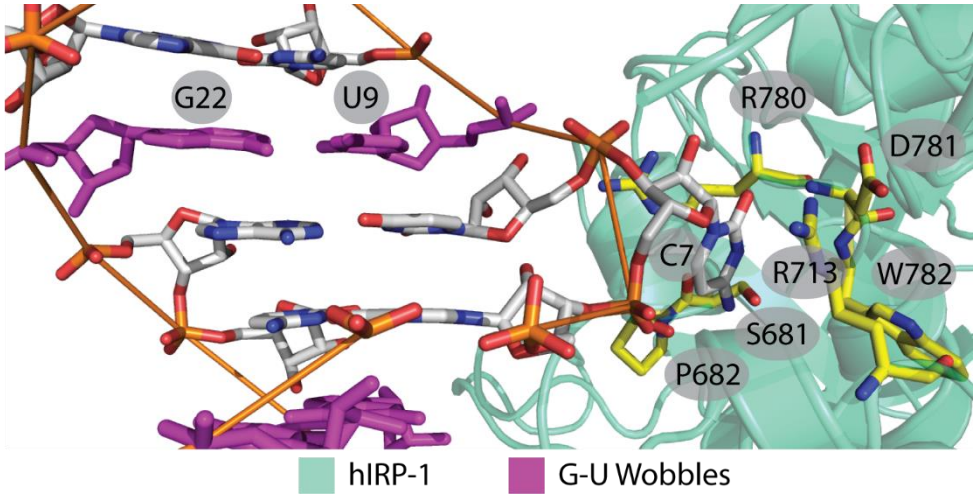

Figure 6.2. The specific interactions of the IRE RNA and hIRP-1. Crystal structure showing a number of specific contacts of the IRP with C7 of the IRE RNA. Also, highlighted in purple are the G•U wobbles in the RNA. Note the proximity of the wobbles to C7.[86]

In this chapter, I characterize the binding of our IRE RNA construct to the hIRP-1. I hypothesized that the apparent binding affinity of the partners is in the low nanomolar range given all the precedence on this system. I also hypothesized that our G22A,G25A mutant RNA construct presents no impairment when binding to the hIRP-1. Obtaining an estimate of the molecular stability of the RNA/protein complex will then allow us to assess the potential of doxorubicin to weaken such stability.

Section 6.2: Methods

6.2.1. RNA Preparation

Iron Responsive Element RNA (5′GGAGUGCUUCAACAGUGCUUGGACGCUCC) and its double mutant G22A,G25A (5′GGAGUGCUUCAACAGUGCUUGAACACUCC) were synthesized *in vitro* from synthetic DNA templates (Integrated DNA Technologies Inc.). The transcriptions were carried out at 40 mM Tris-HCl (pH 8.0), 1 mM spermidine, 0.01 % Triton X-100, 10 mM DTT, 80 mg/mL PEG (8000 MW), 2.0 U/mL thermostable inorganic pyrophosphatase (New England Biolabs, Inc.), 0.3 μM each DNA template, 10 mM $MgCl_2$, 10 mM total NTP (2.5 mM each NTP), and 0.5 mg/mL T7 RNA polymerase (expressed in E. coli BL21(DE3) and purified on pre-packed Ni-NTA beads in column mode as previously described).[193] The T7 promoter sequence was 5′CTA ATA CGA CTC ACT ATA G. The template strands of wild-type and double-mutant (G22A,G25A) IRE RNA were 5′GGAGCGTCCAAGCACTGTTGAAGCACTC CTATAGTGAGTCGTATTAG and 5′GGAGTGTTCAAGCACTGTTGAAGCACTC CTATAGTGAGTCGTATTAG, respectively. Two terminal 2'-O-methyl modifications

in the template strands were introduced to substantially reduce transcript heterogeneity.[194,195] The transcription conditions were optimized by a sparse-matrix approach. The RNA was purified using denaturing 13 % polyacrylamide gels, electroeluted, extensively dialyzed and diluted into 10 mM Tris-HCl pH 6.5, 10 mM NaCl, 0.2 mM EDTA. Prior to any use, the RNA was heated to 90 °C for two minutes and snapped cooled on ice for 10 minutes.

6.2.2. Iron regulatory protein expression and purification:

Histidine-tagged human cytoplasmic aconitase (hIRP1), 98.4 kDa, was overexpressed in *Escherichia coli* by the overproducing strain K12 pQE9-his-hIRF, which was kindly provided by Professor Matthias Hentze of the European Molecular Biology Laboratory in Heidelberg. The culture was grown, harvested, and lysed according to a locally modified version of a published protocol.[208] Purification of hIRP1 from the lysate was carried out using a HiTrap chelating resin (Pharmacia) charged with Ni^{2+}. The resin was washed with the following buffers: Buffer A) 25 mM Tris-HCl, pH 7.6, 150 mM potassium acetate, 1.5 mM $MgCl_2$, 5 % glycerol; Buffer B) Buffer A + 10 mM imidazole + 0.5 M NaCl to remove non-specifically bound proteins. After the addition of each buffer, the resin was washed until A_{280} had returned to background levels. The tagged protein was eluted with a gradient of 10 mM to 100 mM imidazole in Buffer A. Fractions were collected and analyzed by SDS-gel electrophoresis. Purity was estimated to be ~90 % by SDS-gel electrophoresis. Protein concentration was determined by measuring absorbance at 280 nm using a molar extinction coefficient of 84,700 $M^{-1}cm^{-1}$. Protein was stored at -70 °C until ready for use, at which time it was exchanged into the desired buffer for binding assays.

6.2.3. Relative electrophoretic mobility shift assays

The interaction of the IRE RNA and IRP were monitored with relative electrophoretic mobility shift assays. Prior to any assay, the IRE RNA was re-folded as described above. RNA-protein assays were incubated in 24 mM HEPES-KOH pH 7.2, 60 mM KCl, 0.2 mM EDTA, 2 % β-mercaptoethanol, 5 % glycerol for 30 min at room temperature. The RNA concentration was kept constant at 0.2 µM and the protein concentration varied from 0 to 3 µM. Free and bound RNA was resolved in 6 % (19:1) acrylamide/bisacrylamide nondenaturing gels. Gels were run at 4 °C at 100 V. Free and bound RNA were visualized by staining with ethidium bromide. All gel images were quantified using GeneTools, and plotted with GraphPad Prism 5.

6.2.4. Fluorescence quenching of hIRP-1

I performed quenching of intrinsic tryptophan fluorescence to determine apparent K_D values for the IRE RNA/IRP interaction. RNA/protein experiments were conducted on a JY Horiba Fluorolog-3 spectrofluorimeter equipped with a precise temperature control unit. Experiments were conducted at 25 °C and 12 °C, with an excitation wavelength of 280 nm, emission scanning wavelengths from 300 to 400 nm, and slit widths of 5 nm and 6 nm for excitation and emission, respectively. The titrations of IRE RNA into 150 nM hIRP-1 were carried out in a 24 mM HEPES-KOH pH 7.2, 60 mM KCl, 0.2 mM EDTA, 2 % β-mercaptoethanol buffer. The IRE RNA concentrations ranged from 1 nM to 900 nM. The fluorescence intensity at 335 nm was extracted and plotted against the RNA concentration titrated. Throughout the titrations, the IRP concentration was only decreased by < 2 %. The data were fit to a Langmuir binding

isotherm to determine the apparent binding affinity. All experiments were done at least in triplicates. All data were analyzed and plotted with GraphPad Prism 5.

Section 6.3: Results

6.3.1. The IRE RNA and IRP have an interaction in the low nanomolar range

The interaction between the heavy-chain ferritin IRE RNA and the Iron Regulatory Protein isoform 1 (IRP) has been extensively characterized,[86,97,209] with a very high-resolution crystal structure of the frog H-ferritin IRE RNA and rabbit IRP-1.[86] Similarly, using quenching of intrinsic tryptophan fluorescence upon RNA-binding to IRP, Theil and Goss showed that the human version of the RNA binds with low nanomolar affinity to IRP-1.[64,65]

In our work, I utilized a consensus mammalian H-ferritin IRE (Figure 5.1c) that differs from the human counterpart in two ways. First, our construct is truncated in the lower stem by three base pairs, with the addition of two G-C base pairs to promote complete helix formation to facilitate NMR studies.[87] Second, whereas the human counterpart features one uridine and one cytosine internal bulges. Ours has only one bulged cytosine (C7) in the hairpin stem. In the human sequence, these two bulged C and U residues are expected to make both specific and non-specific interactions with the IRP, but there is no high-resolution data available to confirm this. Other residues involved in specific IRP-binding are located in the hexaloop, such as G15, which is also present in our construct.

To our knowledge, this is the first time that this particular H-ferritin IRE RNA construct has been shown to be bound by the human IRP-1. I performed intrinsic tryptophan fluorescence quenching assays to determine the apparent dissociation constant of the IRE RNA/IRP complex (Figure 6a). According to the published crystal structures, one tryptophan residue, W590, undergoes a local structural rearrangement that may partly account for the fluorescence quenching phenomenon.[86,96] Nonetheless, I cannot discard a conglomerate effect of more than one tryptophan residue contributing toward this fluorescence quenching effect. Early reports by Goforth et al. had estimated this RNA-protein binding to occur in the pM range, whereas recent work by Khan et al. had reported a K_D of nearly 50 nM.[42,65] In our assays, due to low signal-to-noise ratios and inner-filter effects below 50 nM IRP, I were unable to determine a true dissociation constant of the IRE RNA/IRP complex. Therefore, I sought to determine an apparent K_D, which would only represent the molecular stability of the complex under the specific conditions and concentration regimes used in our assays. I determined the binding affinity of the complex to be 9.1 ± 0.4 nM (Figure 6b). Interestingly, the binding of the double-mutant G22A,G25A IRE RNA was determined to be slightly stronger to the IRP than its wild-type counterpart. The apparent binding affinity of G22A,G25A IRE RNA to the IRP was 6.2 ± 0.5 nM.

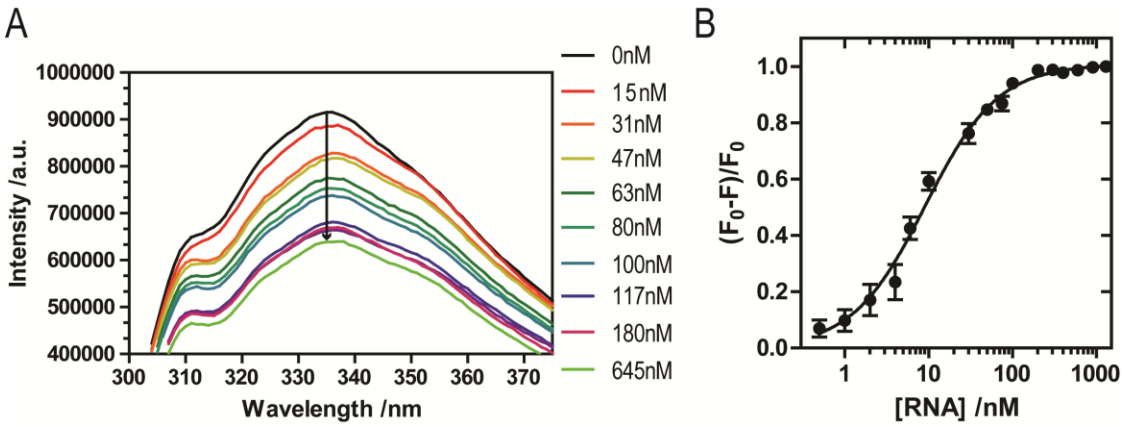

Figure 6.3. The IRE RNA-IRP interaction has a low nanomolar binding affinity. (a) Representative intrinsic fluorescence quenching profile of 150 nM hIRP-1 emission from 300 to 375 nm as increasing amounts of IRE RNA (0 to 1300 nM) are titrated into the solution. (b) The emission intensity at 335 nm for every titration point was extracted and plotted against its corresponding IRE RNA concentration. The data were fit to a Langmuir binding isotherm. Error bars represent standard deviation.

6.3.2. The IRE RNA and IRP binding stoichiometry

Interestingly, when assessing the IRE/IRP interaction by relative electrophoretic mobility shift assays, binding was observed only at high protein/RNA ratios. This behavior has been observed with other IRE RNA constructs, showing complete disappearance of free RNA at a 10:1 protein/RNA molar ratio.[65] Similarly, our gel shift assays showed the same apparent binding stoichiometry (Figure 7a). The counter-intuitive stoichiometry can be attributed to the dimerization of IRP at low micromolar concentrations, where the dimer loses its RNA-binding capability. At 0.15 μM IRP, nearly 30 % of the protein has been found as a dimer in solution.[210] In our experiments, coomassie brilliant blue staining for IRP showed two bands, corresponding to both monomers and dimers of the protein, whereas ethidium bromide staining only showed one band overlapping with the monomer IRP. Additionally, the faint/slightly diffuse

IRE/IRP band in the gel shift assays rather than a sharp/crisp band has been previously observed.[65]

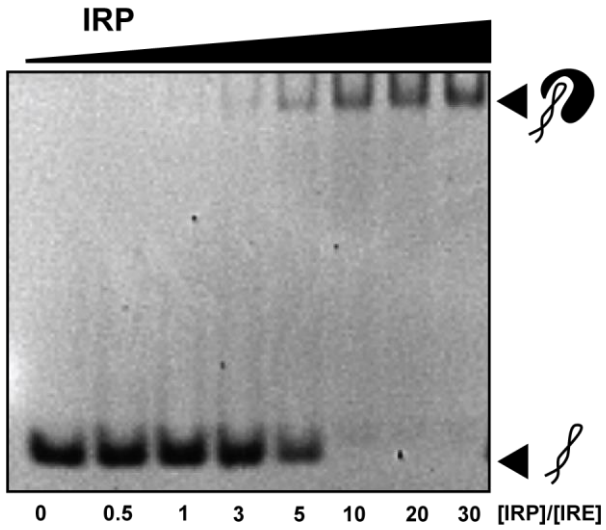

Figure 6.4. The IRE RNA/IRP binding stoichiometry seems suprisingly high. Representative mobility gel shift assay that shows binding of the IRE RNA to the hIRP-1 at high protein/RNA molar ratios.

Altogether, our results confirmed our hypothesis that the IRE/IRP complex has tight binding in the low nanomolar range. Our fluorescence quenching experiments showed a marked dose-dependent response to the IRE RNA concentration. Surprisingly, our gel shift assay results did not resemble our fluorescence assays, as the binding stoichiometry of the complex appeared to be nearly 10:1 IRP:RNA molar ratios.

Section 4: Discussion

The IRE RNA/hIRP-1 complex has been heavily characterized over the last two decades, hence it has become an excellent model system for our studies. Its binding

affinity had been previously estimated in the low nanomolar and even picomolar range. Here I showed, for our purposes, that the complex has an apparent binding affinity of 9.1 ± 0.4 nM. Interestingly, the G22A,G25A RNA mutant showed a stronger binding affinity, 6.2 ± 0.5 nM. This result is not entirely surprising as the exchange of G•U wobble for canonical A-U base pairs should contribute toward the stabilization of the helical structure. Consequently, a more stable and canonical upper stem would mean that the required 30 Å distance between G15 and C7 is maintained more rigorously, thus allowing for a more robust recognition of the IRE RNA by hIRP-1.

The interaction between the IRE and IRP is rather strong, however high-resolution structural data highlights some weaknesses of the complex. First, the mode of interaction of the protein with the RNA leaves significant solvent accessible surfaces (Figure 6.1b). Further inspection reveals that the major groove of the IRE RNA is almost entirely solvent exposed for one full helical turn (Figure 6.1c). Second, the stringent dependence on the upper stem's length in determining protein-binding leaves room for manipulating this interaction. Increasing the base pair rise beyond the canonical 2.8 Å may effectively elongate the upper stem to partially disturb IRP binding of the IRE RNA.

The unexpected gel shift assay results emphasized the strong dimer interaction between hIRP-1 at higher micromolar concentrations. The hIRP-1 has a dimerization constant of 7.7 ± 0.8 μM.[210] Given this strong dimerization, it was difficult to reconcile how a crystal structure of the RNA/protein complex was obtained,[86] since dimerization precludes RNA-binding. As well, the crystal structure of IRP as a cytosolic aconitase does not show dimers in the asymmetric unit.[96] Our future work will entail validating the dimerization of the protein by NMR, utilizing diffusion-ordered two-dimensional

spectroscopy.[211,212] This experiment would allow us to clearly distinguish the concentration regimes under which IRP behaves as a monomer or dimer. Furthermore, our future work will focus on characterizing the RNA/protein complex by solution NMR, observing either the protein or the IRE RNA. The latter would be achieved by implementing $^{13}C/^{15}N$ site-specifically labeled nucleotides and tailored pulse programs to exploit our labels (see Chapter 4).

Chapters 5 and 6 have focused on characterizing the binary interactions of the IRE RNA with either doxorubicin or the IRP; Chapter 7 will focus on the tripartite system. I showed that doxorubicin has a high nanomolar binding affinity for the IRE RNA, 730 nM; and that the IRP has a low nanomolar affinity to the RNA, 9.1 nM. From first principles, the ~100-fold differential in affinities would represent a difficulty in testing our hypothesis that doxorubicin does indeed weaken the RNA/protein complex. Nonetheless, given all the structural features of the RNA/protein complex and its inherent weaknesses detailed in this chapter, I present, in the next chapter, how doxorubicin has a mild disruptive effect on the IRE/IRP complex.

Chapter 7: Doxorubicin as a Blocker of the IRE RNA – IRP Complex

Section 7.1: Introduction

In the previous two chapters, I were able to characterize the interaction between the IRE RNA and doxorubicin and also with the IRP. The interaction with hIRP-1 is both very strong and specific for the IRE RNA. The interaction with doxorubicin is weaker and less specific. In our work, I determined the IRE RNA/IRP complex apparent dissociation constant to be 9.1 ± 0.4 nM; and that of RNA/doxorubicin to be 730 ± 20 nM. I strongly emphasize that the value determined for the IRE/IRP complex is likely not the true binding affinity, as it had been expected to be between 20 – 40 pM,[87] therefore further testing with higher sensitivity assays will need to be performed. Nonetheless, the magnitude of the binding affinity determined in our studies is a trustworthy measure of the stability of the complex under the conditions tested. Hence, our results will be presented as molecular stabilities, K_A, instead of dissociation constants.

As previously mentioned, the binding of the IRP to the IRE RNA presents several opportunities for its disruption. The solvent-accessible surface area is ~3700 $Å^2$, mostly displaying a full turn of the major groove, and nearly half a turn of the minor groove.[86] Therefore, I hypothesized that the extensive solvent exposure and groove accessibility of the IRE RNA while in complex with the IRP may allow for doxorubicin to intercalate into the IRE RNA, promoting complex disruption. Additionally, as seen in Figure 6.2, the proximity of the G•U wobble base pairs to the C7 bulge is also indicative of the potential for doxorubicin to disturb the RNA/protein complex. The intercalation of doxorubicin

into the IRE RNA, shown in Chapter 5, produced partial helix melting. This effect may in turn render the bulge C7, and maybe other contacts, off the stringent geometric requirement of the IRP to bind the IRE RNA. Thus, I further hypothesized that doxorubicin, as an RNA intercalator and promoter of partial helix melting, would also allow for RNA/protein complex weakening.

Other authors have shown the potential of small molecules as disruptors of RNA/protein interactions. Over a decade ago, Werstuck and Green had shown that some small molecules, tobramycin and kanamycin, had gene regulatory roles when bound to specific RNA aptamers.[213] Harvey et al. then demonstrated via translation assays that other small molecules, theophylline and caffeine, when bound to their specific RNA aptamers prevented ribosomal assembly at the 5′ UTR of the mRNA of interest.[85] Coincidentally, the RNA aptamers were located in tandem at the 5′ UTR. Altogether, their findings represented the first direct evidence of small molecules having an inhibitory effect on protein translation. One interesting finding by Harvey et al. was that biotin produced an enhanced inhibitory effect on translation while showcasing a relatively low binding affinity to its RNA aptamers, 6 μM.[85] Doxorubicin's binding to the IRE RNA is 0.7 μM. Also, of note, the exact step of inhibition during initiation complex assembly was not determined.

To date, there has not been an extensive characterization of an RNA/protein complex disruption by a small molecule. Yet, this study shows that doxorubicin is a satisfactory disruptor of this high-affinity interaction. As previously mentioned, the findings of Ma et al. consisted of the first direct evidence of a small molecule promoting up-regulation of translation. Despite its mild disruption of the RNA/protein complex in

mobility gel shift assays, ~8 %, yohimbine enhanced translation of the message downstream of the IRE RNA by up to 40 %. Similarly, our work in this chapter will focus on assessing the potential of doxorubicin to weaken the RNA/protein complex. Of note, I do not aim for doxorubicin to completely abolish the interaction, but rather only "nudge" it. The reason is that, eventually, manipulating iron homeostasis cannot consist of circumventing an entire regulatory system, instead, I would aim for careful regulation of protein synthesis.

Section 7.2: Methods

7.2.1. Relative electrophoretic mobility shift assays

The interaction of the IRE RNA, IRP and doxorubicin were monitored with relative electrophoretic mobility shift assays. Prior to any assay, the IRE RNA was re-folded as described above. RNA-protein-drug assays were incubated in 24 mM HEPES-KOH pH 7.2, 60 mM KCl, 0.2 mM EDTA, 2 % β-mercaptoethanol, 5 % glycerol for 30 min at room temperature without any order of addition. The RNA concentration and protein concentrations were kept constant at 0.2 µM and 1.1 µM, respectively. The drug concentration was varied from 0 to 100 µM. Free and bound RNA for each condition was resolved in 6 % (19:1) acrylamide/bisacrylamide nondenaturing gels. Gels were run at 4 °C at 100 V. Free and bound RNA were visualized by staining with ethidium bromide. All gel images were quantified using GeneTools, and plotted with GraphPad Prism 5.

7.2.2. Fluorescence quenching of hIRP-1 under doxorubicin

I performed quenching of intrinsic tryptophan fluorescence to determine apparent K_D values for the IRE RNA/IRP interaction under a series of concentrations of

doxorubicin and other small molecules. RNA/protein experiments were conducted on a JY Horiba Fluorolog-3 spectrofluorimeter equipped with a precise temperature control unit. Experiments were conducted at 25 °C and 12 °C, with an excitation wavelength of 280 nm, emission scanning wavelengths from 300 to 400 nm, and slit widths of 5 nm and 6 nm for excitation and emission, respectively. The titrations of IRE RNA into 150 nM hIRP-1 were carried out in a 24 mM HEPES-KOH pH 7.2, 60 mM KCl, 0.2 mM EDTA, 2 % β-mercaptoethanol buffer. The IRE RNA concentrations ranged from 1 nM to 900 nM, and the small molecule concentrations were either 10-, 100-, or 1000-fold than that of IRP. The fluorescence intensity at 335 nm was extracted and plotted against the RNA concentration titrated. Throughout the titrations, the IRP concentration was only decreased by < 2 %. The data were fit to a Langmuir binding isotherm to determine the apparent binding affinity. All experiments were done at least in triplicates. All data were analyzed and plotted with GraphPad Prism 5.

7.2.3. RNA preparation

Refer to Chapter 6, Section 6.2.1.

7.2.4. Iron regulatory protein expression and purification

Refer to Chapter 6, Section 6.2.2.

Section 7.3: Results

7.3.1. Gel mobility assays revealed a weak disruption of the IRE RNA/IRP complex

After showing that our IRE RNA construct bound to the IRP, I sought to assess the potential of doxorubicin as a disruptor of this interaction. I hypothesized that the drug

(K_D = 730 nM) would have a modest disruptive effect on the IRE/IRP complex (K_D = 9.1 nM), but that other small molecules would have no effect whatsoever on their binding. To test our hypothesis, I selected a condition in which I could observe both free and bound RNA, and then probed it with doxorubicin and other small molecules at varying concentrations.

Doxorubicin showed a mild disruption of ~3 % of the IRE/IRP complex. As seen in Figure 7.1, doxorubicin concentrations up to 100 μM produced no evident decrease in the IRE/IRP complex band intensity nor did it produce a notorious increase in the free IRE RNA band. Upon quantification of each band as a percentage of the total intensity of free and bound-RNA, I determined that at 100 μM doxorubicin, the IRE/IRP complex had decreased by 2.5 % (Figure 7.1c). This value, although small, is comparable in magnitude with a previously used small molecule, yohimbine, which caused a decrease of ~8 % of the complex.[75] Analogously to doxorubicin, daunorubicin also showed a mild disruption of 2.5 % of the IRE/IRP complex. Of note, the disruption pattern was more erratic and did not follow a strict dose-dependent perturbation of the complex.

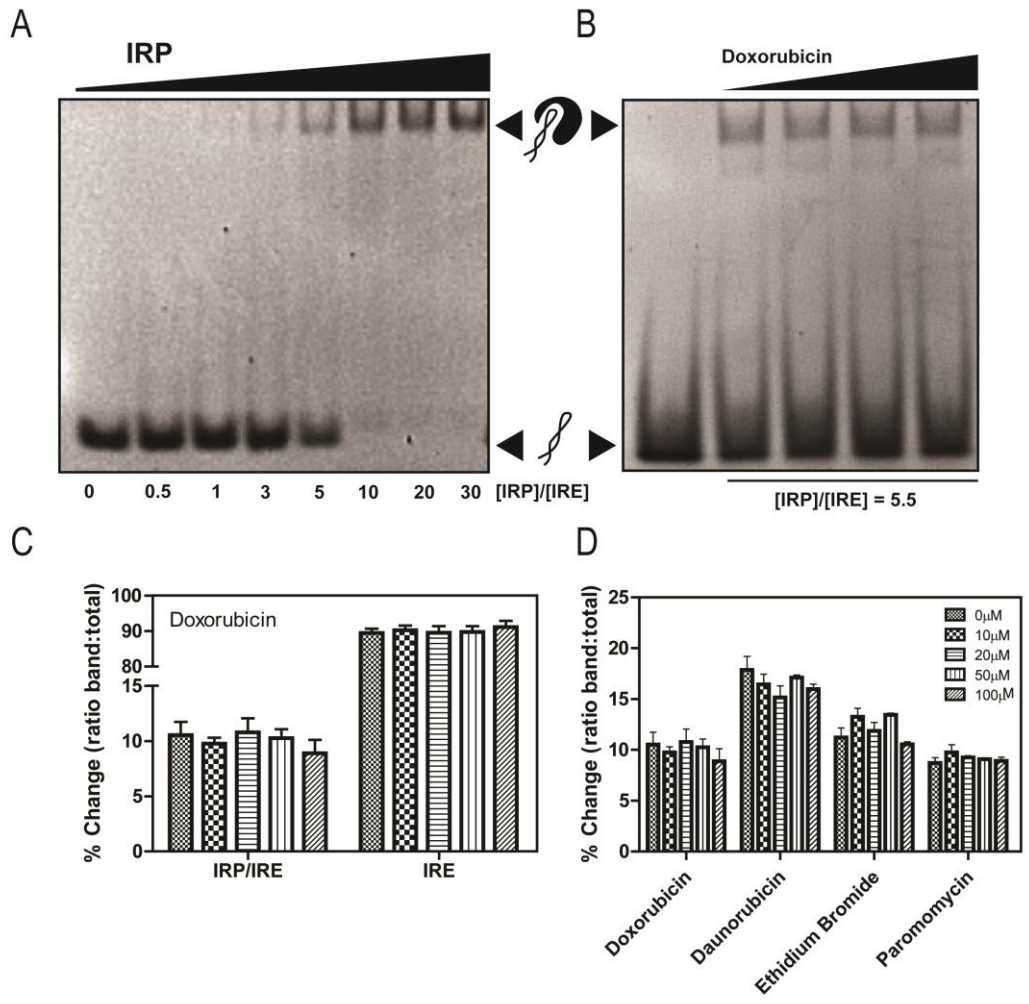

Figure 7.1. The IRE RNA/IRP binding affinity at micromolar concentrations remains unaffected in the presence of doxorubicin and other drugs. (A) Representative mobility gel shift assay that shows binding of the IRE RNA to the hIRP-1 at high protein/RNA ratios. (B) The RNA/protein complex was probed at increasing doxorubicin concentrations, showing the faint recovery of free RNA and minimal depletion of the complex. (C) Quantification of the gel shift assay in (b). The y-axis is the change in band intensity as a ratio of the IRE/IRP or IRE band to the sum of both. (D) Other RNA-binding drugs were used in identical experiments and identical quantifications were performed for the IRE RNA band. None of the other drugs seemed to cause any evident disruption of the complex. The legend of (d) applies to (c).

Interestingly, ethidium bromide caused a very mild disruption of the IRE/IRP complex. As seen in Figure 7.1d, ethidium bromide caused a mild decrease of the complex formation, by only 1 %. These results were surprising, as ethidium bromide is a well-characterized non-specific nucleic acid intercalator. At such high concentrations and molar ratios to the RNA and protein, ethidium bromide was expected to have a sizeable disruptive effect on the complex.

Other small molecules, namely aminoglycosides, did not show any IRE/IRP complex disrupting capability. Earlier, I showed that paromomycin had no observable competition for doxorubicin's binding site (Figure 5.2c). Therefore, I probed the IRE/IRP complex stability with paromomycin. Even at a concentration of 100 μM, it had no disruptive effect on the complex (Figure 7.1d). Of note, other small molecules, streptomycin and kanamycin did not have any disruptive effects.

Altogether, our results showed that doxorubicin had a very minor disruptive effect on the IRE/IRP complex. Additionally, daunorubicin and ethidium bromide showed a similar effect to doxorubicin. Lastly, paromomycin showed no disruptive effect on the IRE/IRP complex.

7.3.2. Fluorescence experiments showed a sizeable effect of doxorubicin on the IRE/IRP complex

Next, I aimed to further characterize and obtain more quantitative information on the disruptive effect of doxorubicin with the IRE/IRP complex at more physiologically relevant concentrations. I hypothesized that at nanomolar concentrations of the molecular players, the disruptive effect of doxorubicin and other molecules is likely greater than 3

%. To test our hypothesis, I performed intrinsic fluorescence spectroscopy experiments to measure the apparent dissociation constant of the IRE/IRP complex in the presence of various concentrations of doxorubicin and other small molecules. These experiments were identical to those used above to measure the apparent binding constant of the IRE/IRP complex.

To our surprise, doxorubicin increased the IRE/IRP complex apparent dissociation constant from 9.1 ± 0.4 nM to 16.7 ± 0.9 nM at a 100:1 doxorubicin:IRP complex ratio. The binding of IRE/IRP was partially impeded by doxorubicin, by weakening its apparent binding affinity by nearly two-fold (Figure 7.2a). In terms of their molecular stabilities (K_A), the RNA/protein complex was affected by reducing its stability from (110 ± 5) x 10^6 M^{-1} to (60 ± 3) x 10^6 M^{-1} at 15 µM doxorubicin, accounting for a destabilizing effect of ~45 % (Figure 7.2b). At first glance, these results are contradictory of the ~3 % disruption of the RNA/protein complex caused by doxorubicin as observed by gel-shift assays (Figure 7.1c). However, the design of the fluorescence experiments herein present an intrinsic advantage toward doxorubicin-mediated disruption: lower protein concentrations; and more free RNA available for drug-binding. I also showed that the disruption of the RNA/protein complex was dose-dependent on the doxorubicin:IRP molar ratio (Figure 7.2a-b). Also, as explained above, the dimerization of doxorubicin near and above 20 µM has been suggested; this process likely interferes with RNA-binding in the prior gel-shift assays, thus also reconciling our results.

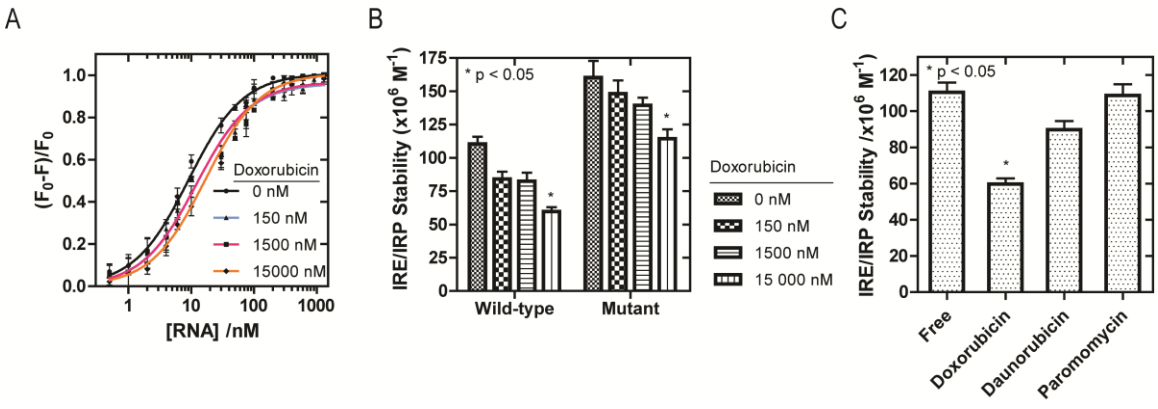

Figure 7.2. The IRE RNA-IRP binding affinity at nanomolar concentrations is affected by doxorubicin. (a) Upon addition of doxorubicin, the apparent binding affinity of the complex is shifted toward larger values two-fold. (b) The molecular stabilities (K_A) of the RNA/protein complex is affected by 45 % in the wild-type RNA, whereas the G22A,G25A mutant RNA is only affected by 29 %. (c) In identical experiments, the addition of daunorubicin and paromomycin had a significant and no observable effect, respectively, in the apparent binding affinity of the RNA/protein complex.

Furthermore, the G22A,G25A IRE RNA/IRP complex showed a less marked response to doxorubicin than its wild-type counterpart. The apparent binding affinity of the RNA/protein complex at 15 µM doxorubicin was determined to be 8.7 ± 0.5 nM, compared to 6.2 ± 0.5 nM without drug. As shown in Figure 7.2b, this corresponded to a disturbance of molecular stability from (160 ± 10) x 10^6 M^{-1} to (114 ± 7) x 10^6 M^{-1} at 15 µM doxorubicin, accounting for a destabilizing effect of ~29 %. These findings were expected, resulting from a combination of tighter affinity of the mutant RNA to the protein partner and a weaker binding of the drug to the mutant RNA.

Daunorubicin showed a decreased ability to disrupt the IRE RNA/IRP complex in comparison to its stronger-binding analog doxorubicin. Previously, I did not observe any major disruptive effect of daunorubicin on the RNA/protein interaction (Figure 7.1d).

However under the specific conditions used in this fluorescence assay I were able to observe a sizeable disruption of the complex at 15 μM drug. The molecular stability of the IRE RNA/IRP complex was decreased from $(110 \pm 5) \times 10^6\ M^{-1}$ to $(90 \pm 5) \times 10^6\ M^{-1}$ (Figure 7.2c). The extent of disruption could be reconciled with the experimental evidence that daunorubicin had a decreased affinity to the IRE RNA, 1300 nM.

Other drugs did not show any disruption of the RNA/protein complex. As expected, the RNA-binding drug paromomycin had no effects on the RNA/protein formation at similar micromolar concentrations (Figure 7.2c). The latter results were in line with our previous competition assays where paromomycin was unable to displace doxorubicin from the IRE RNA (Figure 5.2c).

Altogether, in the last three chapters, our results have supported our hypotheses: (i) Doxorubicin interacts with the IRE RNA with a preference for G•U wobbles flanked by G-C base pairs; and (ii) this chemotherapeutic agent is able to disrupt the IRE RNA/IRP complex. A close derivative of doxorubicin, daunorubicin is also able to disrupt the RNA/protein complex, but to a lesser extent. Other small molecules were nearly harmless to the complex. Finally, when the G•U wobble base pairs are swapped for A-U base pairs, the disruptive effect of doxorubicin on the molecular stability of the IRE RNA/IRP complex was lessened by nearly 20 %.

Section 7.4: Discussion

Doxorubicin is a strong chemotherapeutic agent widely used for a variety of carcinomas and its mechanism of action has been extensively characterized.[54–56] Its main interactions have been shown to be with genomic DNA, preventing cell division.

However, non-specific interactions were suggested, and recently, this drug was shown to bind to the Iron Responsive Element (IRE) RNA *in vitro*.[61] The RNA/doxorubicin interaction, however, was not entirely characterized.

In this thesis, I biophysically and biochemically characterized the interaction of doxorubicin with the consensus human H-ferritin IRE RNA. The apparent dissociation constant of the IRE/doxorubicin complex was 730 nM, which was within an order of magnitude of previous work, 904 nM.[61] I showed, from our NMR results, that doxorubicin intercalated between two G•U wobble and their flanking G-C base pairs. Additionally, I observed sizable RNA melting without a major conformational change in the IRE RNA structure. In previous chapters, I had laid the foundation for understanding how doxorubicin may disrupt the IRE/IRP complex. I proposed a model by which doxorubicin intercalates between G•U and G-C base pairs, potentially promoting partial helical melting.

To our knowledge, there are few examples of small molecules that disrupt RNA/protein complexes. Malina et al. use doxorubicin to study the effect of nucleic acid binders in wheat germ extract protein translation.[55] It was found that doxorubicin reduced translation of a bioluminescent reporter construct; however no specific target was attributed to its mechanism of action. Interestingly, all nucleic acid binders used in such study lowered translation levels. Currently, there is only one example of small molecule-induced protein translation enhancement which involves a similar IRE/IRP system used in our study.[75] As stated previously, yohimbine was shown to deplete the IRE/IRP complex by 8 %. However its ultimate effect in wheat germ translation was an enhancement of nearly 40 % of reporter constructs. Such enhancement in translation can

be expected in part due to the non-linear nature of an *in vivo* gene regulatory system; however, the magnitude was harder to reconcile.

In this chapter, I evaluated the potential of doxorubicin as an IRE/IRP complex disruptor. Previously I had analyzed the crystallographic evidence of the RNA/protein complex, and I highlighted its weaknesses. Therefore, if doxorubicin is capable of reaching the major groove of the G•U wobbles, even during a protein-bound state, it may be able to disrupt these base pairs and exert its partial helix melting action. This would in turn promote dissociation of the RNA/protein complex. Our results showed that the IRE RNA/IRP complex's apparent binding affinity was weakened from 9.1 nM to 16.7 nM at 15 μM doxorubicin. This is equivalent to a molecular stability (K_A) destabilization of 45 %. Due to the relatively low disruptive effect in terms of binding affinities, I carried out identical experiments at 12 °C to further validate our results (data not shown). As expected, the apparent binding constant was 2.1 nM, nearly four-fold stronger than at 25 °C. The destabilizing effects of doxorubicin were comparable to those at 25 °C; the apparent K_D at 15 μM doxorubicin was 4.6 nM (~52 % disruption in terms of molecular stability). In addition, the effects of doxorubicin's close analog, daunorubicin, on the RNA/protein complex were similar, yet less pronounced. Paromomycin, a known RNA major groove binder, had no disruptive effect on the RNA/protein complex. Unfortunately, the effects of ethidium bromide were not observable under our specific tryptophan fluorescence assay conditions due to its strong absorbance near the excitation wavelength used. However, our relative electrophoretic mobility shift assays showed that this nucleic acid stain did not have a sizeable disruptive effect on the complex.

The potential of doxorubicin to disrupt the IRE/IRP complex *in vitro* may reconcile previous *in vivo* data.[59,60,214] In Kwok and Richardson's work, they observed that subjecting myocardial and neoplastic cells to doxorubicin decreased IRP's RNA-binding activity.[59,60] They observed a biphasic behavior, first of decreased IRP-bound RNA, followed by a rapid recovery of actively-binding IRP when cells were exposed to 20 μM doxorubicin. Additionally, they did not observe major depletion of the total IRP concentration. Furthermore, they showed that incubation of these cell lines with doxorubicin increased Fe(II) storage in ferritin three-fold. Interestingly, they showed a two-fold increase in expression of H-ferritin. In this work, I showed how doxorubicin decreased the apparent binding affinity of IRP to IRE nearly two-fold. Henceforth, our findings allow us to propose a simple model by which doxorubicin displaces hIRP-1 from binding to the H-ferritin IRE RNA. I propose that doxorubicin intercalates between two G•U/G-C base pairs in the IRE RNA, promoting partial helix melting, thus altering the structure of the RNA and precluding it from binding to hIRP-1. Disruption of the RNA/protein complex would then allow for formation of the 40S pre-initiation complex. This model may explain both the increased ferritin expression and storage of Fe(II) observed in cell lines exposed to doxorubicin.

Altogether, I have presented how doxorubicin is able to partially disrupt a strong IRE RNA/hIRP-1 interaction. Despite the large differential in affinities of the RNA to each molecular player, doxorubicin is capable of lowering the affinity of hIRP-1 to the IRE RNA. Ongoing work in our laboratory is focused in obtaining a solution structure of the RNA-doxorubicin complex. I are also developing NMR technologies to characterize the interaction between the IRE RNA and the 98 kDa hIRP-1 also under the presence of

doxorubicin to fully discard the possibility of a tripartite complex. Alongside, I are conducting studies in the presence of a series of divalent metal ions, which have been shown to also disrupt the IRE/IRP complex.[64] Preliminary results utilizing the Fe(II) surrogate, Mn(II), have shown decreased affinity of the RNA to doxorubicin, but an increase of this drug's disruptive effect on the complex.

This study expands on the number of small molecules that disturb RNA/protein complexes in charge of down-regulating downstream mRNA translation. Further development of this proof of principle may result in promising therapies of certain diseases that could benefit from overexpression of proteins. Applying this approach to the IRE RNA-IRP regulatory system may also lead to novel adjuvant therapies of non-iron deficiency anemia that replace noxious iron chelators.[11,81,82] For instance, overexpression of iron-storage proteins such as ferritin would ameliorate secondary iron overload produced by recurring blood transfusions in sickle cell, β-thalassemia anemic, or hereditary hemochromatosis patients.[78,81]

Chapter 8: Conclusions and Future Directions

Section 8.1: Contributions toward a "cure" for anemia

The treatment of non-iron deficiency anemia and iron-overload diseases has, for long, focused in palliation rather than a definite cure.[6,215] Many common diseases such as sickle cell anemia and β-thalassemia are treated mainly by recurring blood transfusions and supplemented with subcutaneous or oral iron chelators.[216,217] The latter component is used to ameliorate transfusional iron overload. Unfortunately, the risks of using iron chelators such as deferiprone or deferoxamine may outweigh their benefits.[21] For that reason, in our work, I proposed to sidestep iron chelation therapies for newer biomolecular therapeutics, approaching safer intracellular iron storage with a novel approach.

In our work, I aimed at disrupting an RNA/protein complex responsible for down-regulating the expression of iron-storage proteins. I showed that a small chemotherapeutic drug, doxorubicin, is able to mildly disrupt the IRE RNA/IRP complex (Figure 7.2). Our results indicate that further development of this drug, or screening for similar RNA intercalators, may lead to potential leads for increasing ferritin synthesis *in vivo.*

Our studies represent the initial steps toward renewal of current treatments of anemia, rather than proposing an actual cure. As mentioned previously, the worldwide prevalence of anemia is striking, affecting nearly one out of four individuals globally.[1] One of the main reasons that treatments are palliative rather than curative is the vast etiology generating this disease, especially non-iron deficiency anemia. Many authors

have addressed the current status of the development of new treatments.[218,219] Unfortunately, to date, not much progress has been made, in part due to the lack of a consistent molecular mechanism within all variants of the disease.[216,217,219–222] Ongoing research is focused in developing personalized gene therapies, however, this field has seen more rapid progress in cancerous diseases rather than anemia.[223–225]

Section 8.2: The advent of RNA-targeted therapeutics & other approaches

In Chapter 2, I stated that molecular medicine is mainly focused in targeting proteins with small molecules for the sake of a medical benefit. Our work is another stepping stone toward RNA-targeted therapeutics. I do not claim that, by any means, that doxorubicin is to be used as a molecular therapeutic. Rather I claim that there is potential for regulatory RNA elements, such as the IRE RNA, to be targeted for therapeutics of not only anemia, but any disease that could benefit from a renewed form of treatment. The work presented herein represents a proof of concept that careful manipulation of RNA/protein interactions can be achieved and perhaps exploited in future therapeutics.

RNA has long been a target of bacterial antibiotics, and I believe it is time to exploit the full scope of RNA functionality.[50] The potential of RNA as a target is highlighted by this biomacromolecule's ubiquity in various biological processes. In our work, I only present a system involved in iron homeostasis; however many RNA-based regulatory systems exist in eukaryotes and higher mammals, especially since the advent of the human genome project[147] when it was unveiled that the vast majority of the human genome codes for non-protein coding RNAs.

The use of doxorubicin as an RNA/protein complex disruptor is not the only approach that can be used to achieve our long term impact. I acknowledge that in contrast to the approach presented in our work, several pathways in the synthesis of iron storage proteins may be targeted. For instance, introducing a small-interfering RNA (siRNA) complementary to the mRNA of hIRP-1 would also achieve up-regulation of iron storage proteins.[226] Another potential approach to preventing the IRE/IRP interaction could involve the use of locked nucleic acids (LNAs).[227] These have been shown to have enhanced binding to RNA, significantly contributing to duplex stability. Hence LNAs could behave as competitors against IRP binding and achieve the similar desired regulatory effects.

Section 8.3: Future directions

The thesis work presented herein consists only of the initial steps of our laboratory in the field of RNA-drug interactions and development of NMR technologies. In this section, I present a series of ideas that may represent future work to be performed not only in the matters concerning this thesis, but also in general for our laboratory. As well, within each sub-section, I present a series of desired improvements for the experimental work performed thus far.

8.3.1. Development of novel technologies for the NMR of RNA

In our work (Chapters 3 and 4), I showed how the utilization of $^{13}C/^{15}N$ site-specifically labeled nucleotides improved the analysis of RNA structural and dynamic parameters by NMR. Our yields of nucleotide synthesis were consistently > 90 %, the reaction times < 24 h, and the experimenter hands-on labor minimized < 6 h. The spectral resolution and sensitivity obtained with our custom-made nucleotides as consistently

improved, I eliminated the need for lengthy decoupling pulses; field of NMR should benefit considerably using these labels with larger RNAs. Nonetheless, there is always room for improvement in specific areas of this project.

- Most certainly, to validate our results and our predictions, I have to utilize our custom-made labels to synthesize RNAs >50 nucleotides
- Ideally, in the synthesis of CTP from UTP, I will incorporate an ATP-regeneration system. The excessive use of an expensive substrate, dATP, may become limiting over time.
- Also, the concentration of CTP used, 2 mM, may be further improved, to reduce reaction volumes.
- Our collaborator, Dr. Cristoph Kreutz at the University of Innsbruck, is currently working on synthesizing deuterated uracil. A ^{2}H isotope in the C5-H5 spin system would prove exceedingly useful in NMR analysis due to its overlap with H1′ resonances. As well, it would improve the relaxation properties of the C6-H6 system, due to the lack of $^{3}J_{HH}$ coupling.
- In the topic of deuteration, if deuterated ribose molecules become more readily available or if I can carry out its chemical synthesis, then I would obtain a very useful and versatile labeled nucleotide.
- As well, Dr. Kreutz is currently synthesizing 8-^{13}C-guanine. Current work in our lab is devote to optimizing the synthesis of GTP in a similar manner to the synthesis of UTP showcased in this thesis.
- From a technical perspective, boronate affinity chromatography is effective for the purification of nucleotides, and I were able to automate it in the FPLC.

However, I suggest changing the wash buffer (TEABC) to another buffer system that is less hazardous to the experimenter.

8.3.2. Use of small molecules to disrupt RNA/protein complexes

In our work (Chapters 5 through 7), I showed that doxorubicin is modest disruptor of the IRE/IRP complex. I utilized biochemical and biophysical tools to support our hypotheses of drug-binding, intercalation, helix melting, and complex weakening. Our results showed a complex weakening by ~50 %. Nevertheless, below I present a series of experiments and complementary data that I suggest be obtained in the future. Some of these items are currently under work in our laboratory.

- Continue the resonance assignment for the IRE RNA.
- Map chemical shift perturbations across the IRE RNA when doxorubicin is titrated into the sample.
- Carry out ligand-observed experiments, as mentioned in Chapter 5.
- Perform two- and three-dimensional filtered NMR titration experiments to observe direct effects of doxorubicin on the IRE RNA.
- Incorporate our $^{13}C/^{15}N$ site-specifically labeled nucleotides in assessing the change in residue dynamics when the IRE RNA is bound by doxorubicin.
- Despite the poor solubility of doxorubicin in NMR buffer, attempt to obtain a solution structure of the RNA/doxorubicin complex.
- As well, derivatize doxorubicin to increase its solubility in phosphate-based buffers.
- Our collaborator, Dr. Yomi Oyelere at the Georgia Institute of Technology, is currently working on synthesizing doxorubicin derivatives that may also bind to

the IRE RNA. This would in turn allow us to determine the minimal binding component of doxorubicin, to then further functionalize the molecule to attain both higher affinity and specificity to the RNA.

- Utilize various other IRE RNA constructs, for instance, the whole human sequence which features a more extended lower stem compared to the construct used herein. If the full human H-ferritin IRE RNA has a stronger affinity to doxorubicin, then this drug's disruptive ability of the IRE/IRP complex may be enhanced. Additionally, I may utilize 3′ UTR RNAs, such as the transferrin receptor IRE RNA. These are responsible for the post-transcriptional regulation of the transferrin receptor, which is involved in cellular iron uptake from diferric-transferrin.[38,68,228]

Appendices

The Appendix section will be divided into detailed experimental protocols and supplementary data that was referred to in the text.

Detailed experimental methods:

Protocol: Protein Overexpression of BL2AI strains with pET15b vector:

Timing: One Overnight + 12 hours

- Plate cells (no more than 10µl) in LB plate with 100µg/ml Ampicillin (from now on, Amp). Grow overnight (O/N).
- Use single colony to inoculate a 25-mL culture in LB media with Amp. Grow @ 37°C, 270rpm until OD ≈ 0.6. (About 4.5h)
- Pellet cells @ 3500rpm, 15', 4°C. Discard supernatant. Resuspend pellet in 25mL of LB with Amp
- Inoculate 5mL into 100mL LB with Amp.
- Grow @ 37°C, 270rpm until OD ≈ 0.6 (About 1.5h)
- Pellet cells @ 3500rpm, 15', 4°C. Discard supernatant. Resuspend pellet in 100mL of LB with Amp. (Usually done in two 50-mL fractions)
- Defrost stocks of arabinose
- Inoculate 20mL into 1L LB with Amp.
- Take a 5mL sample (in a falcon tube) to serve as the UNinduced control. Let grow @ 37°C, 270rpm until all inductions are done. Pellet and resuspend in SDS-PAGE buffer or loading solution, then freeze at -20°C.
- Induce the culture with 0.05% L(+)-arabinose for 2h @ 270rpm, 37°C.
- Defrost stocks of IPTG
- Induce with 1mM IPTG for 3h @ 270rpm, 37°C

- Take a 1mL sample (in eppendorf) to serve as the Induced control. Pellet and resuspend in SDS-PAGE buffer or loading solution, then freeze at -20°C.
- Pellet the 1L culture @ 5500rpm for 15', 4°C. Discard supernatant.
- Weigh wet cells.
- Alternative 1: Store pellet at -20°C.
- Alternative 2: Go on to Cell Lysis Protocol
- Note: Usually, the 1L culture can be done in quadruplicate. Previous yield has been of ≈ 16 – 21g / 4L

Protocol: Cell Lysis using Sonication

Timing: 3h - 3h 30'

- Thaw cells in ice for 15'
- Resuspend cell pellet in Lysis buffer. Use ~2mL/g of pellet. Mix gently.

50mM $NaPO_4$	6.90g NaH2PO4·H2O
300mM NaCl	17.54g NaCl
10mM imidazole	0.68g imidazole
QIAexpressionist p114	pH 8.0

- Add lysozyme, 1mg/mL. Incubate on ice for 30'.
- Sonicate at 40% duty for 1', 45s cooling. Perform three times.
- Add RNase A (10µl/mL) and DNase I (5µl/mL). Incubate on ice for 20'.
- Prep Ni-NTA column.
- Centrifuge lysate @ 46 000g (20 000rpm) for 25' @ 4°C
- Continue prep Ni-NTA column.
- Remove gDNA manually by pipetting carefully
- Remove supernatant
- Take a 20µL sample for enzyme activity assay. Preferably, measure activity ASAP, or else freeze at -20°C

- Take another 20µL sample for SDS-PAGE. Add 20µl of 2X SDS loading solution, freeze at -20°C.
- Take 20µL sample for Bradford Assay. Add 80µL of lysis buffer. Add 3mL of Bradford reagent. Let sit for 10', measure OD at 595nm.
- Optional (Adds 1h 30'): Resuspend cell pellet with a minimum amount of lysis buffer, and sonicate again at 40% duty for 1', 45s cooling. Perform three times. Centrifuge lysate @ 46 000g (20 000rpm) for 25' @ 4°C. Remove gDNA. Consolidate supernatants, and dispose of pellet.

Ni-NTA Column Purification of Pentose Phosphate Pathway Proteins

Timing: 12 – 14 hours

- Prep of column:
  - Retrieved beads from fridge. Poured them in column, collected the flow-through (FT). Beads Volume = 6 ml
  - Washed column with 20ml of 0.5M EDTA pH 8.1).
  - Washed with 50ml of water.
  - Added 20ml of 1X $NiCl_2$ solution (stock is 400mM, 8X). Collected FT
  - Added 25ml of lysis buffer (50mM Na3PO4 pH 8.0, 300mM NaCl, 10mM imidazole). Collected FT
  - Capped, and transferred to cold room. Let sit for 20'. Column is ready
- Purification:
  - Place _____ WCL supernatant on column. Collected __ml of **Flow Through**. Retrieved a 20µl aliquot for SDS PAGE
  - Add 75ml of wash buffer (50mM $Na3PO_4$ pH 8.0; 300mM NaCl; 50mM imidazole). Collected __ml of **W1**. Retrieved a 20µl aliquot for SDS PAGE
  - Wash #2, add 75mL of wash buffer, collected __ml of **W2**, Idem. Retrieved aliquot.

- Add 10ml of elution buffer (Wash buffer, with 400mM imidazole instead). Collected 10ml of **E1**. Retrieved a 20µl aliquot for SDS PAGE
- Elution #2, add 10mL of elution buffer collected 10ml of **E2**, Idem. Retrieved aliquot
- Reduce sample volumes to 2mL with 3K MWCO tubes. Spun at 4000rpm for 30' @ 4C. Then, add 10ml of storage buffer and re-spun at 4000rpm for 30' @ 4C.
- Repeat this last step at least 3 – 4 times.
    - Storage buffer for RK, UPRT, XGPRT, APRT and CTPS: 50mM Na3PO4 pH 7.5, 150mM NaCl
    - Storage buffer for PRPPS: 50mM Na3PO4 pH 7.5, 300mM NaCl
- Took a 10µl aliquot for Bradford assay.
    - OD = _.__ → _.___mg/ml → x10X-dilution → **__.__mg/ml in _ml**
    - Total isolated = **__.__mg**
- Add 1 volume of glycerol, note the final effective concentration
- Stored ___ ___ as one __.__mg/ml in 50% glycerol stock, 2mM β-mercaptoethanol

- Recycling:
    - Retrieved beads with 30% ethanol into a falcon tube
    - Place in fridge at 4°C

Protocol for T7 RNA Polymerase Purification:

Timing: 12 – 14 hours

Cell Lysis

- Thaw ____g of cells in ice for 15'
- Resuspended cell pellet in __mL of lysis buffer (20mM NaH_2PO_4 pH 8; 500mM NaCl; 5mM imidazole; 0.05% Tween 20; 1mM PMSF added). Mixed gently. Generally, 10mL will dissolve 1g of pellet.
- Added __mg lysozyme (to 1mg/mL). Incubate on ice for 30'

- Sonicated at 40% duty for 1min, 30s cooling. Performed twice.
- Centrifuged lysate @ 25 000rpm for 30’ @ 4°C
- Removed gDNA manually by pipetting carefully
- Transferred __ml of supernatant to falcon tube.
- Took a 20µL sample for SDS-PAGE. Added 20µl of 2X SDS loading solution, heated at 95C for 10’.
- Took a 10µL sample for Bradford Assay. Added 90µL of lysis buffer. Add 3mL of Bradford reagent. Let sit for 10’, measured OD at 595nm.
    - OD = _.__ → _.___mg/ml → x10X-dilution → **__.__mg/ml in __ml**

Ni-NTA Column Purification

- Prep of column:
    - Retrieved beads from fridge. Poured them in column, collected the flow-through (FT). Beads Volume = __ml (Capacity: 50mg of protein / 1 mL of beads)
    - Washed column with 25ml of 0.5M EDTA. Collected FT
    - Washed with 50ml of water.
    - Added 20ml of 1X $NiCl_2$ solution (stock is 400mM, 8X). Collected FT
    - Added 25ml of lysis buffer. Collected FT
    - Capped, and transferred to cold room. Let sit for 20’. Column is ready

- Purification:
    - Placed _____ WCL supernatant on column. Collected __ml of **FT**. Retrieved a 20µl aliquot for SDS PAGE
    - Added __ml of wash buffer (20mM NaH_2PO_4 pH 8; 500mM NaCl; 8mM imidazole). Collected __ml of **W1**. Retrieved a 20µl aliquot for SDS PAGE

- Wash #2, collected __ml of **W2**, Idem. Retrieved aliquot
- Added 10ml of elution buffer (Wash buffer pH 8, with 100mM imidazole instead). Collected 10ml of **E1**. Retrieved a 20µl aliquot for SDS PAGE
- Elution #2, collected 10ml of **E2**, Idem. Retrieved aliquot
- Reduce sample volumes to 1mL with Amicon 3K ultra MWCO tubes. Spun at 4000rpm for 1h @ 4C. Then, added 10ml of storage buffer (20mM Na_3PO_4, 0.1mM EDTA, 1mM DTT, 150mM NaCl – pH 7.6)
- , and re-spun at 4000rpm for 1h @ 4C.
- Took a 10µl aliquot for Bradford assay.
  - OD = _.__ → _.___mg/ml → x10X-dilution → **__.__mg/ml in _ml**
  - Total isolated = **__.__mg**
- Stored T7 RNAP as one __.__mg/ml in 50% glycerol stock

- Recycling:
  - Retrieved beads with 30% ethanol into a falcon tube
  - Place in fridge at 4°C

Activity Assays for Various Enzymes Used (and not used) in this Work

Protocol: Enzyme activity assay by spectrophotometry

- PRPP Synthetase
  - Reaction mixture: 1mL
  - Incubate mixture for 5'.
  - Mix 10µl PRPPS + 90µl of 55.6mM Tris-HCl pH 7.5.
  - Note: 100-fold dilution from stock.
  - Add 40 µl of PRPPS solution to assay.
  - Note: 250-fold dilution from solution.
  - Monitor ΔA_{340} over time every 10s.
  - Calculate activity as:

$$U = \frac{\frac{1}{2} * V * \Delta A340}{6220 * t * l}$$

Where, V is volume in L, t is time consistent with ΔA_{340}, and l is path length in cm.

H2O	647µl
Tris-HCl pH 7.5	50mM (50µl of 1M)
R5P	5mM (100 µl of 50mM)
ATP	3mM (30 µl of 100mM)
PEP	1mM (20 µl of 50mM)
MgCl2	10mM (10 µl of 1M)
NADH	0.4mM (100 µl of 4mM)
LDH	2U (1µl)
Pyr Kin	2U (1µl)
MyoKin	2U (1µl)

- Ribokinase
  - Reaction mixture: 1mL
  - Incubate mixture for 5'.
  - Mix 10µl Rbsk + 90µl of 55.6mM Tris-HCl pH 7.8.
  - Note: 100-fold dilution from stock.
  - Add 40 µl of RbsK solution to assay.
  - Note: 250-fold dilution from solution.
  - Monitor ΔA_{340} over time every 5s.
  - Calculate activity as:

$$U = \frac{V * \Delta A340}{6220 * t * l}$$

Where, V is volume in L, t is time consistent with ΔA_{340}, and l is path length in cm.

H_2O	548µl
Tris-HCl pH 7.8	50mM (50µl of 1M)
Ribose	5mM (100 µl of 50mM)
ATP	3mM (30 µl of 100mM)
PEP	1mM (20 µl of 50mM)
MgCl2	10mM (10 µl of 1M)
KCl	100mM (100µl of 1M)
NADH	0.4mM (100 µl of 4mM)
LDH	2U (1µl)
Pyr Kin	2U (1µl)

- APRT
  - Reaction mixture: 1mL
  - Incubate mixture for 5'.
  - Add all components except adenine
  - Mix 10µl APRT + 90µl of 55.6mM Tris-HCl pH 7.8.
  - Add adenine to start the reaction
  - Add 40 µl of APRT solution to assay.
  - Monitor ΔA_{340} over time every 10s.
  - Calculate activity as:

$$U = \frac{\frac{1}{2} * V * \Delta A340}{6220 * t * l}$$

Where, V is volume in L, t is time consistent with ΔA_{340}, and l is path length in cm.

H2O	657µl
Tris-HCl pH 7.8	50mM (50µl of 1M)
PRPP	1.5mM (75µl of 20mM)
ATP	3mM (30 µl of 100mM)
PEP	1mM (20 µl of 50mM)
Ade HCl	1.5mM (15µl of 100mM)
MgCl2	10mM (10 µl of 1M)
NADH	0.4mM (100 µl of 4mM)
LDH	2U (1µl)
Pyr Kin	2U (1µl)
Ade Kin	2U (1µl)

- XGPRT
  - Reaction mixture: 1mL
  - Incubate mixture for 5'.
  - Add all components except Guanine
  - Mix 10µl XGPRT + 90µl of 55.6mM Tris-HCl pH 7.5.
  - Add 40 µl of XGPRT solution to assay.
  - Add Guanine to start the reaction
  - Monitor ΔA_{257} over time every 10s @ 37°C (or RT) for 12-15min.
  - Calculate activity as:

$$U = \frac{V * \Delta A257}{5817 * t * l}$$

Where, V is volume in L, t is time consistent with ΔA_{257}, and l is path length in cm.

H2O	685µl
Tris-HCl pH 7.5	100mM (100µl of 1M)
PRPP	1mM (50 µl of 20mM)
MgCl2	100mM (100 µl of 1M)
Gua	50µM (25 µl of 2mM)

- UPRT
  - Reaction mixture: 1mL
  - Add all components except Uracil.
  - Mix 10µl UPRT + 90µl of 55.6mM Tris-HCl pH 8.5.
  - Note: 100-fold dilution from stock.
  - Add 40 µl of UPRT solution to assay.
  - Note: 250-fold dilution from solution.
  - Incubate mixture for 5'.
  - Add Uracil to start the reaction.
  - Monitor ΔA_{271} over time every 10s @ 37°C (or RT) for 12-15min.
  - Calculate activity as:

$$U = \frac{V * \Delta A271}{2763 * t * l}$$

Where, V is volume in L, t is time consistent with ΔA_{271}, and l is path length in cm.

H_2O	810µl
Tris-HCl pH 8.5	20mM (20µl of 1M)
PRPP	1.5mM (75 µl of 20mM)
MgCl2	5mM (5µl of 1M)
(GTP)	1mM
Ura	0.1mM (50 µl of 2mM)

- CTP synthase
  - Reaction mixture: 1mL
  - Add all components except glutamine
  - Mix 10µl CTPS + 90µl of 55.6mM Tris-HCl pH 7.8.
  - Add 40 µl of CTPS solution to assay.
  - Incubate mixture for 5'.
  - Add glutamine to start the reaction
  - Monitor ΔA_{291} over time every 5s @ 37°C (or RT) for 15min.
  - Calculate activity as:

$$U = \frac{V * \Delta A291}{1338 * t * l}$$

Where, V is volume in L, t is time consistent with ΔA_{291}, and l is path length in cm.

H2O	867.5µl
Tris-HCl pH 8.0	50mM (50µl of 1M)
MgCl2	10mM (10µl of 1M)

Either Glutamine	10mM (50µl of 200mM)
UTP	1mM (10µl of 100mM)
ATP	1mM (10µl of 100mM)
GTP	0.25mM (2.5µl of 100mM)

- CTP synthase (NMR Assay)
    - Reaction mixture: 1mL, but prepare two mixtures, one will be Assay, the other will be Control.
    - Add all components except glutamine and enzyme
    - Aliquot 228µl for two assays into two separate eppendorf tubes.
    - Mix 10µl water + 90µl of 55.6mM Tris-HCl pH 8.
    - Add 40 µl of control solution to Control assay.
    - Add 50µl of glutamine to Control assay.
    - Mix 10µl CTPS + 90µl of 55.6mM Tris-HCl pH 8.
    - Add 10µl of CTPS solution to each assay eppendorf. DON'T add glutamine yet.
    - Incubate mixtures for 5' @ 37°C.
    - Transfer both assay tubes and 250µl of the control into NMR tubes.
    - Aliquot 12.5µl of glutamine into two separate eppendorfs.
    - Bring the reaction vessels, glutamine tubes, NMR pipets, etc down to the NMR room.
    - Add 12.5µl of glutamine to start the reactions
    - Monitor U and C's C1',C5 over time for the appearance of ^{13}C-^{15}N-CTP.
    - Additionally, prepare a product standard solution with 2mM ^{13}C-^{15}N-CTP under the same conditions of assay, except use no enzyme and cold UTP.

Sample Preparation (1 mL to be split)	
H_2O (or D_2O)	737.5µl
D_2O	10% (100µl of 100%)
DSS	0.24mM (20µl of 12mM)
NaN_3	1mM (10µl of 100mM)

Tris-HCl pH 8.0	50mM (50µl of 1M)
$MgCl_2$	10mM (10µl of 1M)
^{13}C-^{15}N-UTP	1mM (10µl of 100mM)
ATP	1mM (10µl of 100mM)
GTP	0.25mM (2.5µl of 100mM)

Product standard solution (250 µl)	
D_2O	204.4µl
DSS	0.24mM (5µl of 12mM)
NaN_3	1mM (2.5µl of 100mM)
Tris-HCl pH 8.0	50mM (12.5µl of 1M)
$MgCl_2$	10mM (2.5µl of 1M)
Glutamine	10mM (12.5µl of 200mM)
UTP	1mM (2.5µl of 100mM)
^{13}C-^{15}N-CTP	2mM (5µl of 100mM)
ATP	1mM (2.5µl of 100mM)
GTP	0.25mM (0.63µl of 100mM)

- Phosphopentomutase:
  - Prepare enzyme mixture
  - Incubate on ice for 5'.
  - Prepare assay mixture
  - Note: 1000-fold dilution from stock.
  - Add 20 µl of PPM solution to assay.
  - Note: 5000-fold dilution from solution.
  - Monitor ΔA_{340} over time every 10s.
  - Calculate activity as:

$$U = \frac{\frac{1}{2} * V * \Delta A340}{6220 * t * l}$$

Where, V is volume in L, t is time consistent with ΔA_{340}, and l is path length in cm.

Note: If using the NanoDrop, the rate given is equal to ΔA340/t.

Coupling Scheme:

R1P (PPM)→ R5P (4.1.2.4)→ glyceraldehyde-3-phosphate + acetaldehyde + **2NADH** (1.1.1.1) → EtOH + glycerol-3-phosphate + **2NAD**$^+$

Enzyme mixture (1mL)	
H_2O	680µl
Tris-HCl pH 7.5	10mM (10µl of 1M)
$CoCl_2$	250µM (250µl of 1mM)
EDTA pH 7.5	50µM (50µl of 1mM)
PPM Stock	10µl

Assay mixture (1mL)	
H_2O	763.6µl
Tris-HCl pH 8.3	50mM (50µl of 1M)
R1P	1mM (86.5µl of 11.67mM)
(Ribose-1,5-bisP)	
NADH	0.2mM (50µl of 4mM)
Deoxyriboaldolase	3.2U (27µl of 120U/ml)
Alcohol dehydrogenase	6U (2.9µl of 2099U/ml)
PPM mixture	20µl

Ribonucleoside Hydrolase (E.C. 3.2.2.8)

- Reaction mixture: 1mL
- Incubate mixture for 2'.
- Mix 10µl RihA + 90µl of 55.6mM HEPES pH 7.4.
- Note: 100-fold dilution from stock.
- Add 40 µl of RihA solution to assay.
- Note: 250-fold dilution from solution.
- Monitor ΔA_{262} over time every @ 37°C for 12-15min (Nanodrop 2000c Kinetics Module).
- Calculate activity as:

$$U = \frac{V * \Delta A262}{2.18 * t * l}$$

Where, V is volume in L, t is time consistent with ΔA_{262}, and l is path length in cm. The result will be in µmol/min.

Note: K_M = 0.06mM for uridine and 0.7mM for cytidine

H_2O	802 µl
HEPES pH 7.4	50mM (50µl of 1M)
Uridine	80µM (8µl of 10mM)
NaCl	100mM (100µl of 1M)

Protocol: Chemo-enzymatic synthesis of Uridine MonoPhosphate (UMP)

Allotted time: 2 – 3 days (depending on scale)

Day 1		
Experiment Type	Purpose	Allotted time (hours)
Enzymatic reaction	Coupling of ribose and uracil to synthesize UMP	2
FPLC - Vydac	Verify synthesis of UMP	1
FPLC - Boronate	Purify UMP	3
Lyophilization	Extract UMP from elutions	1 overnight per 50mL of eluent
Day 2		
Waiting		
Day 3		
UV	Check concentration of product	0.5

Materials needed: (no specific amounts given it depends on the scale of synthesis)

- Deionized/autoclaved water
- 1M Sodium phosphate monobasic
- 500mM Sodium phosphate dibasic
- 1M MgCl2
- 100mg/mL ampicillin (Store at -20C)
- 1M DTT (Store at -20C)
- 100mM dATP (Store at -20C)
- 500mM Creatine phosphate (Store at 4C)
- 1M ribose (Store at -20C)
- 50mM uracil (Store at -20C)
- 1mg/mL creatine kinase (Store at -20C)
- Myokinase (from bottle) (Store at 4C)
- 2U/µL thermostable pyrophosphatase (from vial) (Store at -20C)
- 10 mg/mL Bovine Serum Albumin (from vial)(Store at -20C)

- Ribokinase (Store at -20C)
- Phosphoribosylpyrophosphate synthetase (Store at -20C)
- Uridine phosphoribosyl transferase (Store at -20C)
- Vydac column, buffer A: 25mM Na_3PO_4 pH 2.8, 0.22µm filtered.
- Vydac column, buffer B: 125mM Na_3PO_4 pH 2.8, 0.22µm filtered.
- 50% methanol, 0.22µm filtered.
- 1M Triethylamine bicarbonate (TEABC), pH 9.4, 0.22µm filtered.
- Acidified water, pH 4.6, 0.22µm filtered.

Notes about reagents:

- dATP: Make a fresh stock every time if possible, since it dephosphorylates on every freeze-thaw cycle.
- Uracil: Its solubility is very poor, so a 50mM solution is quite cloudy. You could work with a lower concentration. However, making sure you mix the solution before use solves the problem.
- Creatine kinase: Make the 1 mg/mL stock solution in a 50mM Tris-HCl pH 7.5, 50% glycerol solution
- Myokinase: The commercial enzyme is an ammonium sulfate precipitate. It can be used directly without centrifuging it and using the pellet.
- RK, PRPPS and UPRT: These enzymes are isolated in house and stored as 50% glycerol stocks.
- Vydac column, Buffers A and B: Preparation is key. Use equimolar amounts of sodium phosphate mono- and di-basic to reach 25mM or 125mM total concentration, leaving plenty of space for pH adjustment. Then, adjust the pH with glacial acetic acid to 2.8. Fill up to volume with water. Then, filter through a 0.22µm filter.
- 1M TEABC: For every liter, mix 121mL of pure Triethylamine in the hood and fill up to a liter with water. The solution will have a yellow-ish layer at the top, this is normal. Attach a pH probe to the solution. Then, bubble CO2 (dry ice) until pH reaches 9.4. If bubbling is too slow you can heat up the container with dry ice to speed up the bubbling. If the solution has debris in it, gravity filter it. This cannot be vacuum filtered because the CO2 will be taken out of solution.
- Acidified water: To a liter of pure water, bubble CO2 (dry ice) until pH reached 4.4-4.6. This will take some time, so be patient. If the solution has debris in it, gravity filter it. This cannot be vacuum filtered because the CO2 will be taken out of solution.

Procedure:

Preparatory work:

- Prepare all of the reagents needed for the reaction, given the scale that you wish to utilize.
- Below (reaction section), you will find a modifiable spreadsheet which can be used to both determine the reaction components and the amount of reagents needed.

Reaction:

- In a conical tube (or appropriate container), put together the reaction mixture in the order stated, up to UPRT; following the spreadsheet below.

Component	[Stock]	[Desired]	Volume Needed /uL
H2O			1167
Sodium Phosphate Monobasic (mM)	1000	9.4	94
Sodium Phosphate Dibasic (mM)	500	40.6	812
MgCl2 (mM)	1000	10	100
Ampicillin (mg/mL)	100	2	200
DTT (mM)	1000	10	100
dATP (mM)	100	0.5	50
Creatine Phosphate (mM)	500	100	2000
Uracil (mM)	18.8	8.0	4267
BSA (mg/mL)	100	0.1	10
Creatine Kinase (mg/mL)	1	0.0050	50
Myokinase (U/uL)	5	0.0100	20
Pyrophosphatase (U/uL)	2	0.0020	10
RK (U/uL)	0.500	0.0050	100
PRPPS (U/uL)	0.015	0.0003	200
UPRT (U/uL)	0.200	0.0050	250
Ribose (mM)	1000	10	100
KCl (mM)	1000.000	20.0000	200
NMPK (mg/mL)	10	0.05	50
dATP (mM)	100.000	0.2	20
Creatine Phosphate (mM)	500	10	200
	Reaction Volume /mL		10

- Incubate the reaction at 37C for 5-10 minutes, or until the temperature of the mixture has reached 37C.
- Add ribose to start the reaction. Swirl or pipette up-and-down, do not shake or vortex.

- Incubate the reaction at 37C for 5 hours, with occasional stirring.

Quality control:

- Once the reaction is over, take a 120-µL aliquot and then transfer the rest to 4C.
- Load the aliquot onto a 3kDa molecular weight cut-off concentrator mini-column, spin at no more than 10,000 rpm for 15 minutes
- Collect the flow-through
- FPLC sub-protocol:
    - Wash the FPLC system with both buffer A and B, 30mL each at least.
    - Wash the Vydac reverse-phase analytical column (Port #4) manually with 30mL of Buffer A at 1.5mL/min, pressure should be near 15MPa. The maximum pressure of this column is 25MPa.
    - Inject 10µL of the flow-through sample onto the FPLC system.
    - Run the "Vydac Phosphorylation" method, approximate running time is 40 minutes.
    - Successfully made UMP should appear as a sharp peak near 5mL of elution, compare to uracil standards.
    - If the column will not be used for longer than a week, store in 50% methanol/water. Alternatively, 20% ethanol would suffice.

UMP Purification by boronate affinity chromatography:

- Wash the FPLC system with both acidified water and 1M TEABC, 30mL each at least.
- Wash the boronate affinity chromatography column (Port #3) manually with 140mL of 1M TEABC at 5.0mL/min, pressure should be near 1MPa. The maximum pressure of this column is 2.5MPa.
- Using a syringe of appropriate size, inject the entire sample directly into the in-house packed boronate column. Make sure you release both ends from the FPLC system to do so
- Reconnect the column to port #3. Watch for major bubbles being caught in the tubing.
- Run the "Boronate SorbTech" method, approximate running time is 1h 30min at 5.0mL/min.
- Successfully purified UTP should appear as a broad peak near 75mL after the switch to elution. Another way to monitor it is by the conductivity of the eluent, once the value starts dropping steeply, the peak is about to appear.
- Collect and pool all fractions of UMP in conical tubes.

Lyophilization of UMP elution fractions:

- Use a dry ice/acetone or dry ice/ethanol bath to freeze the fractions that are poured directly into the lyophilization flask. Warning, the temperature of this bath is near -78C.
- When freezing the solution, constantly rotate the flask so you can form a layer around the walls of the flask, thus increasing surface area for faster lyophilization.
- Connect the flask to the lyophilizer, already at temperature and vacuum (which are automatic settings).
- Let the lyophilization run until only powder is left in the tubes. Check regularly to ensure temperature and pressure are being maintained.
- Once finished, re-suspend powder in a minimum amount of water.

Final concentration check of UMP:

- Make sure the re-suspended UMP is well mixed.
- Using water as a blank first, make a 100- and 1000-fold dilution of UMP and measure its UV absorbance at 262nm. Ideally, use a wavescan setting so you can evaluate the shape of the absorption peak. Make note of the pathlength being used.
- Calculate the concentration of UMP using an extinction coefficient of 10,000 M-1cm-1.
- Calculate the yield of the reaction and purification up to this point.
- If the concentration is too low (< 50mM), concentrate the solution in the SpeedVac in its automatic setting. If too high (> 100mM), dilute with water.
- Add enough 1M Tris-HCl pH 7.5 buffer to reach a final concentration of 10mM Tris-HCl pH 7.5 without altering the volume significantly.
- Store the newly synthesized UMP at -20C until further use.

Protocol: Synthesis of Cytidine TriPhosphate (CTP) from Uridine TriPhosphate (UTP)

Allotted time: 6 – 7 days (depending on scale)

Day 1		
Experiment Type	Purpose	Allotted time (hours)
Enzymatic reaction	Amination of UTP to synthesize CTP	6

FPLC - Vydac	Verify synthesis of CTP	1
FPLC - Boronate	Purify CTP	3
Lyophilization	Extract CTP from elutions	1 overnight per 50mL of eluent
Day 2, 3, 4		
Waiting		
Day 5		
Speedvac	Wash re-suspended product	4
UV	Check concentration of product	0.5
FPLC - Vydac	Quality control of product	1
Day 6		
NMR	Quality control of product	2

Materials needed: (no specific amounts given it depends on the scale of synthesis)

- Deionized/autoclaved water
- 1M Tris-HCl, pH 8.0
- 1M MgCl2
- 100mg/mL ampicillin (Store at -20C)
- 100mM dATP (Store at -20C)
- 500mM NH_4Cl
- X mM UTP (Store at -20C)
- CTP synthetase (Store at -20C)
- Vydac column, buffer A: 25mM Na_3PO_4 pH 2.8, 0.22µm filtered.
- Vydac column, buffer B: 125mM Na_3PO_4 pH 2.8, 0.22µm filtered.
- 50% methanol, 0.22µm filtered.
- 1M Triethylamine bicarbonate (TEABC), pH 9.4, 0.22µm filtered.
- Acidified water, pH 4.6, 0.22µm filtered.

Notes about reagents:

- dATP: Make a fresh stock every time if possible, since it dephosphorylates on every freeze-thaw cycle.

- Vydac column, Buffers A and B: Preparation is key. Use equimolar amounts of sodium phosphate mono- and di-basic to reach 25mM or 125mM total concentration, leaving plenty of space for pH adjustment. Then, adjust the pH with glacial acetic acid to 2.8. Fill up to volume with water. Then, filter through a 0.22μm filter.
- 1M TEABC: For every liter, mix 121mL of pure Triethylamine in the hood and fill up to a liter with water. The solution will have a yellow-ish layer at the top, this is normal. Attach a pH probe to the solution. Then, bubble CO2 (dry ice) until pH reaches 9.4. If bubbling is too slow you can heat up the container with dry ice to speed up the bubbling. If the solution has debris in it, gravity filter it. This cannot be vacuum filtered because the CO2 will be taken out of solution.
- Acidified water: To a liter of pure water, bubble CO2 (dry ice) until pH reached 4.4-4.6. This will take some time, so be patient. If the solution has debris in it, gravity filter it. This cannot be vacuum filtered because the CO2 will be taken out of solution.

Procedure:

Preparatory work:

- Prepare all of the reagents needed for the reaction, given the scale that you wish to utilize.
- Below (reaction section), you will find a modifiable spreadsheet which can be used to both determine the reaction components and the amount of reagents needed.

Reaction:

- In a conical tube (or appropriate container), put together the reaction mixture in the order stated, up to CTPS; following the spreadsheet below. Make sure to modify the UTP stock concentration to whatever value you actually have in hand.

Component	[Stock]	[Desired]	Volume Needed /uL
H2O			7122
Tris-HCl pH 8.0 (mM)	1000	50	500.0
MgCl2 (mM)	1000	10	100.00
Ampicillin (mg/mL)	100	2.00	200
dATP (mM)	100	4.0	400
UTP (mM)	45	**2.00**	444.4
CTPS (mg/mL)	1.2	0.10	833.3
NH4Cl (mM)	500	**20.00**	400.0
	Reaction Volume /mL		10

- Incubate the reaction at 37C for 5-10 minutes, or until the temperature of the mixture has reached 37C.
- Add NH_4Cl to start the reaction. Swirl or pipette up-and-down, do not shake or vortex.
- Incubate the reaction at 37C for 6 hours, with occasional stirring.

Quality control:

- Once the reaction is over, take a 120-µL aliquot and then transfer the rest to 4C.
- Load the aliquot onto a 3kDa molecular weight cut-off concentrator mini-column, spin at no more than 10,000 rpm for 15 minutes
- Collect the flow-through
- FPLC sub-protocol:
    - Wash the FPLC system with both buffer A and B, 30mL each at least.
    - Wash the Vydac reverse-phase analytical column (Port #4) manually with 30mL of Buffer A at 1.5mL/min, pressure should be near 15MPa. The maximum pressure of this column is 25MPa.
    - Inject 10µL of the flow-through sample onto the FPLC system.
    - Run the "Vydac Phosphorylation" method, approximate running time is 40 minutes.
    - Successfully made CTP should appear as a small broad peak near 20mL of elution, compare to standards. Another means to check for reaction completion is by observing the disappearance of UTP at 37mL of elution.
    - Also note that the height of the CTP peak is not directly related to the amount made, since its extinction coefficient at 254nm (FPLC default) is quite low.

CTP Purification by boronate affinity chromatography:

- Wash the FPLC system with both acidified water and 1M TEABC, 30mL each at least.
- Wash the boronate affinity chromatography column (Port #3) manually with 140mL of 1M TEABC at 5.0mL/min, pressure should be near 1MPa. The maximum pressure of this column is 2.5MPa.
- Using a syringe of appropriate size, inject the entire sample directly into the in-house packed boronate column. Make sure you release both ends from the FPLC system to do so
- Reconnect the column to port #3. Watch for major bubbles being caught in the tubing.
- Run the "Boronate SorbTech" method, approximate running time is 1h 30min at 5.0mL/min.
- Successfully purified CTP should appear as a broad peak near 75mL after the switch to elution. Another way to monitor it is by the conductivity of the eluent, once the value starts dropping steeply, the peak is about to appear.
- Collect and pool all fractions of CTP in conical tubes.
- Note that, for the same reason explained above, the CTP peak may appear small.

Lyophilization of CTP elution fractions:

- Use a dry ice/acetone or dry ice/ethanol bath to freeze the fractions that are poured directly into the lyophilization flask. Warning, the temperature of this bath is near -78C.
- When freezing the solution, constantly rotate the flask so you can form a layer around the walls of the flask, thus increasing surface area for faster lyophilization.
- Connect the flask to the lyophilizer, already at temperature and vacuum (which are automatic settings).
- Let the lyophilization run until only powder is left in the tubes. Check regularly to ensure temperature and pressure are being maintained.
- Once finished, re-suspend powder in a minimum amount of water.

Final concentration check of CTP:

- Make sure the re-suspended CTP is well mixed.
- Using water as a blank first, make a 10- and 100-fold dilution of CTP and measure its UV absorbance at 273nm. Ideally, use a wavescan setting so you can evaluate the shape of the absorption peak. Make note of the pathlength being used.
- Calculate the concentration of UMP using an extinction coefficient of 9,000 $M^{-1}cm^{-1}$.
- Calculate the yield of the reaction and purification up to this point.

- If the concentration is too low (< 50mM), concentrate the solution in the SpeedVac in its automatic setting. If too high (>100 mM), dilute with water.
- Add enough 1M Tris-HCl pH 7.5 buffer to reach a final concentration of 10mM Tris-HCl pH 7.5 without altering the volume significantly.
- Store the newly synthesized UTP at -20C until further use.

Quality Control:

- To ensure that your final product is indeed pure CTP, with no (or little) contamination from substrates, you will collect another FPLC trace and some NMR data.
- FPLC QC:
    - Follow the same directions as above for the Vydac reverse-phase column.
    - The CTP sample may be injected directly into the system, a 2-5µL aliquot of a 100mM solution should suffice.
    - Again, the peak corresponding to CTP should appear near 20mL of elution.
- NMR QC:
    - Make note of the isotopic labels that have been included in the nucleotide, so as to run the appropriate experiments.
    - All the pulse programs used have already been optimized for nucleic acids, therefore they need little to no modification.
    - Make a 2mM CTP sample in 10% D2O, 0.25mM DSS in 250µL for a Shigemi tube.
    - Run diagnostic 1D and 2D experiments that will pin point the labeled atoms in UTP. Only ^{31}P experiments need to be run in the 800 MHz NMR.
    - Below is a table of common experiments and some important parameters:

Experiment	**Nuclei Observed**	**Region Observed**	**^{1}H Carrier /ppm**	**^{13}C/^{15}N/^{31}P Carrier /ppm**	**SW ^{1}H /ppm**	**SW ^{13}C/^{15}N /^{31}P /ppm**
Kgzgwg	^{1}H	All	4.7	117	24	-
Hsqcetgp	^{1}H/^{13}C	Ribose	4.7	80	13	50
Hsqcetgp	^{1}H/^{13}C	Base	4.7	130	13	94
Ktd_hsqcetf3gpsidec	^{1}H/^{15}N	Base	4.7	175	9	90

Ktd_hsqcetf3gpsidec_1d	$^{1}H/^{15}N$	Base	4.7	175	9	90
Zgdc30	^{13}C	All	4.7	110	-	120
zgdc	^{31}P	Phosphate	4.7	0	-	60

    - Once all experiments are done, you can return your NMR sample to your bulk sample, or just dispose of it.
- If the CTP passes QC, it is ready for use. Store at -20C until needed.

Supporting information of doxorubicin stacking into the IRE RNA:

To further support the hypothesis of doxorubicin intercalation, I identified NOE contacts between the drug and the RNA. Interestingly, in NOE spectra, doxorubicin caused no major crosspeaks of its own from H1, H2 and H3 (for numbering, see figure 5.1). However, I observed a number of crosspeaks arising from potential ^{1}H-^{1}H contacts between aromatic protons of doxorubicin and nucleobase protons of the IRE RNA (Figure A.1a). Specifically, in the aromatic-to-aromatic region, I observed two relatively strong peaks with a dose-dependent signal increase. Utilizing doxorubicin's proton assignments and canonical nucleobase proton chemical shifts as a guide, I determined the nature of these new crosspeaks. These contacts corresponded to doxorubicin's H2 to a pyrimidine H5, and from H1/H3 to a pyrimidine H5. Of note, I also observed a weak crosspeak, potentially generated by an H1/H3 to H5 contact (Figure A.1b). These results showed that doxorubicin's aromatic moiety was in close proximity to nucleobases in the IRE RNA, namely pyrimidines.

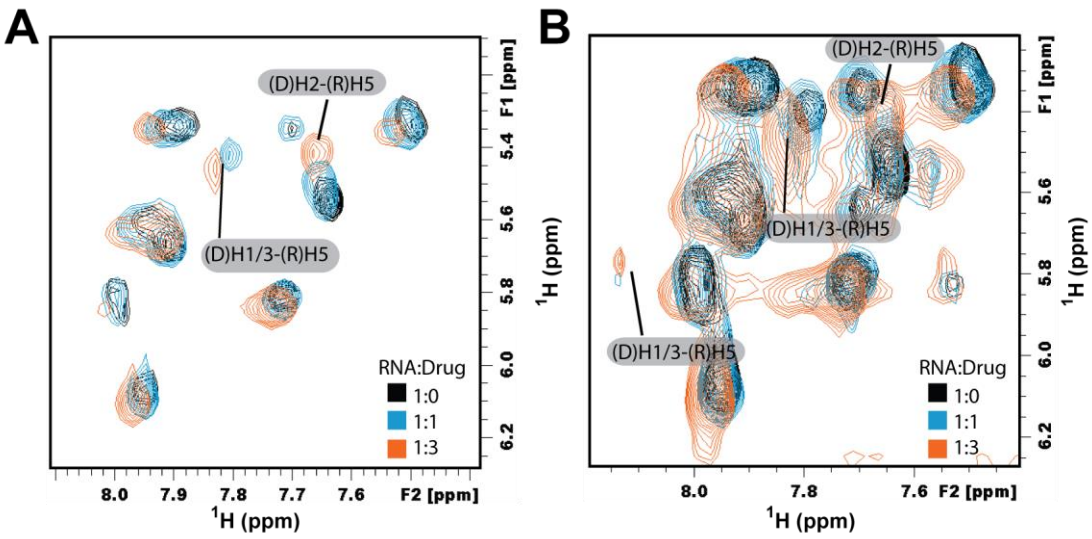

Figure A.1. Doxorubicin generates new NOE contacts with the IRE RNA. (A) Slice of a 2D NOESY experiment showing two correlation off diagonal peaks that appear upon doxorubicin titration into the IRE RNA, contacts are made from aromatic nucleobase protons ((R)H5) to aromatic doxorubicin protons ((D)H1/H2/H3). (B) Blow out of a similar slice to show one more weak correlation peak corresponding to an NOE contact of doxorubicin's H1/3 to a pyrimidine H5. (D) = doxorubicin; (R) = RNA. Ratios are shown as molar ratios.

Supporting information of the IRE RNA/IRP project:

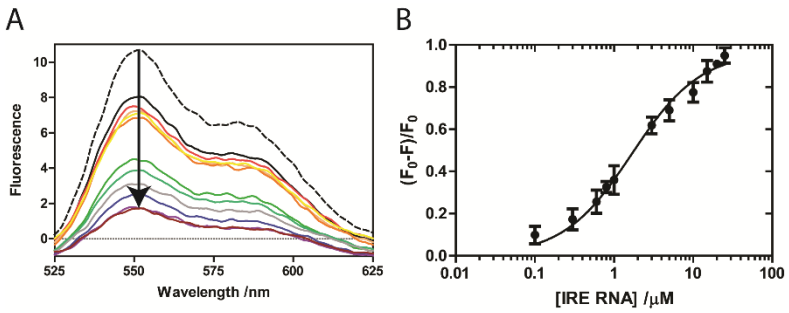

Figure A.2. Daunorubicin has micromolar-affinity interactions with the IRE RNA. (a) Representative fluorescence quenching profile of 7 μM daunorubicin's emission from 500 to 650 nm as increasing amounts of IRE RNA (0 to 25 μM) are titrated into the solution. (b) The emission intensity at 550 nm for every titration point was extracted and plotted against its corresponding IRE RNA concentration. The data were fitted to a Langmuir binding isotherm. Error bars represent standard deviation from three independent experiments.

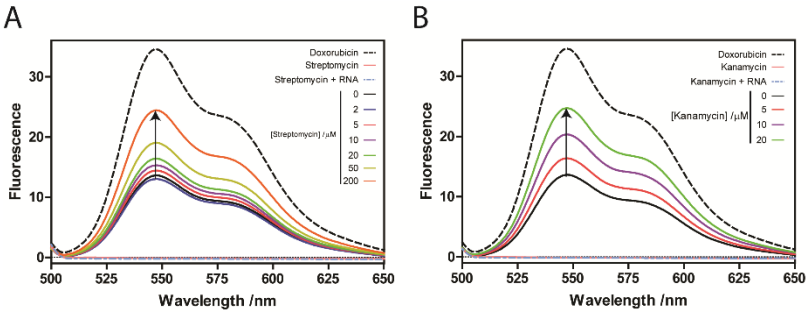

Figure A.3. Streptomycin and kanamycin have a weak competition against doxorubicin binding to the IRE RNA. These order-of-addition experiments show that increasing concentrations of both drugs recovered fluorescence only at large molar ratios of drug:RNA. (a) Streptomycin competition experiments. (b) Kanamycin competition experiments.

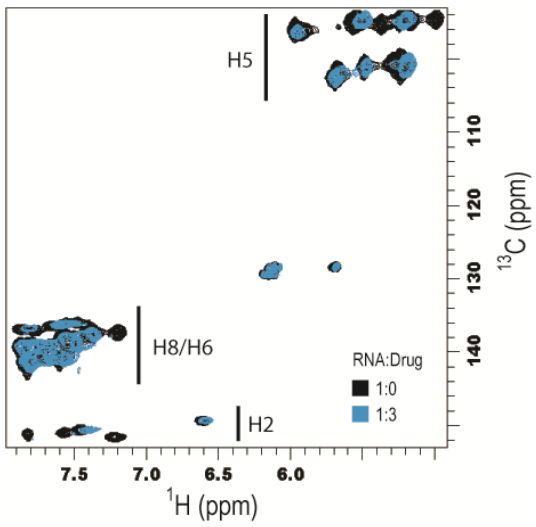

Figure A.4. Two-dimensional 13C-1H HSQC at 1:0 and 1:3 molar ratio of RNA:doxorubicin focused in the base region. No major chemical shift perturbations are observed. Line broadening is observed in the adenine H2 region only. Black: 1:0; Cyan: 1:3 RNA:drug molar ratio.

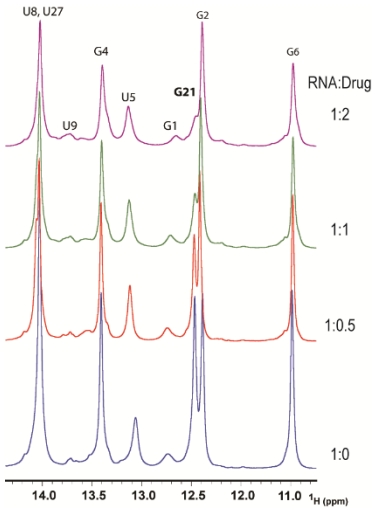

Figure A.5. 1D Daunorubicin disrupts base-pair interactions in the IRE RNA. Representative NMR titration of doxorubicin into the IRE RNA. The assigned resonances are shown. Six resonances in the imino region decrease in intensity with increasing drug concentrations. Blue: 1:0; Red: 1:0.5; Green: 1:1; Magenta: 1:2 molar ratios of RNA:daunorubicin.

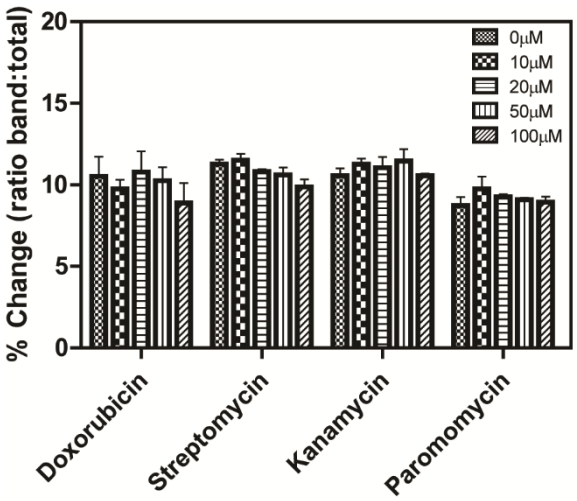

Figure A.6. The IRE RNA/IRP binding affinity at micromolar concentrations remains unaffected in the presence of streptomycin and kanamycin. (a) The RNA/protein complex was probed at increasing streptomycin and kanamycin concentrations. Quantification of the gel shift assays reveals no significant change in free or bound RNA. The y-axis is the change in band intensity as a ratio of the IRE/IRP or IRE band to the sum of both.

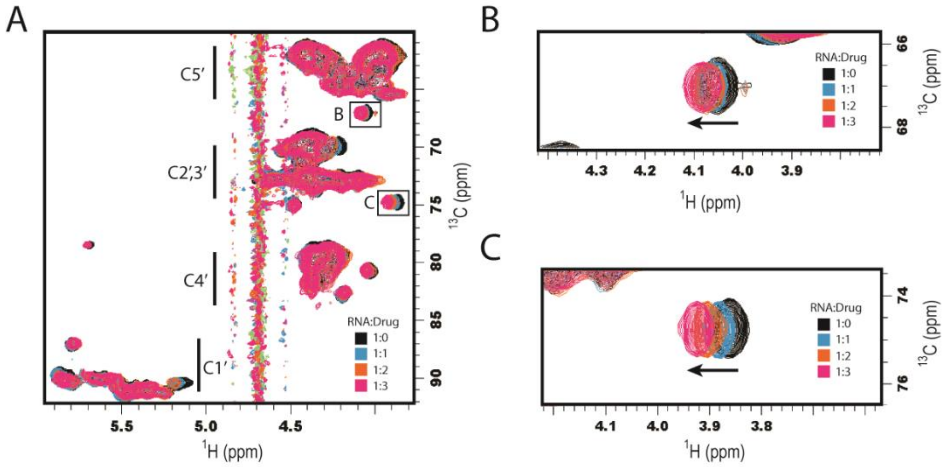

Figure A.7. Doxorubicin causes two specific chemical shift perturbations in the IRE RNA. Two-dimensional ^{13}C-^{1}H HSQC at 1:0 and 1:3 molar ratio of RNA:doxorubicin focused in the ribose region. Only two specific chemical shift perturbations are observed. Cyan: 1:0; Magenta: 1:3.

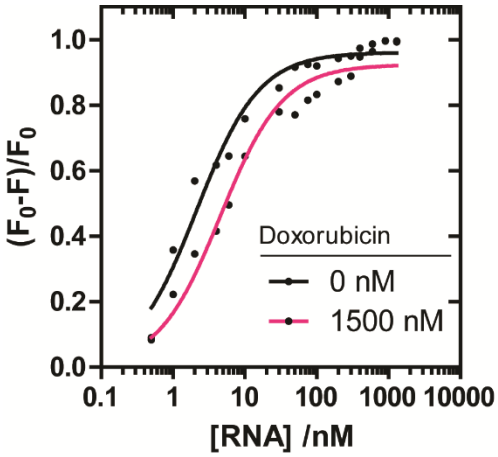

Figure A.8. The IRE RNA-IRP binding affinity at nanomolar concentrations is affected by doxorubicin at lower temperatures. (a) Upon addition of doxorubicin, the apparent binding affinity of the complex is shifted toward larger values two-fold at 12 °C. (b) The molecular stabilities (K_A) of the RNA/protein complex is affected by 45 % in the wild-type RNA, whereas the G22A-G25A mutant RNA is only affected by 29 %.

Bibliography

(1) De Benoist, B., McLean, E., Egli, I., and Cogswell, M. (2008) Worldwide prevalence of anaemia 1993 - 2005, pp 1–40.

(2) (2001) Iron Deficiency Anaemia: Assessment, Prevention, and Control. World Health Organization, pp 1 – 114.

(3) (2010) National Anemia Action Council.

(4) Guralnik, J. M., Eisenstaedt, R. S., Ferrucci, L., Klein, H. G., and Woodman, R. C. (2004) Prevalence of anemia in persons 65 years and older in the United States: evidence for a high rate of unexplained anemia. *Blood 104*, 2263–8.

(5) Brizel, D. M., Dodge, R. K., Clough, R. W., and Dewhirst, M. W. (1999) Oxygenation of head and neck cancer: changes during radiotherapy and impact on treatment outcome. *Radiother. Oncol. 53*, 113–117.

(6) Inati, A., Khoriaty, E., and Musallam, K. M. (2011) Iron in sickle-cell disease: what have I learned over the years? *Pediatr. Blood Cancer 56*, 182–90.

(7) Rees, D. C., Williams, T. N., and Gladwin, M. T. (2010) Sickle-cell disease. *Lancet 376*, 2018–2031.

(8) Harigae, H., and Furuyama, K. (2010) Hereditary sideroblastic anemia: pathophysiology and gene mutations. *Int. J. Hematol. 92*, 425–31.

(9) Hunter, G. A., and Ferreira, G. C. (2009) 5-aminolevulinate synthase: catalysis of the first step of heme biosynthesis. *Cell. Mol. Biol. (Noisy-le-grand). 55*, 102–10.

(10) Camaschella, C. (2008) Recent advances in the understanding of inherited sideroblastic anaemia. *Br. J. Haematol. 143*, 27–38.

(11) Brittenham, G. M. (2011) Iron-chelating therapy for transfusional iron overload. *N. Engl. J. Med. 364*, 146–56.

(12) Jomova, K., Vondrakova, D., Lawson, M., and Valko, M. (2010) Metals, oxidative stress and neurodegenerative disorders. *Mol. Cell. Biochem. 345*, 91–104.

(13) Salvador, G. A. Iron in neuronal function and dysfunction. *Biofactors 36*, 103–10.

(14) Weinberg, E. D. (2010) The hazards of iron loading. *Metallomics 2*, 732–40.

(15) (2010) Institute for Safe Medication Practices.

(16) (2010) Food and Drug Administration, Boxed Warning.

(17) Ceci, A., Felisi, M., De Sanctis, V., and De Mattia, D. (2003) Pharmacotherapy of iron overload in thalassaemic patients. *Expert Opin. Pharmacother. 4*, 1763–74.

(18) Brittenham, G. M., Nathan, D. G., Olivieri, N. F., Porter, J. B., Pippard, M., Vichinsky, E. P., and Weatherall, D. J. (2003) Deferiprone and hepatic fibrosis. *Blood 101*, 5089–90; author reply 5090–1.

(19) Kontoghiorghes, G. J., Spyrou, A., and Kolnagou, A. (2010) Iron chelation therapy in hereditary hemochromatosis and thalassemia intermedia: regulatory and non regulatory mechanisms of increased iron absorption. *Hemoglobin 34*, 251–64.

(20) Kontoghiorghes, G. J. (2010) Introduction of higher doses of deferasirox: better efficacy but not effective iron removal from the heart and increased risks of serious toxicities. *Expert Opin. Drug Saf. 9*, 633–41.

(21) Kontoghiorghes, G. J., Neocleous, K., and Kolnagou, A. (2003) Benefits and risks of deferiprone in iron overload in Thalassaemia and other conditions: comparison of epidemiological and therapeutic aspects with deferoxamine. *Drug Saf. 26*, 553–84.

(22) Roberts, D. J., Brunskill, S. J., Doree, C., Williams, S., Howard, J., and Hyde, C. J. (2007) Oral deferiprone for iron chelation in people with thalassaemia. *Cochrane database Syst. Rev.* CD004839.

(23) Wu, S.-F., Peng, C.-T., Wu, K.-H., and Tsai, C.-H. (2006) Liver fibrosis and iron levels during long-term deferiprone treatment of thalassemia major patients. *Hemoglobin 30*, 215–8.

(24) Anderson, G. J., Darshan, D., Wilkins, S. J., and Frazer, D. M. (2007) Regulation of systemic iron homeostasis: how the body responds to changes in iron demand. *Biometals 20*, 665–74.

(25) Hentze, M. W., Muckenthaler, M. U., and Andrews, N. C. (2004) Balancing acts: molecular control of mammalian iron metabolism. *Cell 117*, 285–97.

(26) Andrews, N. C., and Schmidt, P. J. (2007) Iron homeostasis. *Annu. Rev. Physiol. 69*, 69–85.

(27) Anderson, G. J., Frazer, D. M., and McLaren, G. D. (2009) Iron absorption and metabolism. *Curr. Opin. Gastroenterol. 25*, 129–135.

(28) Wang, J., and Pantopoulos, K. (2011) Regulation of cellular iron metabolism. *Biochem. J. 434*, 365–381.

(29) Yeh, K.-Y., Yeh, M., Mims, L., and Glass, J. (2009) Iron feeding induces ferroportin 1 and hephaestin migration and interaction in rat duodenal epithelium. *Am. J. Physiol. Gastrointest. Liver Physiol. 296*, G55–65.

(30) Ponka, P., Beaumont, C., and Richardson, D. R. (1998) Function and regulation of transferrin and ferritin. *Semin. Hematol. 35*, 35–54.

(31) Richardson, D. R., Lane, D. J. R., Becker, E. M., Huang, M. L.-H., Whitnall, M., Suryo Rahmanto, Y., Sheftel, A. D., and Ponka, P. (2010) Mitochondrial iron trafficking and the integration of iron metabolism between the mitochondrion and cytosol. *Proc. Natl. Acad. Sci. U. S. A. 107*, 10775–82.

(32) Ohgami, R. S., Campagna, D. R., Greer, E. L., Antiochos, B., McDonald, A., Chen, J., Sharp, J. J., Fujiwara, Y., Barker, J. E., and Fleming, M. D. (2005) Identification of a ferrireductase required for efficient transferrin-dependent iron uptake in erythroid cells. *Nat. Genet. 37*, 1264–9.

(33) Arosio, P., Ingrassia, R., and Cavadini, P. (2009) Ferritins: a family of molecules for iron storage, antioxidation and more. *Biochim. Biophys. Acta 1790*, 589–99.

(34) Shi, H., Bencze, K. Z., Stemmler, T. L., and Philpott, C. C. (2008) A cytosolic iron chaperone that delivers iron to ferritin. *Science 320*, 1207–10.

(35) Cherayil, B. J. (2010) Iron and immunity: immunological consequences of iron deficiency and overload. *Arch. Immunol. Ther. Exp. (Warsz). 58*, 407–15.

(36) Shull, G. E., and Theil, E. C. (1982) Translational control of ferritin synthesis by iron in embryonic reticulocytes of the bullfrog. *J. Biol. Chem. 257*, 14187–14191.

(37) Müllner, E. W., Neupert, B., and Kühn, L. C. (1989) A specific mRNA binding factor regulates the iron-dependent stability of cytoplasmic transferrin receptor mRNA. *Cell 58*, 373–82.

(38) Mikulits, W., Schranzhofer, M., Beug, H., and Müllner, E. W. (1999) Post-transcriptional control via iron-responsive elements: the impact of aberrations in hereditary disease. *Mutat. Res. 437*, 219–30.

(39) Gray, N. K., and Hentze, M. W. (1994) Iron regulatory protein prevents binding of the 43S translation pre-initiation complex to ferritin and eALAS mRNAs. *EMBO J. 13*, 3882–91.

(40) Thomson, a M., Rogers, J. T., and Leedman, P. J. (1999) Iron-regulatory proteins, iron-responsive elements and ferritin mRNA translation. *Int. J. Biochem. Cell Biol. 31*, 1139–52.

(41) Leipuviene, R., and Theil, E. C. (2007) The family of iron responsive RNA structures regulated by changes in cellular iron and oxygen. *Cell. Mol. life Sci. 64*, 2945–2955.

(42) Goforth, J. B., Anderson, S. A., Nizzi, C. P., and Eisenstein, R. S. (2010) Multiple determinants within iron-responsive elements dictate iron regulatory protein binding and regulatory hierarchy. *RNA 16*, 154–169.

(43) Binder, R., Horowitz, J. A., Basilion, J. P., Koeller, D. M., Klausner, R. D., and Harford, J. B. (1994) Evidence that the pathway of transferrin receptor mRNA degradation involves an endonucleolytic cleavage within the 3' UTR and does not involve poly(A) tail shortening. *EMBO J. 13*, 1969–80.

(44) Kühn, L. C., and Hentze, M. W. Coordination of cellular iron metabolism by post-transcriptional gene regulation. *J. Inorg. Biochem. 47*, 183–95.

(45) Theil, E. C. (2000) Targeting mRNA to Regulate Iron and Oxygen Metabolism. *Biochem. Pharmacol. 59*, 87–93.

(46) Guan, L., and Disney, M. D. (2012) Recent advances in developing small molecules targeting RNA. *ACS Chem. Biol. 7*, 73–86.

(47) Moumné, R., Catala, M., Larue, V., Micouin, L., and Tisné, C. (2012) Fragment-based design of small RNA binders: promising developments and contribution of NMR. *Biochimie 94*, 1607–1619.

(48) Ecker, D. J., and Griffey, R. H. (1999) RNA as a small-molecule drug target: doubling the value of genomics. *Drug Discov. Today 4*, 420–429.

(49) Gallego, J., and Varani, G. (2001) Targeting RNA with small-molecule drugs: therapeutic promise and chemical challenges. *Acc. Chem. Res. 34*, 836–843.

(50) Zaman, G. J. R., Michiels, P. J. A., and van Boeckel, C. A. A. (2003) Targeting RNA: new opportunities to address drugless targets. *Drug Discov. Today 8*, 297–306.

(51) Fourmy, D., Recht, M. I., Blanchard, S. C., and Puglisi, J. D. (1996) Structure of the A site of Escherichia coli 16S ribosomal RNA complexed with an aminoglycoside antibiotic. *Science (80-.). 274*, 1367–1371.

(52) Fourmy, D., Yoshizawa, S., and Puglisi, J. D. (1998) Paromomycin binding induces a local conformational change in the A-site of 16 S rRNA. *J. Mol. Biol. 277*, 333–345.

(53) Frederick, C. A., Williams, L. D., Ughetto, G., van der Marel, G. A., van Boom, J. H., Rich, A., and Wang, A. H.-J. (1990) Structural comparison of anticancer drug-DNA complexes: adriamycin and daunomycin. *Biochemistry 29*, 2538–2549.

(54) Howerton, S. B., Nagpal, A., and Williams, L. D. (2003) Surprising roles of electrostatic interactions in DNA-ligand complexes. *Biopolymers 69*, 87–99.

(55) Malina, A., Khan, S., Carlson, C. B., Svitkin, Y., Harvey, I., Sonenberg, N., Beal, P. A., and Pelletier, J. (2005) Inhibitory properties of nucleic acid-binding ligands on protein synthesis. *FEBS Lett. 579*, 79–89.

(56) Buss, J. L., Greene, B. T., Turner, J., Torti, F. M., and Torti, S. V. (2004) Iron chelators in cancer chemotherapy. *Curr. Top. Med. Chem. 4*, 1623–1635.

(57) Yang, F., Kemp, C. J., and Henikoff, S. (2013) Doxorubicin enhances nucleosome turnover around promoters. *Curr. Biol. 23*, 782–787.

(58) Bae, S. I., Zhao, R., and Snapka, R. M. (2008) PCNA damage caused by antineoplastic drugs. *Biochem. Pharmacol. 76*, 1653–1668.

(59) Kwok, J. C., and Richardson, D. R. (2003) Anthracyclines induce accumulation of iron in ferritin in myocardial and neoplastic cells: inhibition of the ferritin iron mobilization pathway. *Mol. Pharmacol. 63*, 849–861.

(60) Kwok, J. C., and Richardson, D. R. (2002) Unexpected anthracycline-mediated alterations in iron-regulatory protein-RNA-binding activity: the iron and copper complexes of anthracyclines decrease RNA-binding activity. *Mol. Pharmacol. 62*, 888–900.

(61) Canzoneri, J. C., and Oyelere, A. K. (2008) Interaction of anthracyclines with iron responsive element mRNAs. *Nucleic Acids Res. 36*, 6825–6834.

(62) Showalter, S. A., Baker, N. A., Tang, C., and Hall, K. B. (2005) Iron responsive element RNA flexibility described by NMR and isotropic reorientational eigenmode dynamics. *J. Biomol. NMR 32*, 179–193.

(63) Wang, Y. H., Sczekan, S. R., and Theil, E. C. (1990) Structure of the 5’ untranslated regulatory region of ferritin mRNA studied in solution. *Nucleic Acids Res. 18*, 4463–4468.

(64) Ma, J., Haldar, S., Khan, M. a, Sharma, S. Das, Merrick, W. C., Theil, E. C., and Goss, D. J. (2012) Fe2+ binds iron responsive element-RNA, selectively changing protein-binding affinities and regulating mRNA repression and activation. *Proc. Natl. Acad. Sci. U. S. A. 109*, 8417–22.

(65) Khan, M. A., Walden, W. E., Goss, D. J., and Theil, E. C. (2009) Direct Fe2+ sensing by iron-responsive messenger RNA:repressor complexes weakens binding. *J. Biol. Chem. 284*, 30122–30128.

(66) McCallum, S. A., and Pardi, A. (2003) Refined Solution Structure of the Iron-responsive Element RNA Using Residual Dipolar Couplings. *J. Mol. Biol. 326*, 1037–1050.

(67) Dandekar, T., Stripecke, R., Gray, N. K., Goossen, B., Constable, A., Johansson, H. E., and Hentze, M. W. (1991) Identification of a novel iron-responsive element in murine and human erythroid delta-aminolevulinic acid synthase mRNA. *EMBO J. 10*, 1903–1909.

(68) Pantopoulos, K., Porwal, S. K., Tartakoff, A., and Devireddy, L. (2012) Mechanisms of mammalian iron homeostasis. *Biochemistry 51*, 5705–5724.

(69) Gkouvatsos, K., Papanikolaou, G., and Pantopoulos, K. (2012) Regulation of iron transport and the role of transferrin. *Biochim. Biophys. Acta 1820*, 188–202.

(70) Hentze, M. W., Muckenthaler, M. U., Galy, B., and Camaschella, C. (2010) Two to tango: regulation of mammalian iron metabolism. *Cell 142*, 24–38.

(71) Gourley, B. L., Parker, S. B., Jones, B. J., Zumbrennen, K. B., and Leibold, E. A. (2003) Cytosolic aconitase and ferritin are regulated by iron in Caenorhabditis elegans. *J. Biol. Chem. 278*, 3227–3234.

(72) Kaplan, J., and Ward, D. M. (2013) The essential nature of iron usage and regulation. *Curr. Biol. 23*, R642–R646.

(73) Auffinger, P., Grover, N., and Westhof, E. (2011) Metal ion binding to RNA. *Met. Ions Life Sci. 9*, 1–35.

(74) Brown, R. S., Dewan, J. C., and Klug, A. (1985) Crystallographic and biochemical investigation of the lead(II)-catalyzed hydrolysis of yeast phenylalanine tRNA. *Biochemistry 24*, 4785–4801.

(75) Tibodeau, J. D., Fox, P. M., Ropp, P. A., Theil, E. C., and Thorp, H. H. (2006) The up-regulation of ferritin expression using a small-molecule ligand to the native mRNA. *Proc. Natl. Acad. Sci. U. S. A. 103*, 253–257.

(76) Zahringer, J., Baliga, B. S., and Munro, H. N. (1976) Subcellular distribution of total poly(A)-containing RNA and ferritin-mRNA in the cytoplasm of rat liver. *Biochem. Biophys. Res. Commun. 68*, 1088–1093.

(77) Jenkins, Z. A., Hagar, W., Bowlus, C. L., Johansson, H. E., Harmatz, P., Vichinsky, E. P., and Theil, E. C. (2007) Iron homeostasis during transfusional iron overload in beta-thalassemia and sickle cell disease: changes in iron regulatory protein, hepcidin, and ferritin expression. *Pediatr. Hematol. Oncol. 24*, 237–243.

(78) Sebastiani, G., and Pantopoulos, K. (2011) Disorders associated with systemic or local iron overload: from pathophysiology to clinical practice. *Metallomics 3*, 971–986.

(79) Brissot, P., Bardou-Jacquet, E., Jouanolle, A.-M., and Loréal, O. (2011) Iron disorders of genetic origin: a changing world. *Trends Mol. Med. 17*, 707–713.

(80) Richardson, D. R., and Ponka, P. (1997) The molecular mechanisms of the metabolism and transport of iron in normal and neoplastic cells. *Biochim. Biophys. Acta 1331*, 1–40.

(81) Fleming, R. E., and Ponka, P. (2012) Iron overload in human disease. *N. Engl. J. Med. 366*, 348–59.

(82) Brittenham, G. M., Nathan, D. G., Olivieri, N. F., Porter, J. B., Pippard, M., Vichinsky, E. P., and Weatherall, D. J. (2003) Deferiprone and hepatic fibrosis. *Blood 101*, 5089–5090.

(83) Sohn, Y.-S., Mitterstiller, A.-M., Breuer, W., Weiss, G., and Cabantchik, Z. I. (2011) Rescuing iron-overloaded macrophages by conservative relocation of the accumulated metal. *Br. J. Pharmacol. 164*, 406–418.

(84) Harvey, I., Garneau, P., and Pelletier, J. (2002) Forced engagement of a RNA/protein complex by a chemical inducer of dimerization to modulate gene expression. *Proc. Natl. Acad. Sci. U. S. A. 99*, 1882–1887.

(85) Harvey, I., Garneau, P., and Pelletier, J. (2002) Inhibition of translation by RNA-small molecule interactions. *RNA 8*, 452–463.

(86) Walden, W. E., Selezneva, A. I., Dupuy, J., Volbeda, A., Fontecilla-Camps, J. C., Theil, E., and Volz, K. (2006) Structure of Dual Function Iron Regulatory Protein 1 Complexed with Ferritin IRE-RNA. *Science (80-.). 314*, 1903–1908.

(87) Addess, K. J., Basilion, J. P., Klausner, R. D., Rouault, T. a, and Pardi, a. (1997) Structure and dynamics of the iron responsive element RNA: implications for binding of the RNA by iron regulatory binding proteins. *J. Mol. Biol. 274*, 72–83.

(88) Theil, E. C. (1998) Iron transport and storage in microorganisms, plants, and animals, in *Metal ions in biological systems* (Sigel, A., and Sigel, H., Eds.), pp 403–434. Marcel Dekker, Inc., New York.

(89) Henderson, B. R., Menotti, E., Bonnard, C., and Kuhns, L. C. (1994) Optimal Sequence and Structure of Iron-responsive Elements. *J. Biol. Chem. 269*, 17481–17489.

(90) Ke, Y., Sierzputowska-Gracz, H., Gdaniec, Z., and Theil, E. C. (2000) Internal loop/bulge and hairpin loop of the iron-responsive element of ferritin mRNA contribute

to maximal iron regulatory protein 2 binding and translational regulation in the iso-iron-responsive element/iso-iron regulatory protein family. *Biochemistry 39*, 6235–42.

(91) Ke, Y., and Theil, E. C. (2002) An mRNA loop/bulge in the ferritin iron-responsive element forms in vivo and Was detected by radical probing with Cu-1,10-phenantholine and iron regulatory protein footprinting. *J. Biol. Chem. 277*, 2373–6.

(92) Gdaniec, Z., Sierzputowska-Gracz, H., and Theil, E. (1999) Iron regulatory element and internal Loop/Bulge structure for ferritin mRNA studied by Cobalt(III) hexammine binding, molecular modeling, and NMR spectroscopy. *Biochemistry 38*, 5676.

(93) Laing, L. G., and Hall, K. B. (1996) A model of the iron responsive element RNA hairpin loop structure determined from NMR and thermodynamic data. *Biochemistry 35*, 13586–96.

(94) Artymiuk, P. J., and Green, J. (2006) The Double Life of Aconitase. *Structure 14*, 2–4.

(95) Gruer, M. J., Artymiuk, P. J., and Guest, J. R. (1997) The aconitase family: three structural variations on a common theme. *Trends Biochem. Sci.*

(96) Dupuy, J., Volbeda, A., Carpentier, P., Darnault, C., Moulis, J.-M., and Fontecilla-Camps, J. C. (2006) Crystal Structure of Human Iron Regulatory Protein 1 as Cytosolic Aconitase. *Structure 14*, 129–139.

(97) Duyne, L. I. and P. W. / W. Y. and G. van, and Volz, K. (2008) The functional duality of iron regulatory protein 1. *Curr. Opin. Struct. Biol. 18*, 106–111.

(98) Gitlin, J. D., Lill, R., Anderson, C. P., Shen, M., Eisenstein, R. S., and Leibold, E. A. (2012) Mammalian iron metabolism and its control by iron regulatory proteins. *Biochim. Biophys. Acta - Mol. Cell Res. 1823*, 1468–1483.

(99) Eisenstein, R. S. (2000) Iron regulatory proteins and the molecular control of mammalian iron metabolism. *Annu. Rev. Nutr. 20*, 627–62.

(100) Arthur, P. K., Alvarado, L. J., and Dayie, T. K. (2011) Expression, purification and analysis of the activity of enzymes from the pentose phosphate pathway. *Protein Expr. Purif. 76*, 229–37.

(101) Toor, N., Keating, K. S., and Pyle, A. M. (2009) Structural insights into RNA splicing. *Curr. Opin. Struct. Biol. 19*, 260–6.

(102) Cech, T. R. (1986) The generality of self-splicing RNA: relationship to nuclear mRNA splicing. *Cell 44*, 207–10.

(103) Dayie, K. T., and Padgett, R. A. (2008) A glimpse into the active site of a group II intron and maybe the spliceosome, too. *RNA 14*, 1697–703.

(104) Korostelev, A., Ermolenko, D. N., and Noller, H. F. (2008) Structural dynamics of the ribosome. *Curr. Opin. Chem. Biol. 12*, 674–83.

(105) Steitz, T. A. (2008) A structural understanding of the dynamic ribosome machine. *Nat. Rev. Mol. Cell Biol. 9*, 242–53.

(106) Wahl, M. C., Will, C. L., and Lührmann, R. (2009) The spliceosome: design principles of a dynamic RNP machine. *Cell 136*, 701–18.

(107) Breaker, R. R. (2009) Riboswitches: from ancient gene-control systems to modern drug targets. *Future Microbiol. 4*, 771–3.

(108) Serganov, A. Determination of riboswitch structures: light at the end of the tunnel? *RNA Biol. 7*, 98–103.

(109) Serganov, A., and Nudler, E. (2013) A decade of riboswitches. *Cell 152*, 17–24.

(110) Weigand, J. E., and Suess, B. (2009) Aptamers and riboswitches: perspectives in biotechnology. *Appl. Microbiol. Biotechnol. 85*, 229–36.

(111) Mattick, J. S. (2007) A new paradigm for developmental biology. *J. Exp. Biol. 210*, 1526–47.

(112) Ponting, C. P., Oliver, P. L., and Reik, W. (2009) Evolution and functions of long noncoding RNAs. *Cell 136*, 629–41.

(113) Rodor, J., Letelier, I., Holuigue, L., and Echeverria, M. (2010) Nucleolar RNPs: from genes to functional snoRNAs in plants. *Biochem. Soc. Trans. 38*, 672–6.

(114) Schmeing, T. M., and Ramakrishnan, V. (2009) What recent ribosome structures have revealed about the mechanism of translation. *Nature 461*, 1234–42.

(115) Newman, A. J., and Nagai, K. (2010) Structural studies of the spliceosome: blind men and an elephant. *Curr. Opin. Struct. Biol. 20*, 82–9.

(116) Tolbert, T. J., and Williamson, J. R. (1996) Preparation of Specifically Deuterated RNA for NMR Studies Using a Combination of Chemical and Enzymatic Synthesis. *J. Am. Chem. Soc. 118*, 7929–7940.

(117) Simon, E. S., Grabowski, S., and Whitesides, G. M. (1989) Preparation of phosphoenolpyruvate from D-(-)-3-phosphoglyceric acid for use in regeneration of ATP. *J. Am. Chem. Soc. 111*, 8920–8921.

(118) Rising, K. A., and Schramm, V. L. (1994) Enzymic Synthesis of NAD+ with the Specific Incorporation of Atomic Labels. *J. Am. Chem. Soc. 116*, 6531–6536.

(119) Batey, R. T., Battiste, J. L., and Williamson, J. R. (1995) Preparation of isotopically enriched RNAs for heteronuclear NMR. *Methods Enzymol. 261*, 300–322.

(120) Hall, K. B. (1995) Uses of 13C- and 15N-labeled RNA in NMR of RNA-protein complexes. *Methods Enzymol. 261*, 542–59.

(121) Pardi, A. (1995) Multidimensional heteronuclear NMR experiments for structure determination of isotopically labeled RNA. *Methods Enzymol. 261*, 350–80.

(122) Puglisi, J. D., and Wyatt, J. R. (1995) Biochemical and NMR studies of RNA conformation with an emphasis on RNA pseudoknots. *Methods Enzymol. 261*, 323–50.

(123) Davis, J. H., Tonelli, M., Scott, L. G., Jaeger, L., Williamson, J. R., and Butcher, S. E. (2005) RNA helical packing in solution: NMR structure of a 30 kDa GAAA tetraloop-receptor complex. *J. Mol. Biol. 351*, 371–82.

(124) Vallurupalli, P., Scott, L., Hennig, M., Williamson, J. R., and Kay, L. E. (2006) New RNA labeling methods offer dramatic sensitivity enhancements in 2H NMR relaxation spectra. *J. Am. Chem. Soc. 128*, 9346–7.

(125) Tolbert, T. J., and Williamson, J. R. (1997) Preparation of Specifically Deuterated and 13 C-Labeled RNA for NMR Studies Using Enzymatic Synthesis. *J. Am. Chem. Soc. 119*, 12100–12108.

(126) Dayie, K. T., Tolbert, T. J., and Williamson, J. R. (1998) 3D C(CC)H TOCSY experiment for assigning protons and carbons in uniformly 13C- and selectively 2H-labeled RNA. *J. Magn. Reson. 130*, 97–101.

(127) Scott, L. G., Tolbert, T. J., and Williamson, J. R. (2000) Preparation of specifically 2H- and 13C-labeled ribonucleotides. *Methods Enzymol. 317*, 18–38.

(128) Dayie, K. T. (2008) Key labeling technologies to tackle sizeable problems in RNA structural biology. *Int. J. Mol. Sci. 9*, 1214–40.

(129) Park, J., van Koeverden, P., Singh, B., and Gupta, R. S. (2007) Identification and characterization of human ribokinase and comparison of its properties with E. coli ribokinase and human adenosine kinase. *FEBS Lett. 581*, 3211–6.

(130) Li, S., Lu, Y., Peng, B., and Ding, J. (2007) Crystal structure of human phosphoribosylpyrophosphate synthetase 1 reveals a novel allosteric site. *Biochem. J. 401*, 39–47.

(131) Sinha, S. C., and Smith, J. L. (2001) The PRT protein family. *Curr. Opin. Struct. Biol. 11*, 733–9.

(132) Sin, I. L., and Finch, L. R. (1972) Adenine phosphoribosyltransferase in Mycoplasma mycoides and Escherichia coli. *J. Bacteriol. 112*, 439–44.

(133) Lundegaard, C., and Jensen, K. F. (1999) Kinetic mechanism of uracil phosphoribosyltransferase from Escherichia coli and catalytic importance of the conserved proline in the PRPP binding site. *Biochemistry 38*, 3327–34.

(134) Vos, S., de Jersey, J., and Martin, J. L. (1997) Crystal structure of Escherichia coli xanthine phosphoribosyltransferase. *Biochemistry 36*, 4125–34.

(135) Lunn, F. a, MacDonnell, J. E., and Bearne, S. L. (2008) Structural requirements for the activation of Escherichia coli CTP synthase by the allosteric effector GTP are stringent, but requirements for inhibition are lax. *J. Biol. Chem. 283*, 2010–20.

(136) Andersson, C. E., and Mowbray, S. L. (2002) Activation of ribokinase by monovalent cations. *J. Mol. Biol. 315*, 409–19.

(137) Gross, A., Abril, O., Lewis, J. M., Geresh, S., and Whitesides, G. M. (1983) Practical Synthesis of 5-Phospho-D-ribosyl-a-1-pyrophosphate (PRPP): Enzymatic routes from ribose 5-phosphate or ribose. *J. Am. Chem. Soc. 105*, 7428–7435.

(138) Hove-Jensen, B., and Maigaard, M. (1993) Escherichia coli rpiA gene encoding ribose phosphate isomerase A. *J. Bacteriol. 175*, 5628–35.

(139) Keough, D. T., McConachie, L. A., Gordon, R. B., de Jersey, J., and Emmerson, B. T. (1987) Human hypoxanthine-guanine phosphoribosyltransferase. Development of a spectrophotometric assay and its use in detection and characterization of mutant forms. *Clin. Chim. Acta. 163*, 301–8.

(140) Guddat, L. W., Vos, S., Martin, J. L., Keough, D. T., and De Jersey, J. (2002) Crystal structures of free , IMP- , and GMP-bound Escherichia coli hypoxanthine phosphoribosyltransferase. *Protein Sci. 11*, 1626–1638.

(141) Anderson, P. M. (1983) CTP synthetase from Escherichia coli: an improved purification procedure and characterization of hysteretic and enzyme concentration effects on kinetic properties. *Biochemistry 22*, 3285–92.

(142) Chuvikovsky, D. V, Esipov, R. S., Skoblov, Y. S., Chupova, L. a, Muravyova, T. I., Miroshnikov, A. I., Lapinjoki, S., and Mikhailopulo, I. a. (2006) Ribokinase from E. coli: expression, purification, and substrate specificity. *Bioorg. Med. Chem. 14*, 6327–32.

(143) Nosal, J. M., Switzer, R. L., and Becker, M. a. (1993) Overexpression, purification, and characterization of recombinant human 5-phosphoribosyl-1-pyrophosphate synthetase isozymes I and II. *J. Biol. Chem. 268*, 10168–75.

(144) Hochstadt, J. (1978) Adenine phosphoribosyltransferase from Escherichia coli. *Methods Enzymol. 51*, 558–67.

(145) Krenitsky, T. A., Neil, S. M., and Miller, R. L. (1970) Guanine and xanthine phosphoribosyltransfer activities of Lactobacillus casei and Escherichia coli. *J. Biol. Chem. 245*, 2605–2611.

(146) Bearne, S. L., Hekmat, O., and Donnell, J. E. M. A. C. (2001) Inhibition of Escherichia coli CTP synthase by glutamate y-semialdehyde and the role of the allosteric effector GTP in glutamine hydrolysis. *Biochem. J. 232*, 223–232.

(147) Venter, J. C., Adams, M. D., Myers, E. W., Li, P. W., Mural, R. J., Sutton, G. G., Smith, H. O., Yandell, M., Evans, C. A., Holt, R. A., Gocayne, J. D., Amanatides, P., Ballew, R. M., Huson, D. H., Wortman, J. R., Zhang, Q., Kodira, C. D., Zheng, X. H., Chen, L., Skupski, M., Subramanian, G., Thomas, P. D., Zhang, J., Gabor Miklos, G. L., Nelson, C., Broder, S., Clark, A. G., Nadeau, J., McKusick, V. A., Zinder, N., Levine, A. J., Roberts, R. J., Simon, M., Slayman, C., Hunkapiller, M., Bolanos, R., Delcher, A., Dew, I., Fasulo, D., Flanigan, M., Florea, L., Halpern, A., Hannenhalli, S., Kravitz, S., Levy, S., Mobarry, C., Reinert, K., Remington, K., Abu-Threideh, J., Beasley, E., Biddick, K., Bonazzi, V., Brandon, R., Cargill, M., Chandramouliswaran, I., Charlab, R., Chaturvedi, K., Deng, Z., Di Francesco, V., Dunn, P., Eilbeck, K., Evangelista, C., Gabrielian, A. E., Gan, W., Ge, W., Gong, F., Gu, Z., Guan, P., Heiman, T. J., Higgins, M. E., Ji, R. R., Ke, Z., Ketchum, K. A., Lai, Z., Lei, Y., Li, Z., Li, J., Liang, Y., Lin, X., Lu, F., Merkulov, G. V, Milshina, N., Moore, H. M., Naik, A. K., Narayan, V. A., Neelam, B., Nusskern, D., Rusch, D. B., Salzberg, S., Shao, W., Shue, B., Sun, J., Wang, Z., Wang, A., Wang, X., Wang, J., Wei, M., Wides, R., Xiao, C., Yan, C., Yao, A., Ye, J., Zhan, M., Zhang, W., Zhang, H., Zhao, Q., Zheng, L., Zhong, F., Zhong, W., Zhu, S., Zhao, S., Gilbert, D., Baumhueter, S., Spier, G., Carter, C., Cravchik, A., Woodage, T., Ali, F., An, H., Awe, A., Baldwin, D., Baden, H., Barnstead, M., Barrow, I., Beeson, K., Busam, D., Carver, A., Center, A., Cheng, M. L., Curry, L., Danaher, S., Davenport, L., Desilets, R., Dietz, S., Dodson, K., Doup, L., Ferriera, S., Garg, N., Gluecksmann, A., Hart, B., Haynes, J., Haynes, C., Heiner, C., Hladun, S., Hostin, D., Houck, J., Howland, T., Ibegwam, C., Johnson, J., Kalush, F., Kline, L., Koduru, S., Love, A., Mann, F., May, D., McCawley, S., McIntosh, T., McMullen, I., Moy, M., Moy, L., Murphy, B., Nelson, K., Pfannkoch, C., Pratts, E., Puri, V., Qureshi, H., Reardon, M., Rodriguez, R., Rogers, Y. H., Romblad, D., Ruhfel, B., Scott, R., Sitter, C., Smallwood, M., Stewart, E., Strong, R., Suh, E., Thomas, R., Tint, N. N., Tse, S., Vech, C., Wang, G., Wetter, J., Williams, S., Williams, M., Windsor, S., Winn-Deen, E., Wolfe, K., Zaveri, J., Zaveri, K., Abril, J. F., Guigó, R., Campbell, M. J., Sjolander, K. V, Karlak, B., Kejariwal, A., Mi, H., Lazareva, B., Hatton, T., Narechania, A., Diemer, K., Muruganujan, A., Guo, N., Sato, S., Bafna, V., Istrail, S., Lippert, R., Schwartz, R., Walenz, B., Yooseph, S., Allen, D., Basu, A., Baxendale, J., Blick, L., Caminha, M., Carnes-Stine, J., Caulk, P., Chiang, Y.

H., Coyne, M., Dahlke, C., Mays, A., Dombroski, M., Donnelly, M., Ely, D., Esparham, S., Fosler, C., Gire, H., Glanowski, S., Glasser, K., Glodek, A., Gorokhov, M., Graham, K., Gropman, B., Harris, M., Heil, J., Henderson, S., Hoover, J., Jennings, D., Jordan, C., Jordan, J., Kasha, J., Kagan, L., Kraft, C., Levitsky, A., Lewis, M., Liu, X., Lopez, J., Ma, D., Majoros, W., McDaniel, J., Murphy, S., Newman, M., Nguyen, T., Nguyen, N., Nodell, M., Pan, S., Peck, J., Peterson, M., Rowe, W., Sanders, R., Scott, J., Simpson, M., Smith, T., Sprague, A., Stockwell, T., Turner, R., Venter, E., Wang, M., Wen, M., Wu, D., Wu, M., Xia, A., Zandieh, A., and Zhu, X. (2001) The sequence of the human genome. *Science 291*, 1304–51.

(148) Blount, K. F., and Breaker, R. R. (2006) Riboswitches as antibacterial drug targets. *Nat. Biotechnol. 24*, 1558–64.

(149) (1977) The Protein Data Bank.

(150) Bernstein, F. C., Koetzle, T. F., Williams, G. J., Meyer, E. F., Brice, M. D., Rodgers, J. R., Kennard, O., Shimanouchi, T., and Tasumi, M. (1977) The Protein Data Bank: a computer-based archival file for macromolecular structures. *J. Mol. Biol. 112*, 535–42.

(151) Nikonowicz, E. P., Sirr, a, Legault, P., Jucker, F. M., Baer, L. M., and Pardi, a. (1992) Preparation of 13C and 15N labelled RNAs for heteronuclear multi-dimensional NMR studies. *Nucleic Acids Res. 20*, 4507–13.

(152) Zhou, H., Vermeulen, A., Jucker, F. M., and Pardi, A. (2001) Incorporating Residual Dipolar Couplings into the NMR Solution Structure Determination of Nucleic Acids. *Biopolymers 52*, 168–180.

(153) Hennig, M., Scott, L. G., Sperling, E., Bermel, W., and Williamson, J. R. (2007) Synthesis of 5-fluoropyrimidine nucleotides as sensitive NMR probes of RNA structure. *J. Am. Chem. Soc. 129*, 14911–21.

(154) Dayie, T. K., and Thakur, C. S. (2010) Site-specific labeling of nucleotides for making RNA for high resolution NMR studies using an E. coli strain disabled in the oxidative pentose phosphate pathway. *J. Biomol. NMR 47*, 19–31.

(155) Spano, M. N., and Walter, N. G. (2011) Solution structure of an alternate conformation of helix27 from Escherichia coli16S rRNA. *Biopolymers 95*, 653–68.

(156) Nikonowicz, E. P. (2001) Preparation and use of 2H-labeled RNA oligonucleotides in nuclear magnetic resonance studies. *Methods Enzymol. 338*, 320–41.

(157) Thakur, C. S., Sama, J. N., Jackson, M. E., Chen, B., and Dayie, T. K. (2010) Selective 13C labeling of nucleotides for large RNA NMR spectroscopy using an E. coli strain disabled in the TCA cycle. *J. Biomol. NMR 48*, 179–92.

(158) Thakur, C. S., and Dayie, T. K. (2012) Asymmetry of 13C labeled 3-pyruvate affords improved site specific labeling of RNA for NMR spectroscopy. *J. Biomol. NMR 52*, 65–77.

(159) Thakur, C. S., Luo, Y., Chen, B., Eldho, N. V, and Dayie, T. K. (2012) Biomass production of site selective 13C/15N nucleotides using wild type and a transketolase E. coli mutant for labeling RNA for high resolution NMR. *J. Biomol. NMR 52*, 103–14.

(160) Michnicka, M. J., Harper, J. W., and King, G. C. (1993) Selective isotopic enrichment of synthetic RNA: application to the HIV-1 TAR element. *Biochemistry 32*, 395–400.

(161) Hines, J. V, Landry, S. M., Varani, G., and Tinoco, I. (1994) Carbon-Proton Scalar Couplings in RNA: 3D Heteronuclear and 2D Isotope-Edited NMR of a 13C-Labeled Extra-Stable Hairpin. *J. Am. Chem. Soc. 116*, 5823–5831.

(162) Dayie, K. T., Wagner, G., September, R. V, Re, V., Recei, M., and May, V. (1997) Carbonyl Carbon Probe of Local Mobility in 13 C , 15 N-Enriched Proteins Using High-Resolution Nuclear Magnetic Resonance. *J. Am. Chem. Soc. 119*, 7797–7806.

(163) Yamazaki, T., Muhandiram, R., and Kay, L. E. (1994) NMR Experiments for the Measurement of Carbon Relaxation Properties in Highly Enriched , Uniformly l3C , I5N-Labeled Proteins : Application to 13Ca Carbons. *J. Am. Chem. Soc. 116*, 8266–8278.

(164) Hansen, A. L., and Al-Hashimi, H. M. (2007) Dynamics of large elongated RNA by NMR carbon relaxation. *J. Am. Chem. Soc. 129*, 16072–82.

(165) Wunderlich, C. H., Spitzer, R., Santner, T., Fauster, K., Tollinger, M., and Kreutz, C. (2012) Synthesis of (6-(13)C)pyrimidine nucleotides as spin-labels for RNA dynamics. *J. Am. Chem. Soc. 134*, 7558–69.

(166) Milecki, J. (2002) Specific labelling of nucleosides and nucleotides with13C and15N. *J. Label. Compd. Radiopharm. 45*, 307–337.

(167) Schultheisz, H. L., Szymczyna, B. R., Scott, L. G., and Williamson, J. R. (2011) Enzymatic de novo pyrimidine nucleotide synthesis. *J. Am. Chem. Soc. 133*, 297–304.

(168) Batey, R. T., Inada, M., Kujawinski, E., Puglisi, J. D., and Williamson, J. R. (1992) Preparation of isotopically labeled ribonucleotides for multidimensional NMR spectroscopy of RNA. *Nucleic Acids Res. 20*, 4515–23.

(169) Hoffman, D. W., and Holland, J. A. (1995) Preparation of carbon-13 labeled ribonucleotides using acetate as an isotope source. *Nucleic Acids Res. 23*, 3361–2.

(170) Lemaster, D. M., and Kushlan, D. M. (2001) Dynamical Mapping of E . coli Thioredoxin via 13 C NMR Relaxation Analysis. *J. Am. Chem. Soc. 118*, 9255–9264.

(171) Johnson, J. E., Julien, K. R., and Hoogstraten, C. G. (2006) Alternate-site isotopic labeling of ribonucleotides for NMR studies of ribose conformational dynamics in RNA. *J. Biomol. NMR 35*, 261–74.

(172) Thakur, C. S., Brown, M. E., Sama, J. N., Jackson, M. E., and Dayie, T. K. (2010) Growth of wildtype and mutant E. coli strains in minimal media for optimal production of nucleic acids for preparing labeled nucleotides. *Appl. Microbiol. Biotechnol. 88*, 771–9.

(173) SantaLucia, J., Shen, L. X., Cai, Z., Lewis, H., and Tinoco, I. (1995) Synthesis and NMR of RNA with selective isotopic enrichment in the bases. *Nucleic Acids Res. 23*, 4913–21.

(174) Endrizzi, J. a, Kim, H., Anderson, P. M., and Baldwin, E. P. (2004) Crystal structure of Escherichia coli cytidine triphosphate synthetase, a nucleotide-regulated glutamine amidotransferase/ATP-dependent amidoligase fusion protein and homologue of anticancer and antiparasitic drug targets. *Biochemistry 43*, 6447–63.

(175) MacDonnell, J. E., Lunn, F. a, and Bearne, S. L. (2004) Inhibition of E. coli CTP synthase by the "positive" allosteric effector GTP. *Biochim. Biophys. Acta 1699*, 213–20.

(176) Keun, H. C., Beckonert, O., Griffin, J. L., Richter, C., Moskau, D., Lindon, J. C., and Nicholson, J. K. (2002) Cryogenic probe 13C NMR spectroscopy of urine for metabonomic studies. *Anal. Chem. 74*, 4588–93.

(177) Griffin, J. ., Keun, H., Richter, C., Moskau, D., Rae, C., and Nicholson, J. . (2003) Compartmentation of metabolism probed by [2-13C]alanine: improved 13C NMR sensitivity using a CryoProbe detects evidence of a glial metabolon. *Neurochem. Int. 42*, 93–99.

(178) Miclet, E., Williams Jr, D. C., Clore, G. M., Bryce, D. L., Boisbouvier, J., and Bax, A. (2004) Relaxation-optimized NMR spectroscopy of methylene groups in proteins and nucleic acids. *J. Am. Chem. Soc. 126*, 10560–70.

(179) Schleucher, J., Schwendinger, M., Sattler, M., Schmidt, P., Schedletzky, O., Glaser, S. J., Sørensen, O. W., and Griesinger, C. (1994) A general enhancement scheme in heteronuclear multidimensional NMR employing pulsed field gradients. *J. Biomol. NMR 4*, 301–6.

(180) Dayie, K. T. (2005) Resolution enhanced homonuclear carbon decoupled triple resonance experiments for unambiguous RNA structural characterization. *J. Biomol. NMR 32*, 129–39.

(181) Showalter, S. a, and Hall, K. B. (2005) Isotropic reorientational eigenmode dynamics complements NMR relaxation measurements for RNA. *Methods Enzymol. 394*, 465–480.

(182) Trantírek, L., Caha, E., Kaderávek, P., and Fiala, R. (2007) NMR (13)C-relaxation study of base and sugar dynamics in GCAA RNA hairpin tetraloop. *J. Biomol. Struct. Dyn. 25*, 243–52.

(183) Nikonowicz, E. P., and Pardi, A. (1993) An efficient procedure for assignment of the proton, carbon, and nitrogen resonances in 13C/15N labeled nucleic acids. *Methods Enzymol. 232*, 1141 – 1156.

(184) Bax, A., Mehlkopf, A. ., and Smidt, J. (1979) Homonuclear broadband-decoupled absorption spectra, with linewidths which are independent of the transverse relaxation rate. *J. Magn. Reson. 35*, 167–169.

(185) Bax, A., and Freeman, R. (1981) Investigation of complex networks of spin-spin coupling by two-dimensional NMR. *J. Magn. Reson. 44*, 542–561.

(186) Grzesiek, S., and Bax, A. (1992) Improved 3D triple-resonance NMR techniques applied to a 31 kDa protein. *J. Magn. Reson. 96*, 432–440.

(187) Van de Ven, F. J. ., and Philippens, vanielle E. . (1992) Optimization of constant-time evolution in multidimensional NMR experiments. *J. Magn. Reson. 97*, 637–644.

(188) Kupce, Ē., and Wagner, G. (1996) Multisite Band-Selective Decoupling in Proteins. *J. Magn. Reson. Ser. B 110*, 309–312.

(189) Tolbert, B. S., Miyazaki, Y., Barton, S., Kinde, B., Starck, P., Singh, R., Bax, A., Case, D. A., and Summers, M. F. (2010) Major groove width variations in RNA structures determined by NMR and impact of 13C residual chemical shift anisotropy and 1H-13C residual dipolar coupling on refinement. *J. Biomol. NMR 47*, 205–19.

(190) Lane, A. N. (1995) [17] Determination of fast dynamics of nucleic acids by NMR. *Methods Enzymol. 261*, 413–435.

(191) Getz, M., Sun, X., Casiano-negroni, A., Zhang, Q., and Al-hashimi, H. M. (2007) Rna dynamics and conformational adaptation *86*, 384–402.

(192) Hall, K. B. (2008) RNA in motion. *Curr. Opin. Chem. Biol. 12*, 612–8.

(193) Guillerez, J., Lopez, P. J., Proux, F., Launay, H., and Dreyfus, M. (2005) A mutation in T7 RNA polymerase that facilitates promoter clearance. *Proc. Natl. Acad. Sci. U. S. A. 102*, 5958–5963.

(194) Milligan, J. F., Groebe, D. R., Witherell, G. W., and Uhlenbeck, O. C. (1987) Oligoribonucleotide synthesis using T7 RNA polymerase and synthetic DNA templates. *Nucleic Acids Res. 15*, 8783–98.

(195) Kao, C., Zheng, M., and Rudisser, S. (1999) A simple and efficient method to reduce nontemplated nucleotide addition at the 3 terminus of RNAs transcribed by T7 RNA polymerase. *RNA 5*, 1268–1272.

(196) Karukstis, K. K., Thompson, E. H., Whiles, J. A., and Rosenfeld, R. J. (1998) Deciphering the fluorescence signature of daunomycin and doxorubicin. *Biophys. Chem. 73*, 249–263.

(197) Changenet-Barret, P., Gustavsson, T., Markovitsi, D., Manet, I., and Monti, S. (2013) Unravelling molecular mechanisms in the fluorescence spectra of doxorubicin in aqueous solution by femtosecond fluorescence spectroscopy. *Phys. Chem. Chem. Phys. 15*, 2937–2944.

(198) Zeman, S. M., Phillips, D. R., and Crothers, D. M. (1998) Characterization of covalent adriamycin-DNA adducts. *Proc. Natl. Acad. Sci. U. S. A. 95*, 11561–11565.

(199) Cockroft, S. L., Hunter, C. A., Lawson, K. R., Perkins, J., and Urch, C. J. (2005) Electrostatic control of aromatic stacking interactions. *J. Am. Chem. Soc. 127*, 8594–8595.

(200) Seitz, O., Tewari, A. K., and Dubey, R. (2008) Emerging trends in molecular recognition: Utility of weak aromatic interactions. *Bioorg. Med. Chem. 16*, 126–143.

(201) Salonen, L. M., Ellermann, M., and Diederich, F. (2011) Aromatic rings in chemical and biological recognition: energetics and structures. *Angew. Chem. Int. Ed. Engl. 50*, 4808–42.

(202) Gooch, B. D., and Beal, P. A. (2004) Recognition of duplex RNA by helix-threading peptides. *J. Am. Chem. Soc. 126*, 10603–10610.

(203) Butt, J., Kim, H. Y., Basilion, J. P., Cohen, S., Iwai, K., Philpott, C. C., Altschul, S., Klausner, R. D., and Rouault, T. A. (1996) Differences in the RNA binding sites of iron regulatory proteins and potential target diversity. *Proc. Natl. Acad. Sci. U. S. A. 93*, 4345–4349.

(204) Kwok, J. C., and Richardson, D. R. (2002) The iron metabolism of neoplastic cells: alterations that facilitate proliferation? *Crit. Rev. Oncol. Hematol. 42*, 65–78.

(205) Chen, Y., and Varani, G. (2013) Engineering RNA-binding proteins for biology. *FEBS J. 280*, 3734–54.

(206) Teichmann, J. D. and J. P. / N. G. and S., Cléry, A., Blatter, M., and Allain, F. H.-T. (2008) RNA recognition motifs: boring? Not quite. *Curr. Opin. Struct. Biol. 18*, 290–298.

(207) Draper, D. E. (1999) Themes in RNA-protein recognition. *J. Mol. Biol. 293*, 255–270.

(208) Gegout, V., Schlegl, J., Schalger, B., Hentze, M. W., Reinbolt, J., Ehresmann, B., Ehresmann, C., and Romby, P. (1999) Ligand-induced Structural Alterations in Human Iron Regulatory Protein-1 Revealed by Protein Footprinting. *J. Biol. Chem. 274*, 15052–15058.

(209) Paraskeva, E., Gray, N. K., Schläger, B., Wehr, K., and Hentze, M. W. (1999) Ribosomal pausing and scanning arrest as mechanisms of translational regulation from cap-distal iron-responsive elements. *Mol. Cell. Biol. 19*, 807–16.

(210) Yikilmaz, E., Rouault, T. A., and Schuck, P. (2005) Self-association and ligand-induced conformational changes of iron regulatory proteins 1 and 2. *Biochemistry 44*, 8470–8478.

(211) Morris, K. F., and Johnson, C. S. (1992) Diffusion-ordered two-dimensional nuclear magnetic resonance spectroscopy. *J. Am. Chem. Soc. 114*, 3139–3141.

(212) Stejskal, E. O., and Tanner, J. E. (1965) Spin Diffusion Measurements: Spin Echoes in the Presence of a Time-Dependent Field Gradient. *J. Chem. Phys. 42*, 288.

(213) Werstuck, G. (1998) Controlling Gene Expression in Living Cells Through Small Molecule-RNA Interactions. *Science (80-.). 282*, 296–298.

(214) Minotti, G., Ronchi, R., Salvatorelli, E., Menna, P., and Cairo, G. (2001) Doxorubicin Irreversibly Inactivates Iron Regulatory Proteins 1 and 2 in Cardiomyocytes : Evidence for Distinct Metabolic Pathways and Implications for Iron-mediated Cardiotoxicity of Antitumor Therapy. *Cancer Res. 61*, 8422–8428.

(215) Hershko, C., Link, G., Konijn, A. M., and Cabantchik, Z. (2005) Objectives and Mechanism of Iron Chelation Therapy. *Ann. N. Y. Acad. Sci. 1054*, 124–135.

(216) Sun, K., and Xia, Y. (2013) New insights into sickle cell disease: a disease of hypoxia. *Curr. Opin. Hematol. 20*, 215–21.

(217) Thein, S. L. (2013) The molecular basis of β-thalassemia. *Cold Spring Harb. Perspect. Med. 3*, a011700.

(218) Goldberg, S. L. (2007) Novel treatment options for transfusional iron overload in patients with myelodysplastic syndromes. *Leuk. Res. 31 Suppl 3*, S16–22.

(219) Sheth, S., Licursi, M., and Bhatia, M. (2013) Sickle cell disease: time for a closer look at treatment options? *Br. J. Haematol. 162*, 455–64.

(220) Pietrangelo, A., Caleffi, A., and Corradini, E. (2011) Non-HFE hepatic iron overload. *Semin. Liver Dis. 31*, 302–18.

(221) Szalay, F. (2013) Hemochromatosis: one form of iron-overload diseases. *Orv. Hetil. 154*, 1156–64.

(222) Majumdar, S. (2013) The adolescent with sickle cell disease. *Adolesc. Med. State Art Rev. 24*, 295–306, xv.

(223) Vidal, F., and Rafii, A. (2013) Lymph Node Assessment in Endometrial Cancer: Towards Personalized Medicine. *Obstet. Gynecol. Int. 2013*, 892465.

(224) Kim, T.-M., Lee, S.-H., and Chung, Y.-J. (2013) Clinical applications of next-generation sequencing in colorectal cancers. *World J. Gastroenterol. 19*, 6784–6793.

(225) Venter, J. C. (2010) Multiple personal genomes await. *Nature 464*, 676–7.

(226) Wilson, R. C., and Doudna, J. A. (2013) Molecular mechanisms of RNA interference. *Annu. Rev. Biophys. 42*, 217–39.

(227) Campbell, M. A., and Wengel, J. (2011) Locked vs. unlocked nucleic acids (LNA vs. UNA): contrasting structures work towards common therapeutic goals. *Chem. Soc. Rev. 40*, 5680–9.

(228) Erlitzki, R., Long, J. C., and Theil, E. C. (2002) Multiple, conserved iron-responsive elements in the 3'-untranslated region of transferrin receptor mRNA enhance binding of iron regulatory protein 2. *J. Biol. Chem. 277*, 42579–87.